Cand. Scient. Thesis in Physical Oceanography

Single CO_2 drops in seawater

Reidun Gangstø

June 2004

Geophysical Institute
University of Bergen

The thesis is written in LaTeX2ε, reportstyle,
12 points text and double page format.
The work was completed 1st June 2004.

Abstract

To mitigate the increasing atmospheric CO_2 level and reduce the subsequent impacts, storage of CO_2 is one option that might become necessary. Ocean storage and storage of CO_2 under the sea bottom with potential leakage into the ocean both require knowledge of the behaviour of CO_2 drops in seawater.

An analysis of the dissolution and velocity of a single CO_2 drop rising from 800 m depth is made. The drop is simulated by a numerical model and theory is compared to data from an ocean experiment performed in Monterey bay, California. Single CO_2 drops were there released at 800 m and imaged under hydrate forming conditions.

The slip velocity of a hydrate-covered drop has been suggested to correspond to the drag of a spherical rigid particle. However, a clear discrepancy between this theory and the ocean observations is shown. Some possible explanations for this deviation are found. An existing parameterisation for slip velocity accounting for change of shape fits the observed drop velocity reasonably well. That deformation must be taken into account in the calculations of drop terminal velocities is confirmed by similar studies.

Hydrate is expected to reduce the mass transfer. Common theory with a reduction factor of 2 matches the observed dissolution rate. This is compatible with laboratory results.

A main reason for studying mass transfer and drop velocity is to get increased knowledge about the distribution of dissolved CO_2 in the water column. The effects of varying initial drop size, release depth and theories of dynamics and dissolution on the vertical distribution of dissolved CO_2 are studied. When deformation is not included in the calculations of drop terminal velocities, an overestimation of the vertical spread of dissolved CO_2 might be made. Releasing CO_2 near the critical depth leads to a narrower vertical range of dissolved CO_2, making release depth an important factor influencing the vertical spread in the ocean.

To study statistical probability distributions of drops, a database with information about the mass loss of numerous drops having different initial drop sizes was generated. A simple Matlab program was then developed to extract data from the database and provide different probability distributions. Normal and lognormal distributions were studied with varying standard deviations. Comparing the two showed that the distributions of dissolved CO_2 in the water column were equal when a small standard deviation was used. With a larger standard deviation the vertical spread was greater with the lognormal distribution than with the normal probability distribution. The vertical spread is especially sensitive to the presence of large drops in the drop distribution.

Acknowledgements

First of all I would like to thank my supervisors; Peter M. Haugan for introducing me to this interesting subject and Guttorm Alendal for developing the numerical model - thanks a lot to both of you for guiding me through the process in the very best way.

This thesis was partly performed at the G. C. Rieber Climate Institute, Nansen Environmental and Remote Sensing Center in Bergen. For that reason I want to thank Helge Drange at the G. C. Rieber Climate Institute for economical support and for the opportunity to get an insight into the research environment at the Nansen Center. I would also like to thank Ola M. Johannessen for useful comments to my work.

Thanks to Elin Darelius for taking time to read through my thesis and suggest improvements. And finally thanks to everybody else who has supported and helped me in different ways - not to forget the students at the Geophysical Institute for making the study time fun!

Reidun Gangstø

Contents

Chapter 1

Introduction

CO_2 is a natural component of the atmosphere-seawater system in continuous exchange between atmosphere and ocean. Due to the release of anthropogenic CO_2 to the atmosphere, the ocean is now taking up more than it gives back to the atmosphere in an attempt to regain the natural balance (IPCC 2001). Today about a third of the released CO_2 to the atmosphere is taken up in the ocean, but the entire ocean has a much higher absorbing capacity. Due to the thermocline barrier however, it takes several hundred years for the whole ocean to get into a new steady state with the atmosphere. Most of the anthropogenic CO_2 that is taken up in the ocean therefore ends up in the surface waters, giving a reduced value of pH here which might affect the marine life (Haugan & Drange 1996). To reduce this and other impacts from an increased CO_2 level in the atmosphere, CO_2 storage might be needed, in a conversion period to newer energy forms.

Marchetti (1977) was the first to suggest storage of CO_2 in the ocean, in order to delay the release to the atmosphere by several hundred years and thus reduce the expected top level of atmospheric CO_2 (Hoffert et al. 1979). Ocean storage may be done in several ways; one possible solution is to release liquid CO_2 drops at intermediate depths.

CO_2 can also be stored under the sea bottom, this has been performed for some time by Statoil at the Sleipner field (Herzog et al. 2000). A potential problem with storage under the sea bottom is leakage of CO_2 into the sea.

For CO_2 drops released into the ocean, deliberately or by a leakage, there are two main aspects to consider: environmental impacts and storage efficiency. A high concentration of dissolved CO_2 causing an ocean area with low pH might influence the marine life. A large vertical range of spreading would presumably give the least impacts on the marine biota. Storage of CO_2 is on the other hand worthless if the CO_2 reaches the surface and the atmosphere after a short time. A narrow spread of dissolved CO_2 might provide a higher density of the surrounding water and cause a sinking of the drops. This could delay the return of the CO_2 to the atmosphere (Alendal & Drange 2001).

A numerical model is here used to simulate single CO_2 drops in seawater. A main objective is to investigate the factors determining the vertical spread of dissolved CO_2. Two

components influencing this are mass transfer and terminal velocity of the drops. To be able to simulate the behaviour of single CO_2 drops and estimate the spread, an analysis of the theory used to calculate mass transfer and terminal velocity is first made based on an ocean experiment.

More background information about the climate problem and the motivation for this work can be found in chapter 2. Theory describing particle properties and behaviour in a surrounding medium is included in chapter 3. In chapter 4 the analysis of single CO_2 drop equations is found, based on literature and an ocean experiment. A study of vertical distributions of dissolved CO_2 is presented in chapter 5. The discussion in chapter 6 handles the results and summary and conclusions are given in chapter 7. A description of the numerical model used is included in Appendix A and a table of notations can be found in Appendix B.

Chapter 2

The background

2.1 CO_2 and the carbon cycle

Carbon dioxide (CO_2) takes part in a natural global circulation system involving atmosphere, ocean, geological reservoirs and land (see Figure 2.1). The ocean contains about 50 times

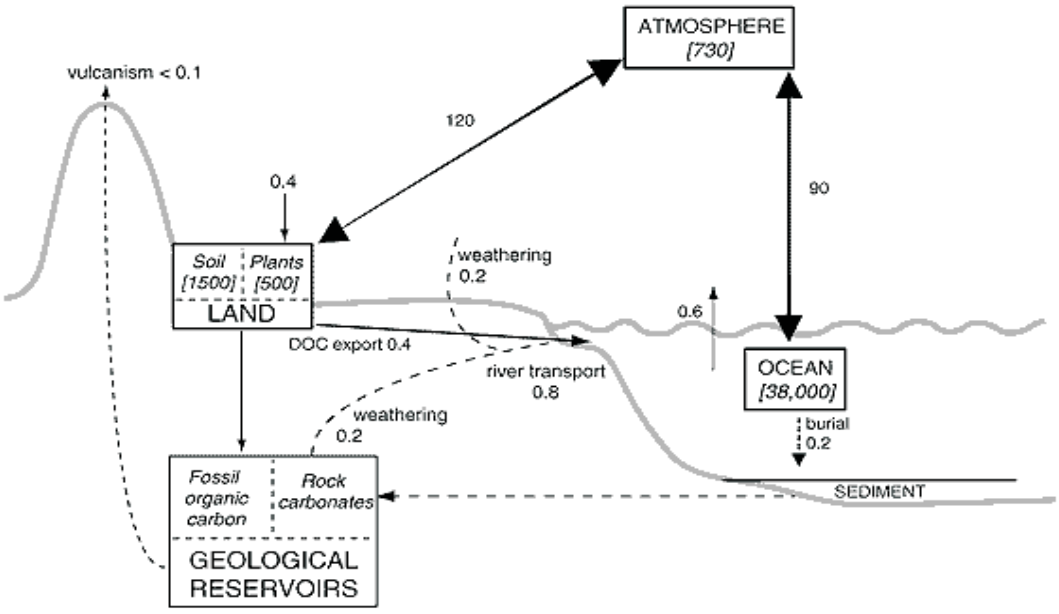

Figure 2.1: *Storages (PgC) and exchange fluxes (PgC/yr) of carbon in the natural carbon cycle (IPCC 2001).*

more carbon than the atmosphere.

By emitting anthropogenic CO_2 to the atmosphere, this natural carbon cycle has been disturbed. The carbon dioxide concentration in the atmosphere has increased by 31% since

1750 (IPCC 2001), mainly due to burning of fossil fuels. Currently the emissions are about 6 GtC/year (Sato et al. 2000) and the atmospheric partial pressure of CO_2 (pCO_2) has reached the value of 370 ppmv (parts per million by volume). This is a significant increase since before industrial times (280 ppmv). The Intergovernmental Panel on Climate Change (IPCC) has assessed a stabilization of atmospheric pCO2 at between 550 ppmv and 1000 ppmv by 2100. The atmospheric CO_2 increase is most likely a main cause of the global warming appearing the last 100 years. The IPCC predicts an average temperature increase of 1.4 - 5.8 ^oC over the next hundred years which might give catastrophic consequences for some countries in form of more droughts, floods and a rising sea level, affecting humans and the earth.

The ocean and terrestrial ecosystems together take up about half of the anthropogenic CO_2 released to the atmosphere (IPCC 2001). Net CO_2 transfer across the air-sea interface can occur whenever there is a difference in partial pressure of CO_2. Other factors that influence the transfer capacity are wind, temperature, salinity, alkalinity and pressure of surface water.

Three main forms of CO_2 in seawater can be found: dissolved CO_2 (about 1% of total), bicarbonate ion HCO_3^- (about 91%) and carbonate ion CO_3^{2-} (about 8%). The sum of these is called DIC (dissolved inorganic carbon) and this is transported in the ocean by physical processes and transformed to organic matter by biological processes. Exchange of carbon between various forms in surface water is described by the equation:

$$CO_2 + H_2O + CO_3^{2-} \rightleftharpoons 2HCO_3^- \tag{2.1}$$

Most of the CO_2 that is added to the surface waters due to an increasing atmospheric CO_2 content ends up as HCO_3^-. This results in a reduced value of pH (= -log[H+]) which may cause possible impacts to the marine biota. Typical values of pH in the ocean range from 7.7 to 8.2 (Brewer et al. 1995), with the highest values found in high latitudes in summer at the surface, the lowest at depth in old water. A reduction of 0.1 units has already occurred during the past 200 years (Haugan & Drange 1996) and continued release of fossil-fuel CO_2 into the atmosphere could result in a pH reduction of 0.7 units over the next several centuries (Caldeira & Wickett 2003). This would probably be the greatest pH change experienced in the past 300 million years (possibly except from consequences from rare, extreme events). The majority of the impacts of a lowered value of pH will occur in the upper ocean where most marine life exists and most of the biological production takes place. Even a stabilization of atmospheric CO_2 at 550 ppmv will cause severe damage to benthic life in the surface water (Thornton & Shirayama 2001).

Different feedback mechanisms take part in determining the CO_2 uptake in the ocean. As CO_2 dissolves in the surface water, less CO_3^{2-} remains to react with further CO_2. An increasing atmospheric CO_2 level with an increasing level of CO_2 in the surface waters thus correspond to a decreasing capacity of surface waters to take up anthropogenic CO_2. This effect is substantial (IPCC 2001). The temperature increase by global warming also reduces

the solubility of CO_2, as the equilibrium pCO_2 in seawater increases by about 10 to 20 ppm per ^oC temperature increase. This effect is thought to be smaller. Coupled atmosphere-ocean models (IPCC 2001) have shown that global warming provides an increase in vertical stratification, which would reduce the rate of mixing between surface and deep waters and therefore tend to reduce future ocean CO_2 uptake. Ocean calcification (precipitation of $CaCO_3$ by marine organisms) also reduces the amount of CO_3^{2-} in the surface waters. This is predicted to decrease significantly over the next 100 years and favours CO_2 uptake in the surface water (IPCC 2001).

CO_2 is taken up by the ocean much more effectively than other anthropogenic gases because of its high solubility and its chemical reactivity. In principle the ocean has a capacity to absorb 70-90% of the anthropogenic CO_2 released in the total fossil fuel era, even when emissions of up to 4500 GtC are considered (Archer et al. 1997), but this is happening through a very slow process. The surface waters use about one year to get into equilibrium with the atmosphere, but it takes several hundred years for the whole ocean to approach a new steady state in accordance with a higher atmospheric CO_2 level. This is because the thermocline makes a barrier between the surface water and the deep water so that water exchange mainly happens through the global ocean circulation.

2.2 CO_2 sequestration

IPPC also stated that the worst scenarios resulting from global warming that were made can be avoided, but many technical, economical, political, social and institutional barriers have to be climbed in order to do that. Development of renewable energy forms and efficiency technology are important parts of getting closer to a solution to the problem. Unfortunately, 85% of the energy needs in the world are covered by fossil fuels, and efficiency technology and renewable resources may not develop fast enough to limit the atmospheric CO_2 content at an acceptable level.

Removal and storage of CO_2 from power plants is one method that reduces the emissions of CO_2 to the atmosphere, and this might become necessary and important in a transition period to newer energy forms. Removed CO_2 can possibly be stored on land, in the ocean, in reservoirs and in formations under the earth or under the seabed. Thorough monitoring is then vital to investigate unwanted consequences, to calculate the efficiency of storage compared with other mitigation options and to make sure that a disposal is being executed as expected (Caldeira 2003). Two storage alternatives are further described here.

2.2.1 Geological storage

CO_2 can be stored underground in depleted oil or gas fields, unminable coal seams or in deep saline aquifers. In theory, the storage capacities in geological formations are large enough to reduce future global CO_2 emissions significantly, but there are several criteria to

take into account, some of them being geological, hydrodynamic and geothermal. About 800 sedimentary basins exists globally, but most of them are inappropriate for CO_2 sequestration (Bachu 2001). Convergent sedimentary basins should for instance be avoided due to the potential rapid escape of large amounts of CO_2 back to the atmosphere. Such an escape could cause major local environmental risks as CO_2 is heavier than air. This was tragically demonstrated in 1986 when a tremendous gas burst of CO_2 from Lake Nyos in Cameroon killed more than 1700 people and livestock up to 25 km away (Kling et al. 1994).

The physical state and properties of the injected CO_2 influence the capacity of the basin and the CO_2 behaviour. CO_2 can be stored as compressed gas, liquid or in a supercritical phase, the method suitable depends on the temperature and original pressure of the reservoir. Pressure and temperature could vary considerably within the basin and from basin to basin. Research and monitoring is therefore necessary to get a better understanding of the characteristics of the reservoirs, the physical and chemical processes and the CO_2 behaviour in combination with sequestration (Bachu 2001).

Geological storage has already been performed for a period of time. Statoil has since 1996 stored one million tons of CO_2 each year in the 250 m thick Utsira formation at the Sleipner field about 800 m under the seabed (Herzog et al. 2000). In the Alberta basin in Canada a mixture of CO_2 and H_2S is injected in deep saline aquifers and depleted hydrocarbon reservoirs (Bachu 2000).

The possibility of leakage

One potential problem associated with CO_2 injection into sedimentary basins is the leakage possibility. Leakage can occur through existing drilled wells or through the natural geological media. Some leakage is expected, the question is whether the leakage is acceptable when it comes to environmental consequences. A leakage that arises from a formation below the seabed has several uncertainties connected to it as it goes into the ocean, dissolves and might be captured there. The expected physical behavior of CO_2 that is emitted into the ocean and possible effects of this is further explained in the next section concerning ocean storage.

2.2.2 Ocean storage

Marchetti (1977) was the first to suggest injection of CO_2 into the ocean in order to reduce the atmospheric CO_2 content. He found the Strait of Gibraltar to be a suitable location as the CO_2 would follow the Mediterranean water at this site sinking down and spreading into the Atlantic. Hoffert et al. (1979) then developed their box diffusion model and studied the atmospheric response to ocean storage of CO_2. They found that the expected top level of atmospheric CO_2 would be reduced by delaying the CO_2 return to the atmosphere by several hundred years. The idea was supported by other model studies (Bacastow & Stegen 1991, Stegen et al. 1993). Many model calculations and laboratory experiments have been performed in the recent years to achieve increased knowledge of the behaviour of CO_2 in

the ocean. Only small scale experiments have been done in the actual ocean so far (Brewer et al. 1999, Brewer et al. 2002). A research experiment wishing to investigate the option of ocean storage by releasing a small plume of CO_2 in the Norwegian Sea was recently stopped due to a lacking international law. Whether such experiments should be permitted or not is still under debate in the Oslo-Paris (Ospar) convention.

Deliberately added CO_2 to the ocean could possibly give unwanted impacts. A reduced value of pH is the most instantaneous environmental effect. Marine organisms near the injection points, where a high concentration of dissolved CO_2 could exist, might be affected before dilution has occurred. The natural variability of pH in the deeper ocean is smaller than in the upper ocean, so the limits of ecosystem tolerance here is probably narrower than in the surface waters (Haugan & Drange 1996). Ocean storage would reduce the probably much larger impacts in the surface waters caused by a higher atmospheric CO_2 content. Some environmental studies have been performed, for instance the one by Caulfield et al. (1997).

Different options of ocean storage have been suggested and the most important ones are shown in Figure 2.2. In addition to temperature the behaviour of CO_2 depends largely on the

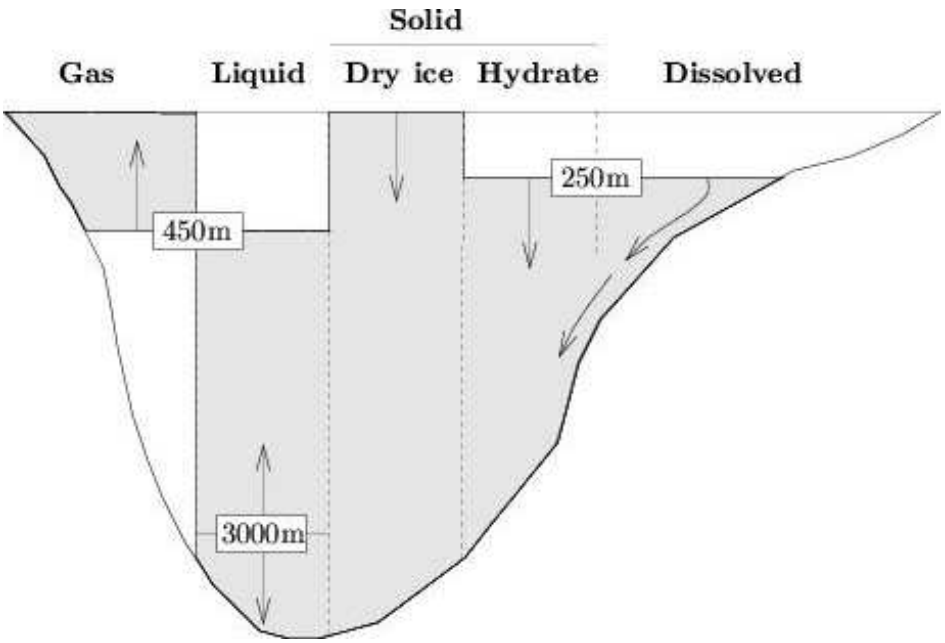

Figure 2.2: *CO_2 phases and moving directions at different depths (Alendal & Drange 2001).*

depth at which it is released. At depths shallower than about 450 m, CO_2 gas bubbles would form and quickly ascend to the surface. Between depths of about 450 and 3000 meters CO_2 will be in liquid phase and less dense than seawater. Releasing CO_2 here at intermediate depths would create a plume of rising drops, with CO_2 dissolving and spreading in the water column until the drops are small enough to follow the ocean dynamics.

Around the depth of about 3000 m the density of seawater becomes equal to the density

of CO_2, this is referred to as the critical depth. Below this depth CO_2 will be denser than seawater. This effect is due to the low compressibility of seawater and the high compressibility of liquid CO_2. Storing CO_2 as a pool on the sea floor has therefore been suggested, this would probably be kept away from the atmosphere for a very long time. Solid CO_2 is denser than seawater and releasing CO_2 as dry ice has also been suggested; this would descend to the sea floor. Nevertheless, there are practical difficulties with this option and it would be expensive. The knowledge of the ecosystems of the deep ocean interior is also still limiting, and especially the knowledge of the responses of these systems to added CO_2. In fact, the environmental effects may be significant due to the potentially large amounts of benthic life existing at the ocean bottom.

Hydrate formation is another important phenomenon to take into account. CO_2 hydrate can be created when the ocean temperature is below 10 ^oC and at depths below 200-400 m (Brewer et al. 1999). It is a crystalline clathrate compound that forms from CO_2 and water and is itself denser than seawater. If a drop of CO_2 is released under hydrate forming conditions, hydrate will form as a thin film around the drop surface affecting the character and the behaviour of the drop. There are still some uncertainties connected to hydrate formation.

As the density of the surrounding seawater increases as CO_2 dissolves in it, shallow injection of dissolved CO_2 by creating a gravity current was proposed (Haugan & Drange 1992). The initial density contrast may however not be enough to guarantee a satisfactory transfer (Alendal et al. 1994) and there may be environmental impacts at the slope (Magnesen & Wahl 1993).

Of the different ocean storage options presented, releasing CO_2 at intermediate depths seems to be the preferable option. Most of the proposed ocean disposal scenarios concern sequestration of a plume of liquid CO_2 drops at depths below the thermocline. Drange et al. (2001) found that the depth of 1000 m would be a suitable injection site, leading to an efficient and durable storing of CO_2. A great vertical range of spreading of the dissolved CO_2 would presumably give the least impacts on the marine biota. The concentration of dissolved CO_2 and the corresponding possible environmental impacts depend on several factors. Amount of released CO_2, release rate, dissolution rate and rising velocities of CO_2 drops are all essential components to consider.

Chapter 3

Theory

A fluid particle can be a drop or a bubble, depending on whether it is a mass of liquid or a mass of gas, existing in a surrounding medium. A well-defined interface separates the particle, referred to as the dispersed phase, from the external medium, termed the continuous phase. In the interaction between the dispersed and continuous phase, coupling occurs through mass, momentum and energy transfer. The concepts of mass and momentum transfer will be described in this chapter. Mass transfer takes place as an addition or removal of mass to or from the fluid particle while momentum transfer happens by the drag force or as a result of mass transfer.

3.1 Basic laws and dimensionless numbers

Two fundamental physical laws governing mass transfer and motion of particles in fluids are the principle of conservation of mass in form of the continuity equation and Newton's second law.

The continuity equation states that the rate of change of drop mass is the negative value of the mass flux through the drop surface.

Newton's second law states that the net force acting on a system is equal to the rate of change of momentum of the system. For an incompressible fluid particle, this leads to the momentum equation:

$$m_d \frac{d\mathbf{v}}{dt} = (m_c - m_d)g - F_d \tag{3.1}$$

The term on the left represents mass of the drop, m_d $[kg]$, multiplied with the acceleration, where $\mathbf{v}$ $[ms^{-1}]$ is the velocity of the drop. The terms on the right make the sum of the forces acting on the drop/bubble. The first term on the right hand side is the buoyancy force. Here m_c [kg] is the mass of the displaced surrounding medium and g $[ms^{-2}]$ is the gravitational acceleration where the positive direction is set upwards. The buoyancy force is called a body force and acts on the mass of the fluid particle. F_d is the drag force of the particle. Both the pressure field and the viscous stresses contribute to the drag force, denoted as form drag and

friction/shear drag, respectively. The drag force will be further described in section 3.3.1. Pressure and viscosity forces represent the surface forces, acting on the surface of the drop.

The surface tension, σ $[Nm^{-1}]$, tries to minimize the area of surface films. It is defined as force per unit length across any line drawn on the interface, in a direction normal to the line and tangential to the interface. It can also be interpreted as free energy per unit area of the interface (Batchelor 1967).

To identify the dominant forces in the momentum equation, dimensionless numbers are useful by expressing the ratio between two forces. If we replace the variables in the momentum equation by dimensionless parameters like the velocity scale, U, and the length scale, L, these numbers can be defined. Some of them are presented below:

The **Reynolds number** represents an important dimensionless parameter that defines the character of a flow field. It is the ratio between inertia and viscous forces:

$$Re = \rho_c L \frac{U}{\mu_c} = \frac{UL}{\nu_c}. \tag{3.2}$$

Here μ_c $[kgm^{-1}s^{-1}]$ is the molecular viscosity of the continuous phase, $\nu_c = \mu_c/\rho_c$ $[m^2s^{-1}]$ is the kinematical viscosity and ρ_c $[kgm^{-3}]$ is the density of the surrounding medium.

The **Eötvös number** is a measure of the importance of buoyancy compared to the surface tension:

$$E\ddot{o} = g\Delta\rho\frac{L^2}{\sigma}. \tag{3.3}$$

This number is further referred to as the Eotvos number, Eo.

The **Weber number** is the ratio of inertia forces to surface tension forces:

$$We = \frac{\rho_c L U^2}{\sigma}. \tag{3.4}$$

From the numbers above further numbers can be defined. An example is the **Morton number** which is a particularly useful number:

$$Mo = \frac{EoWe^2}{Re^4} = g\mu_c^4\frac{\Delta\rho}{\rho_c^2\sigma^3}. \tag{3.5}$$

$\Delta\rho$ is the density difference between the continuous phase and the drop, the density of the drop is denoted as ρ_d $[kgm^{-3}]$.

3.2 Drop shape

Fluid particles can have a range of shapes under influence of external fluid fields, and the shape affects both motion and mass transfer. In immiscible liquids, where drops and bubbles move freely only subject to gravity, three shape regimes are generally identified: The spherical, the ellipsoidal and the spherical-cap or ellipsoidal-cap regime. If surface tension

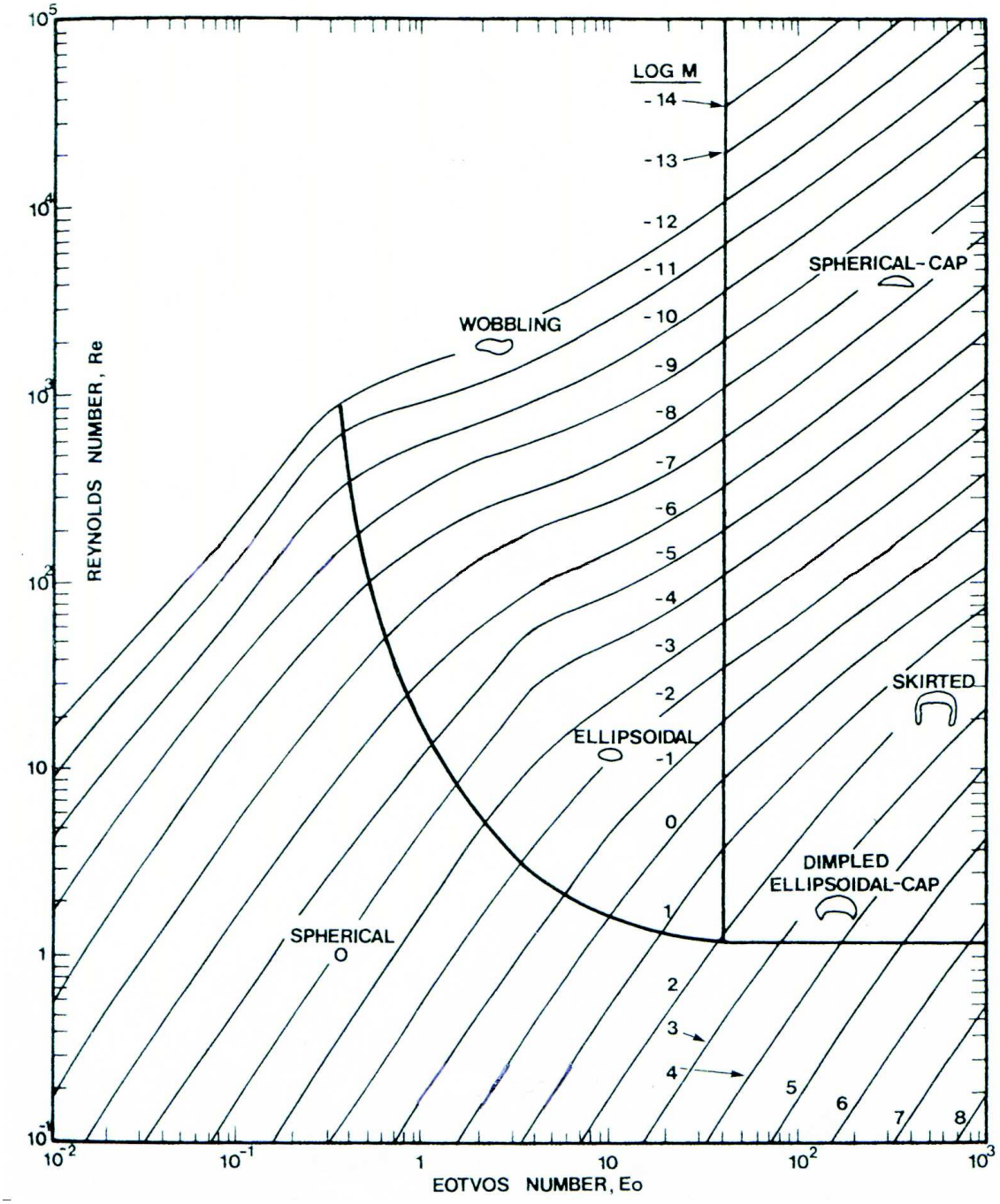

Figure 3.1: *Different shape regimes of drops and bubbles (Clift et al. 1978).*

and viscous forces dominate inertia forces, the bubbles and drops can be termed spherical. A small particle of pure fluid tends to be spherical due to the large surface to volume ratio. By definition, fluid particles are 'spherical' if the minor to major axis ratio is within 10% of unity (Clift et al. 1978).

'Ellipsoidal' bubbles and drops are oblate with a convex interface around the whole surface. The shapes may be different from true ellipsoids and there might not be any fore-and-aft symmetry, i.e. that the drop is symmetric about its minor axis. Bubbles and drops in this regime may also be subject to random wobbling motions, which makes recognizing of the shape hard. Most fluid particles of intermediate size (with a diameter of between 1 and 15 mm) are ellipsoidal.

The regime called 'spherical-cap' or 'ellipsoidal-cap' is one that large bubbles and drops often fit into. They tend to have flat bases without fore-and-aft symmetry. 'Dimpled' drops or bubbles have an indention on the back part while 'skirted' ones are often large spherical- or ellipsoidal-caps with thin envelopes of dispersed fluids.

A generalized graphical correlation can be made for fluid particles moving freely in infinite media in terms of the Eotvos, Morton and the Reynolds number. Figure 3.1 shows the resulting plot and the boundaries between the three shape regimes. The length scale L in the previous section is here defined as d_e [m], i.e. the diameter of a sphere having the equivalent volume as the fluid particle measured. Extreme values of density and viscosity ratio are not included in the figure.

We can see that for $Re < 1$ the drops and bubbles are all spherical, independent of the Eotvos number. They are ellipsoidal at intermediate to high values of *Re* and with intermediate Eo, and the particles belong to a spherical- or ellipsoidal-cap regime when Eo is large and with intermediate to large *Re*. The boundaries between the shape regimes are not well defined, but the figure is useful for showing general bubble and drop regimes (Clift et al. 1978).

3.3 Momentum transfer and motion

Momentum, defined as mass multiplied with velocity, is transferred between the dispersed and the continuous phase through mass transfer, drag and lift. The standard theory for spherical drops is first described, then an alternative theory for deformed drops and bubbles is included.

3.3.1 Spherical drops

For a sphere rising in a medium the equation of momentum (equation 3.1) becomes:

$$\frac{4}{3}\pi r^3 \rho_d \frac{d\mathbf{v}}{dt} = \frac{4}{3}\pi g r^3 (\rho_c - \rho_d) - F_d \tag{3.6}$$

The term on the left is mass times acceleration while the terms on the right define buoyancy and drag force, respectively, and r [m] is the radius of the sphere.

The drag force and the drag coefficient

The drag force represents a resistance that the particle experiences due to the presence of the continuous phase. It acts opposite to the direction of the movement of the particle. The drag force is given by the quadratic drag law:

$$F_d = C_d \frac{1}{2} \rho_c |\mathbf{u} - \mathbf{v}| (\mathbf{u} - \mathbf{v}) A \tag{3.7}$$

where $A = \pi r^2$ $[m^2]$ is the cross sectional area of the spherical fluid particle, $\mathbf{u}$ $[ms^{-1}]$ is the velocity of the continuous phase, and C_d $[1]$ is a non-dimensional proportionality factor called the drag coefficient. The drag coefficient will depend on particle shape and orientation with respect to flow as well as on the flow parameters such as Reynolds number and turbulence level. The variation of C_d for a non-rotating sphere is shown in Figure 3.2.

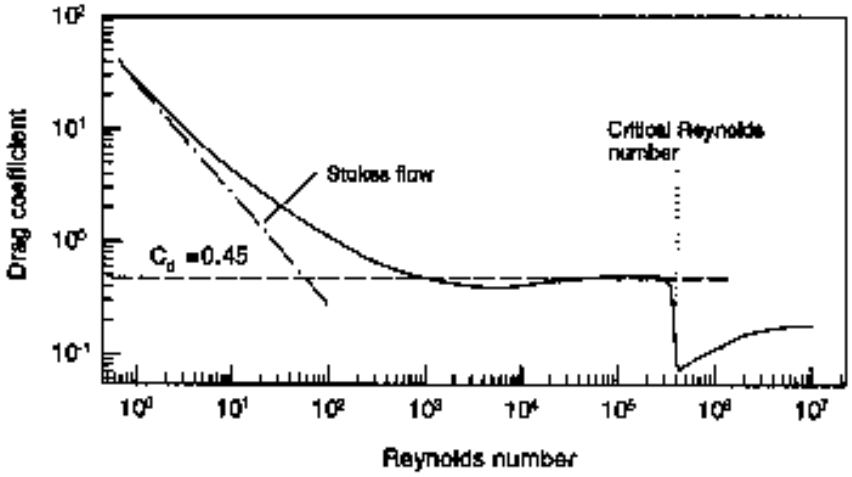

Figure 3.2: *Drag coefficient, C_d, of a sphere plotted as a function of Reynolds number (Crowe et al. 1998).*

This is the conventional correlation for the drag of a sphere, referred to as the "standard drag curve". Many equations have been suggested to approximate this curve. At low relative Reynolds numbers ($Re_r < 1$), the drag coefficient varies inversely with Reynolds number, referred to as "Stokes flow regime" with the drag coefficient given by Stokes (1851):

$$C_d = \frac{24}{Re_r}. \tag{3.8}$$

$Re_r = \rho_c d |\mathbf{u} - \mathbf{v}| \mu_c^{-1}$ is the relative Reynolds number where d $[m]$ is the diameter of the sphere and $d = 2r$.

With increasing Reynolds number the flow starts to split and vortices may form behind the drop. This leads to a decreased pressure in the wake, which increases the form drag. The

drag coefficient now approaches a nearly constant value of 0.445, called the “inertial range” or “Newton’s law range”. Here the drag is caused mainly by the form drag. For the drag coefficient in the transition region between Stokes and the inertial regime ($Re < 800$), the correlation below by Schiller & Naumann (1933) is a reasonably good approximation to the standard drag curve (within 5 %):

$$C_d = \frac{24}{Re_r}(1 + 0.15 Re_r^{0.687}). \tag{3.9}$$

With further increasing Reynolds number the drag coefficient suddenly decreases at “the critical Reynolds number” $(Re_r \sim 3 \cdot 10^5)$, where a transition to turbulence occurs, reducing the form drag and the drag coefficient.

Figure 3.3 from Crowe et al. (1998) shows spread in data that has been the outcome from different experiments with turbulence, where particle and drag coefficients have been measured. The transition to turbulence can occur at a lower Reynolds number if the particle is

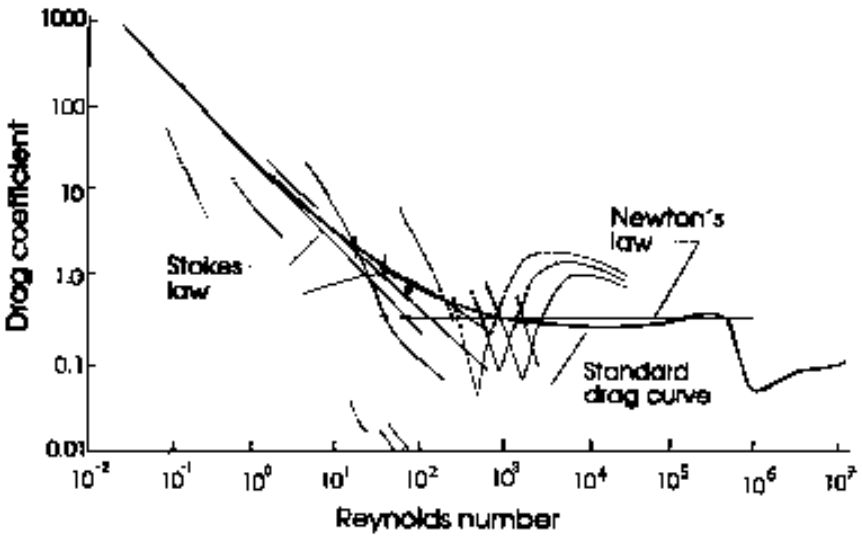

Figure 3.3: *Variation in data obtained for the drag coefficient of a sphere (Crowe et al. 1998).*

rough or if the relative turbulence intensity in the free stream is increased. The drag at higher Reynolds numbers is caused mainly by the form drag, with shear (friction) contributing little. When the boundary layer becomes turbulent, the form drag decreases and the drag therefore becomes very small. The relative turbulence intensity is defined as:

$$I_r = \frac{\sqrt{\overline{u'^2}}}{|\mathbf{u} - \mathbf{v}|} \tag{3.10}$$

where $\sqrt{\overline{u'^2}}$ is the root mean square of the carrier fluid turbulence fluctuations, $\mathbf{u}$ is the velocity of the continous phase (seawater) and $\mathbf{v}$ is the velocity of the dispersed phase (drop) (Crowe et al. 1998).

The momentum response time is the time needed for a particle to respond to a change in velocity. It is denoted as τ_V $[ms]$. Including the relative Reynolds number and dividing by mass, equation 3.6 can be written:

$$\frac{d\mathbf{v}}{dt} = \frac{\rho_c - \rho_d}{\rho_d} g - \frac{18\mu_c}{\rho_d d^2} \frac{Re_r C_d (\mathbf{u} - \mathbf{v})}{24}. \tag{3.11}$$

The response time in the Stokes flow regime, where $C_d = 24Re_r$, is defined as (Crowe et al. 1998):

$$\tau_V = \frac{\rho_d d^2}{18\mu_c}. \tag{3.12}$$

The momentum response time is most sensitive to particle size; the larger the particle is the longer will the required response time be.

Terminal velocity

When there is no acceleration of the relative velocity between the drop and the surrounding medium, the terminal velocity is achieved. Without the acceleration term in the equation of momentum (equation 3.6) a balance between the buoyancy force of the sphere and the drag force can be written:

$$\frac{4}{3}\pi g r^3 (\rho_c - \rho_d) = \frac{1}{2} C_d \rho_c \pi r^2 U_T^2. \tag{3.13}$$

U_T $[ms^{-1}]$ is then the terminal velocity of the sphere (setting the velocity of the surrounding medium equal to zero) given by:

$$U_T = \left(\frac{8gr(\rho_c - \rho_d)}{3C_d \rho_c}\right)^{0.5}. \tag{3.14}$$

3.3.2 Deformed drops

While small particles and rigid spheres follow the standard drag curve shown in Figure 3.2, intermediate and larger bubbles and drops tend to deform under influence of the surrounding medium and will have a different drag pattern. Figure 3.1 can in addition to showing shape regimes be used to estimate the terminal velocities of the different shape regimes, but to obtain accurate estimates mathematical correlations are preferred.

The theory by Grace et al. (1976)

Grace et al. (1976) suggested one way to find terminal velocities for ellipsoidal bubbles and drops. They included the effect of surface-active contaminants (surfactants) that can exist in the surrounding water. Experiments (Clift et al. 1978) have shown that in contaminated water the drag of ellipsoidal bubbles will be significantly larger than in pure water (Figure 3.4). This is because in contaminated water bubbles will be less spherical, and deformed

bubbles will have a larger drag than spherical ones. The deformation is due an absence of internal circulation, caused by the surface-active contaminants. Internal circulation increases the surface tension and helps keeping a bubble spherical. Surfactants prevent the internal circulation especially for bubbles of intermediate size, while small bubbles tend to be spherical. Small bubbles are seen to get a drag curve similar to the standard drag curve of solid, spherical particles (Figure 3.4).

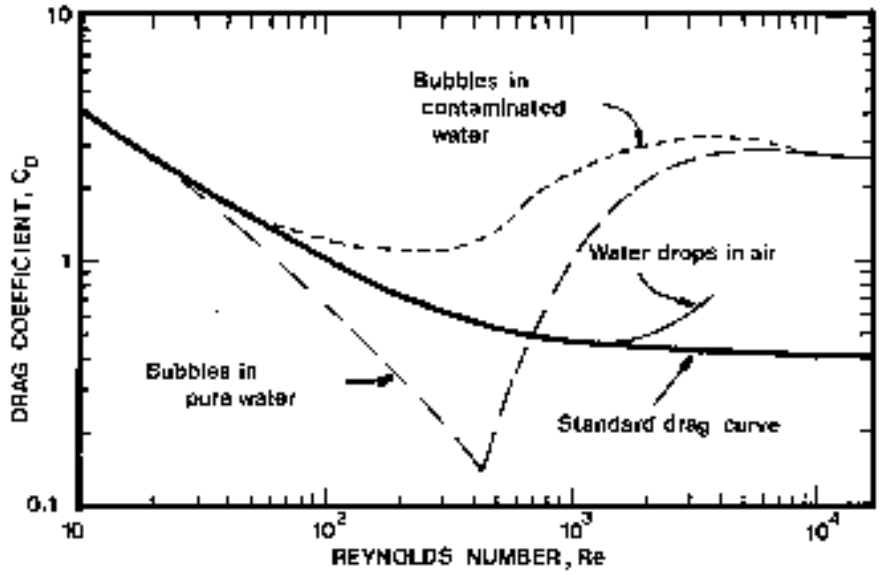

Figure 3.4: *Drag coefficient as a function of Reynolds number for bubbles in water compared with the standard drag curve for rigid spheres (Clift et al. 1978).*

A summary of terminal velocities found for carbon tetrachloride drops falling trough water measured in varying system purity are shown in Figure 3.5 (Clift et al. 1978). The lower curve, showing contaminated drops in the ellipsoidal regime, is obtained from (Grace et al. 1976):

$$U_T = \frac{\mu_c}{\rho_c d_e} Mo^{-0.149}(J - 0.857). \tag{3.15}$$

Here

$$J = \begin{cases} 0.94H^{0.757} & \text{for} \quad 2 < H <= 59.3 \\ 3.42H^{0.441} & \text{for} \quad H > 59.3 \end{cases} \tag{3.16}$$

where

$$H = \frac{4}{3} EoMo^{-0.149}(\frac{\mu_c}{\mu_w})^{-0.14} \tag{3.17}$$

and $\mu_w = 9 \cdot 10^{-4}$ $[kgm^{-1}s^{-1}]$ is the viscosity of water. Criteria that should be met here are:

$$Mo < 10^{-3}, Eo < 40, Re > 0.1. \tag{3.18}$$

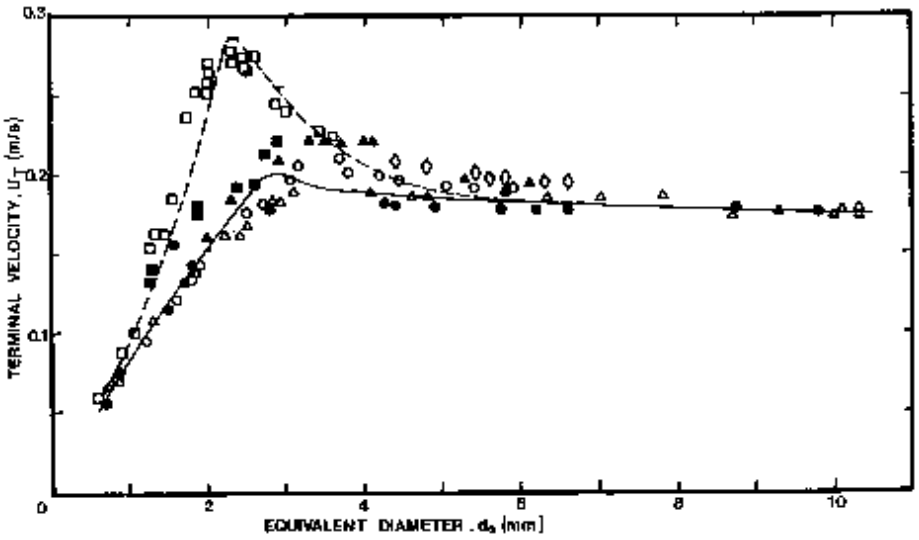

Figure 3.5: *Terminal velocity of carbon tetrachloride drops for pure systems (upper curve) and contaminated systems (lower curve) (Clift et al. 1978).*

For drops in purified water (the upper curve in Figure 3.5) a modified velocity equation was found (Grace et al. 1976):

$$U_{pure} = U[1 + \frac{\lambda}{1+\kappa}]. \tag{3.19}$$

Here λ is a correction coefficient that must be obtained experimentally and κ is the viscosity ratio μ_d/μ_c where μ_d $[kgm^{-1}s^{-1}]$ is the molecular viscosity of the drop.

The theory by Bozzano and Dente (2001)

A general way to calculate the terminal velocity of bubbles of different shapes was suggested by Bozzano & Dente (2001), based on a number of experiments. The terminal velocity is here determined by size, interfacial tension, density and viscosity of the surrounding medium. Bozzano & Dente (2001) let the drag be dependent on a generalized friction factor f, written as a function of the dimensionless numbers, the Morton, Eotvos and Reynolds numbers:

$$f = \frac{48}{Re}(\frac{1+12Mo^{1/3}}{1+36Mo^{1/3}}) + 0.9\frac{Eo^{3/2}}{1.4(1+30Mo^{1/6}) + Eo^{3/2}}. \tag{3.20}$$

Re, Eo and M are defined in equations 3.2, 3.3 and 3.5, the length scale L is now replaced with the equivalent diameter d_e. The drag is found from:

$$C_d = f(\frac{a}{r_e})^2 \tag{3.21}$$

where a $[m]$ is the major semi-axis of the drop and r_e $[m]$ is the equivalent radius, i.e. the radius of a sphere having the equivalent volume as the fluid particle measured. Bozzano &

Dente (2001) also found a correlation for $(\frac{a}{r_e})^2$:

$$(\frac{a}{r_e})^2 \cong \frac{10(1+1.3Mo^{1/6})+3.1Eo}{10(1+1.3Mo^{1/6})+Eo}. \tag{3.22}$$

The resulting drag coefficient, C_d, can then be employed in the terminal velocity equation (equivalent to equation 3.14):

$$U_T = (\frac{8gr_e(\rho_c-\rho_d)}{3C_d\rho_c})^{0.5} \tag{3.23}$$

to obtain the bubble velocity. Bozzano & Dente (2001) originally set $\Delta\rho = \rho_c$ in the Morton number and the expression for terminal velocity.

3.4 Mass transfer

The continuity equation for a drop is given in the form:

$$\frac{dm}{dt} = -\rho_s wS \tag{3.24}$$

where m [kg] is the mass of a drop or bubble, ρ_s $[kgm^{-3}]$ is the density of the fluid at the drop surface S $[m^2]$ and w $[ms^{-1}]$ is the velocity through the drop surface, taken here to be uniform and positive if mass is transferred out from the drop.

When a fluid drop dissolves in seawater, the mass that is transported from the surface of the drop, is driven by the difference in fluid mass concentration between surface and ambient fluid. The mass flux at the surface can be given by Fick's law:

$$\rho_s w = -D_v \frac{\partial \rho_d}{\partial n} \tag{3.25}$$

where n is the coordinate normal to the surface in the direction out from the drop and D_v $[m^2s^{-1}]$ is the diffusion coefficient. For scalars in water this is:

$$D_v = \frac{7.1141 \cdot 10^{-15} \cdot (273,15+T)}{\mu_c} \tag{3.26}$$

where T $[^oC]$ is the temperature of the fluid in the continuous phase. For seawater with temperature equal to 20 ^{o}C and salinity of 36 psu, $\mu_c = \mu_{sw} = 1.075 \cdot 10^{-3}$ $kgms^{-1}$.

Equation 3.25 is similar to:

$$\rho_s w = -\rho_s D_v \frac{\partial(\rho_d/\rho_s)}{\partial n} = -\rho_s D_v \frac{\partial \omega_d}{\partial n} \sim \rho_c D_v \frac{\omega_{d,s}-\omega_{d,\infty}}{d}. \tag{3.27}$$

Here ω_d [1] is the mass fraction of the dispersed phase, $\omega_{d,s}$ [1] is the mass fraction at the surface and $\omega_{d,\infty}$ in the free stream. The density ρ_c $[kgm^{-3}]$ is representative density and can be taken as the density of the continuous phase.

Given the continuity equation (3.24), the rate of change of mass of a spherical drop is proportional to:

$$\frac{dm}{dt} \sim \pi d^2 \rho_c D_v \frac{\omega_{d,\infty} - \omega_{d,s}}{d} \tag{3.28}$$

The proportionality constant to be used is called the **Sherwood number**, Sh. Applying this gives:

$$\frac{dm}{dt} = Sh\pi d\rho_c D_v(\omega_{d,\infty} - \omega_{d,s}). \tag{3.29}$$

The Sherwood number is found by a correlation which represents the effect of relative velocity between the drop and the surrounding medium. This effect is to increase the rate of mass transfer. The correlation is called the **Ranz-Marshall correlation** and is formulated as

$$Sh = 2 + 0.69 Re_r^{0.5} Sc^{0.33}. \tag{3.30}$$

Sc is the **Schmidt number**:

$$Sc = \frac{\nu_c}{D_v}. \tag{3.31}$$

From Section 3.1 we know that ν_c $[m^2 s]$ is the kinematic viscosity of the continuous phase and $\nu_c = \frac{\mu_c}{\rho_c}$. With seawater as the continuous phase and μ_c set equal to $1.075 \cdot 10^{-3}$ $kgms^{-1}$, $\nu_c = \nu_{sw} = 1.049 \cdot 10^{-6}$ $m^2 s^{-1}$, and the value of Sc would be around $5 \cdot 10^8$.

Re_r is the relative Reynolds number as defined earlier, based on the relative speed between the drop and the continuous phase. The Ranz-Marshall correlation with the factor 0.69 in equation 3.30 is valid for $30 \leq Re_r \leq 2000$. For $2 \leq Re_r \leq 200$ a factor of 0.6 should be used instead of 0.69. In cases where there is no net flow around the drop the value of the Sherwood number becomes a constant, Sh = 2.

In a simpler way, the linear rate of changing mass of a drop can be used (Brewer et al. 2002). The velocity of mass being dissolved, *w* in equation 3.24, is then equivalent to a constant dissolution rate that must be obtained experimentally. Taking the dissolution rate Γ $[molm^{-2}s^{-1}]$, we have to multiply with the specific volume V_m $[m^3 mol^{-1}]$ of the drop fluid to get the right dimensions (ms^{-1}). For a spherical drop with the surface $S = 4\pi r^2$, the equation of changing mass with time then becomes:

$$\frac{dm}{dt} = -4\pi r^2 \rho_s V_m \Gamma \tag{3.32}$$

where ρ_s is the density of the drop fluid at the surface, chosen equal to the density of the drop, ρ_d. Equally, as $m = 4\pi r^3 \rho_d / 3$ for a spherical drop, equation 3.32 can be written:

$$\frac{dr}{dt} = -V_m \Gamma. \tag{3.33}$$

3.5 Size distribution

To describe the variation of drop sizes, statistical parameters are practical to use. The spread of the size distribution can in the most general way be defined by the terms monodisperse or polydisperse. Particles or drops near one specific size belong to a monodispersed distribution, while the distribution of particles of several different sizes together is polydispersed.

3.5.1 Discrete distribution

Drop or particle size distribution can be described by number or mass. When the number of drops in a chosen size interval is counted, registered and the distribution is normalized, we call the representation a discrete number frequency distribution. The number frequency, $f_n(D_i)$, corresponds to each size interval ΔD. A measure of size to be used is the diameter (for a spherical particle) or equivalent diameter (for nonspherical particles). The distribution is normalized when

$$\sum_{i=1}^{N} f_n(D_i) = 1 \tag{3.34}$$

where N is the total number of intervals. The number-average distribution size can be found from:

$$\overline{D}_n = \sum_{i=1}^{N} D_i f_n(D_i) \tag{3.35}$$

while the number variance

$$\sigma_n^2 = \sum_{i=1}^{N} (D_i - \overline{D}_n)^2 f_n(D_i) = \sum_{i=1}^{N} {D_i}^2 f_n(D_i) - \overline{D}_n^2 \tag{3.36}$$

represents the spread of the distribution. The number standard deviation is then

$$\sigma_n = \sqrt{\sigma_n^2}. \tag{3.37}$$

Correspondingly, when using mass as the dependent variable we achieve the discrete mass frequency distribution, $f_m(D_i)$. Here we get similar equations to the number representation, only n is replaced by m.

3.5.2 Continuous distribution

The continuous frequency can be achieved by letting the size interval ΔD approach zero.

$$f_{n/m}(D) = \lim_{\Delta D \to 0} \frac{f_{n/m}(D)}{\Delta D}. \tag{3.38}$$

The differential quantity $f_{n/m}(D)dD$ gives the number/mass fraction of particles with diameter between D and $D+dD$. Now the variation of the frequency distribution with size can be shown as a continuous function

$$\int_0^{D_{max}} f(D)dD = 1 \tag{3.39}$$

if the distribution has been normalized. D_{max} is the maximum drop size.

Size data are usually discrete values. A general practice is to treat the values as if they were continuous and estimate useful statistical parameters.

The mode is the point where the frequency function has its maximum. A bimodal distribution has two maxima. The mean is estimated from the frequency distribution by

$$\mu = \int_0^{D_{max}} Df(D)dD. \tag{3.40}$$

The variance can be found from the integral

$$\sigma^2 = \int_0^{D_{max}} (D-\mu)^2 f(D)dD = \int_0^{D_{max}} D^2 f(D)dD - \mu^2. \tag{3.41}$$

The standard deviation is again the positive square root of the variance. We have a monodispersed distribution if

$$\frac{\sigma}{\mu} < 0.1. \tag{3.42}$$

Most drops are located within 2 or 3 standard deviations.

3.5.3 Probability distributions

There are several different distribution functions to use, two continuous distributions are presented below.

Normal distribution

One common distribution function is the normal (Gaussian) distribution, which is defined as

$$f(x) = \frac{1}{\sqrt{2\pi}\sigma} e^{-\frac{1}{2}(\frac{x-\mu}{\sigma})^2}, \tag{3.43}$$

where σ is the standard deviation and μ the mean. The distribution is symmetric about the mean and bell-shaped (see Figure 3.6 a)), and has been normalized so that

$$\int_0^{\infty} f(x)dx = 1. \tag{3.44}$$

In a normal distribution 68 % of the data is located between $\mu\pm\sigma$ and 95 % between $\mu\pm2\sigma$. A **standard normal distribution** has mean zero and standard deviation 1.

The curve of a continuous probability distribution is constructed so that the area under the curve, with the boundaries $x = x_1$ and $x = x_2$, is equal to the probability that a random variable X has a value between $x = x_1$ and $x = x_2$. This probability can be found by calculating the integral of equation 3.43 between $x = x_1$ and $x = x_2$. To make it easier to find such probabilities, statistical tables were made for distributions with mean zero and standard deviation 1. Every observations of any normal random variable X can be transformed into a new set of observations of a normal variable Z with mean zero and standard deviation 1 by:

$$Z = \frac{X - \mu}{\sigma}. \tag{3.45}$$

The statistical table gives the area under the standard normal curve that correspond to the probability that Z has a value less than z for different values of z (Walpole et al. 1998).

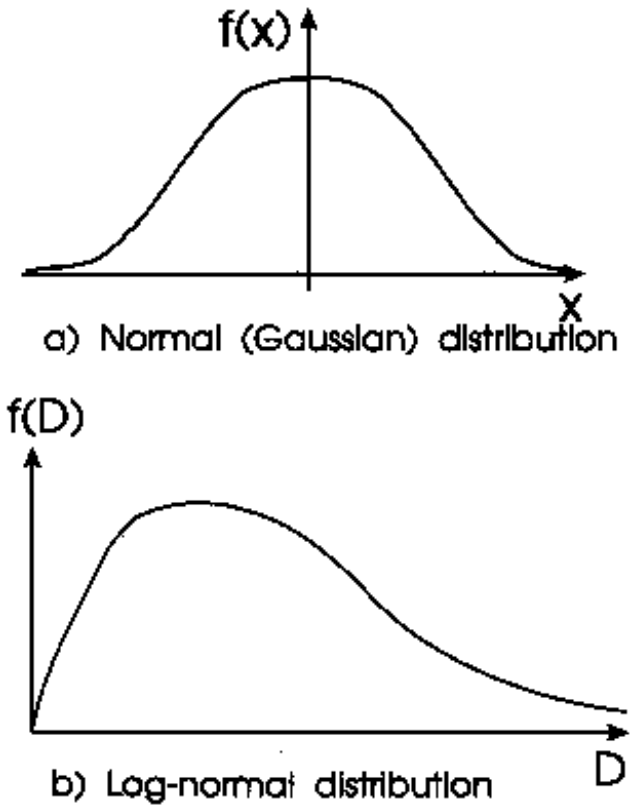

Figure 3.6: *a) Normal and b) lognormal distributions (Crowe et al. 1998).*

Lognormal distribution

Another distribution function is the lognormal distribution:

$$f(x) = \begin{cases} \frac{1}{\sqrt{2\pi}\sigma x} e^{-[ln(x)-\mu]^2/(2\sigma^2)} & \text{for} \quad x \geq 0 \\ 0 & \text{for} \quad x < 0 \end{cases} \tag{3.46}$$

The mean and variance of the lognormal distribution are:

$$E(x) = e^{\mu+\sigma^2/2} \tag{3.47}$$

$$Var(x) = e^{2\mu+\sigma^2} \cdot (e^{\sigma^2} - 1) \tag{3.48}$$

A lognormal distribution is presented in Figure 3.6 b).

Chapter 4

An analysis of single drop equations

Theory describing terminal velocity and mass transfer of a single drop is here studied and the theoretical results are compared with an ocean experiment. Factors that may influence the drag are especially discussed.

A numerical model (described in Appendix A) is used to simulate a single drop of CO_2 released and rising in the ocean. In the model the set of equations used to calculate drop velocity and mass loss must be chosen at first, and initial values of drop diameter, release depth and drag coefficient must be given. The numerical model then provides data of time, depth, diameter, mass, seawater density and temperature, CO_2 density and drop velocity. The model run is stopped when the CO_2 drop has got a minimum diameter, here chosen as 10^{-3} m. The time step determining how often the data is written out is set to 1 s.

The initial drop and seawater characteristics included in this analysis are based on the experiment by Brewer et al. (2002) introduced next.

4.1 Observations by Brewer et al. (2002)

Peter G. Brewer et al. released CO_2 drops in the ocean at 800 meters depth in Monterey Bay, California (Brewer et al. 2002). In order to follow and measure precisely the rising drops, an imaging box with a transparent face was used, fixed to a remotely operated vehicle (ROV) shown in Figure 4.1. The box had a meter scale fastened to it and was open in top and bottom so that the drops could move freely upwards, but motion from the surrounding seawater would be restricted by the walls. With this concept and a 'high-definition' television camera they impressively managed to measure the rise rate and the dissolution rate of CO_2 drops rising several hundred meters.

Brewer et al. (2002) followed a single drop rising from 800 meters depth. During its rise a second drop was observed attached to the drop, but no change in rise velocity was noticed and it was possible to measure the properties of each drop individually (Brewer et al. 2002).

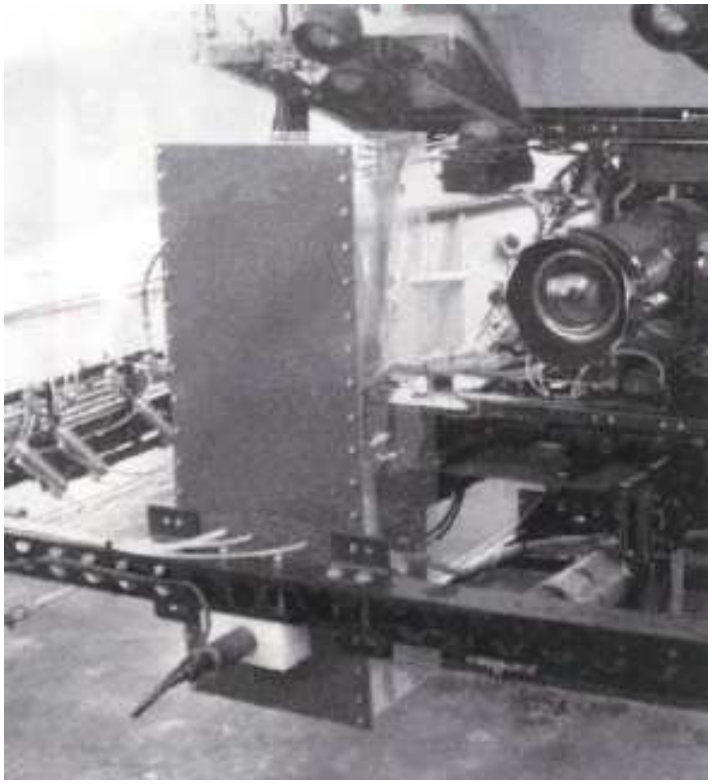

Figure 4.1: *The ROV with the imaging box used in the ocean experiment (Brewer et al. 2002).*

The drop released at 800 m depth is included in this thesis. It was followed for nearly 45 minutes until it reached a depth of about 500 meters. The temperature of the surrounding water was 4.4 ^{o}C at 800 m and increased upwards, to 5.4 ^{o}C at 500 m. Under conditions where the temperature is below 10 ^{o}C and the depths are below 200-400 meters, hydrate formation is expected to take place. When formed on a CO_2 drop of liquid phase, the hydrate is transparent and solid. Spherical drop shape and stiffness of the drop surface indicate that hydrate is present (Brewer et al. 2002). Brewer et al. (2002) observed that the drops where deformed by the delivery tube and had a stick like shape initially, but that they got more rounded as they rose. They concluded that hydrate formation took place.

The drop had an initial diameter and mass of $8.9{\cdot}10^{-3}$ m and $3.47{\cdot}10^{-4}$ kg respectively, which decreased to $1.6{\cdot}10^{-3}$ m and $2.2{\cdot}10^{-6}$ kg as the drop dissolved. The CO_2 density, ρ_{CO_2} [kgm^{-3}], decreased from about 939 kgm^{-3} to 905 kgm^{-3}, while the drop velocity increased slightly from a value of 0.102 to 0.135 ms^{-1}. Observed characteristics of the seawater and the drop are shown in Table 4.1. (The CO_2 densities in the table differ slightly from the values reported in Brewer et al. (2002) as another method is used here to calculate densities (see Appendix A4 for further details). This has no important impact on the result.)

Depth [m]	Time [s]	Temperature [^oC]	Diameter [m]	Mass [kg]	ρ_{CO_2} [kgm^{-3}]	Velocity [ms^{-1}]
804.5	0	4.398	0.0089	$3.47{\cdot}10^{-4}$	939.2	0.102
706.3	853.8	4.740	0.00606	$1.09{\cdot}10^{-4}$	929.4	0.113
649.1	1387.8	4.994	0.00485	$5.5{\cdot}10^{-5}$	923.3	0.120
602.1	1789.2	5.165	0.00364	$2.3{\cdot}10^{-5}$	917.9	0.125
496.8	2584.8	5.449	0.00162	$2.2{\cdot}10^{-6}$	905.3	0.135

Table 4.1: *Observations from the ocean experiment by Brewer et al. (2002).*

4.1.1 Estimated seawater density and dimensionless numbers

The salinity of the seawater was not given in the paper by Brewer et al. (2002) and a constant value of 35.0 psu has been used here to calculate the seawater density $\rho_{sw} = \rho_{sw}(S,T,P)$ (see Appendix A). The temperature was assumed to increase linearly, based on the data from Brewer et al. (2002) shown in table 4.1. The density and temperature profiles are presented in Figure 4.2.

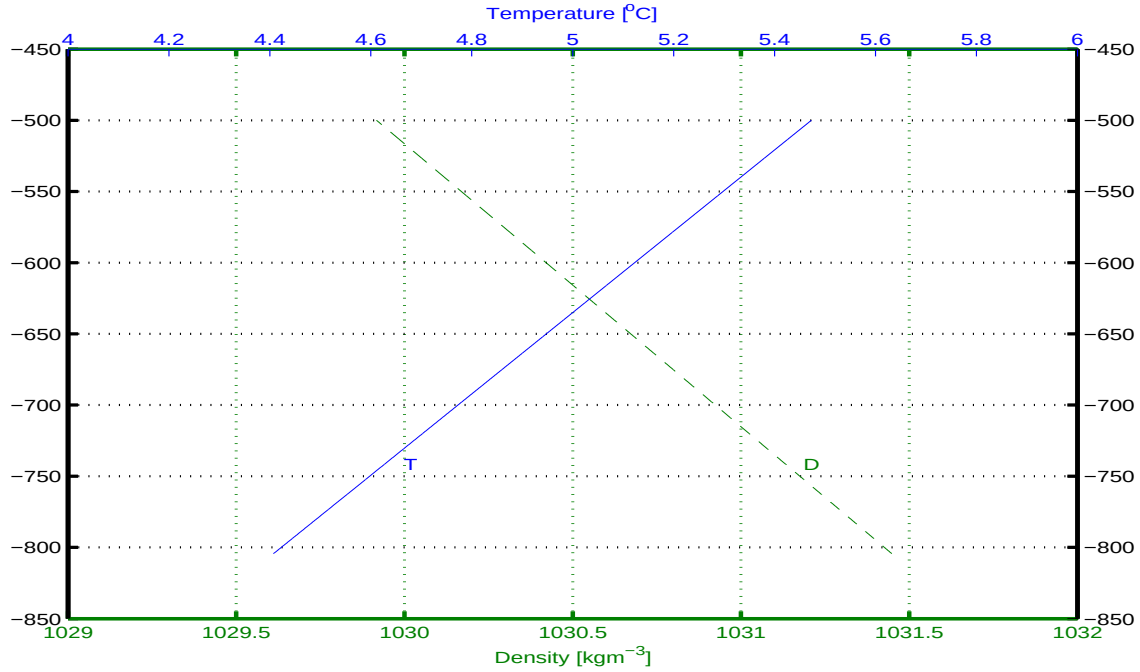

Figure 4.2: *Density and temperature profiles, with salinity $S = 35$ psu.*

From the estimated seawater density and the observations in Table 4.1 the dimensionless numbers the Reynolds, Eotvos and Morton number (see Section 3.1) are calculated. The Reynolds number ($Re = Ud\rho_{sw}\mu_{sw}^{-1}$) has values of between 200 and 900 while the Eotvos ($Eo = g(\rho_{sw} - \rho_{CO_2})d^2\sigma^{-1}$) decreases from 3.1 to 1.1. Finally, the Morton number ($Mo = g\mu_{sw}^4(\rho_{sw} - \rho_{CO_2})\rho_{sw}^{-2}\sigma^{-3}$) has a value around $1{\cdot}10^{-10}$. In the calculations a seawater vis-

cosity of $\mu_{sw} = 1.075 \cdot 10^{-3}\ kgm^{-1}s^{-1}$ is use and the surface tension σ is set equal to 0.023 Nm^{-1}. The dimensionless numbers calculated at each observational depth are included in Table 4.2 together with seawater density. These numbers will be used in Section 4.3.3.

Depth [m]	$\rho_{sw}[kgm^{-3}]$	Morton number [1]	Eotvos number [1]	Reynolds number [1]
804.5	1031.4	$9.3366 \cdot 10^{-11}$	3.1167	871.02
706.3	1031.0	$1.0288 \cdot 10^{-10}$	1.5908	656.73
649.1	1030.7	$1.0883 \cdot 10^{-10}$	1.0772	558.00
602.1	1030.4	$1.1412 \cdot 10^{-10}$	0.6359	436.14
496.8	1029.9	$1.2650 \cdot 10^{-10}$	0.1395	209.53

Table 4.2: *Seawater density and the dimensionless numbers.*

4.2 Terminal velocity

As the acceleration in the experiment is assumed to be instantaneous, the response time is neglected (Chapter 3). The drop velocity is thus at all times equal to the terminal velocity:

$$U_T = \left(\frac{8gr(\rho_{sw} - \rho_{CO_2})}{3C_d\rho_{sw}}\right)^{0.5}. \tag{4.1}$$

In the previous section we found all the data needed in equation 4.1 to calculate the terminal velocity, except from the drag coefficient, C_d. Results from laboratory work have shown that drops covered with a hydrate shell get a spherical shape. It has been suggested (Hirai et al. 1997, Mori 1998) that hydrate-covered drops behave as rigid spheres. It would thus be appropriate to use values for C_d from the standard drag curve (Figure 3.2). As the Reynolds numbers in this case are between 200 and 900, the approximation of the standard drag curve by Schiller & Naumann (1933) (equation 3.9) is used.

The drop terminal velocity calculated from equation 4.1 with data from Table 4.1 and C_d from equation 3.9 is shown in Figure 4.3 (solid line). The asterisks represent the observed velocity by Brewer et al. (2002). There obviously is a clear deviation between calculated and observed values. While the terminal velocity of the drop observed by Brewer et al. (2002) slightly increases as the drop size decreases, the calculated velocity decreases.

As the value of seawater density is not fully known, the sensitivity of terminal velocity to changed salinities was investigated. The seawater density was calculated with constant salinities of the values 34, 35 and 36 psu. Different values of constant seawater densities between 1028 and 1031 were also tried out. The results showed negligible effect on the drop velocity and the salinity value S = 35 psu is therefore further used.

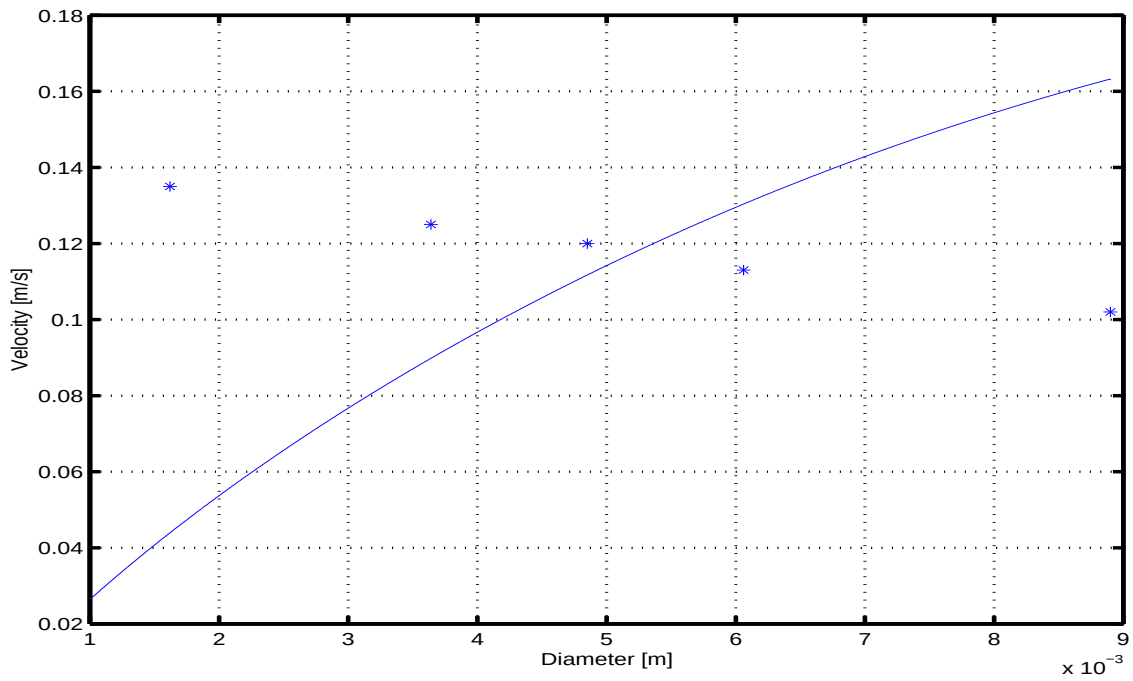

Figure 4.3: *Terminal velocity versus diameter calculated for rigid spheres (solid line) compared to observed drop velocity (asterisks).*

4.2.1 Drag coefficient needed to match the observed velocities

The values of the drag coefficient that would be needed for the calculated velocities to fit those observed by Brewer et al. (2002) (Table 4.1) can be found by equation 4.1. These are shown in Table 4.3 together with the corresponding Reynolds numbers.

Reynolds number [1]	Drag coefficient C_d [1]
871.02	1.0007
656.73	0.6115
558.0	0.4589
436.14	0.3328
209.53	0.1407

Table 4.3: *Reynolds number and drag coefficient for the observed drop.*

Figure 4.4 shows the drag from Table 4.3 plotted as asterisks, compared to an approximation (Schiller & Naumann 1933) of the standard drag curve (equation 3.9). The stippled line is a third degree adjustment to the calculation points, found by:

$$C_d = 5.8 \cdot 10^{-10} Re^3 + 2.1 \cdot 10^{-7} Re^2 + 5.0 \cdot 10^{-4} Re + 0.0215. \quad (4.2)$$

There is clearly a lack of compatibility between the calculated drag and the standard drag

curve of a rigid sphere. To achieve the observed terminal velocities using equation 4.1, the drag coefficient must decrease as Re decreases, not increase as with the standard drag curve.

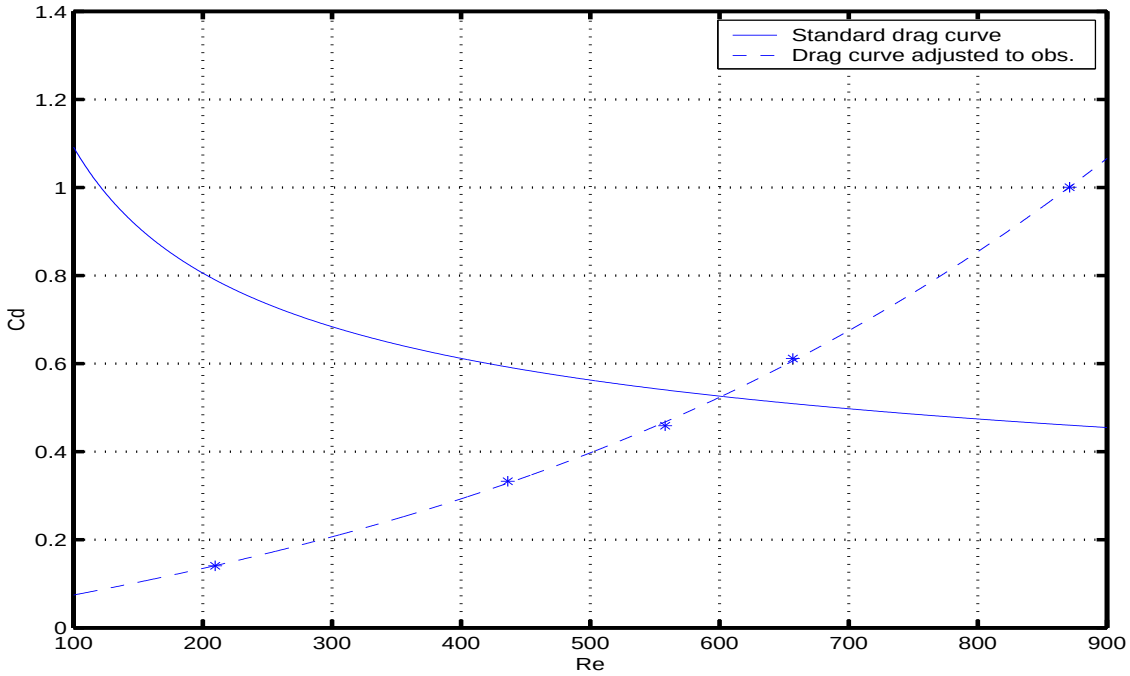

Figure 4.4: *Drag adjusted to the data from Table 4.3 (dotted line) compared to standard drag curve (solid line).*

The drop velocity calculated using values of C_d from the adjusted drag curve in figure 4.4 is shown together with the observed velocity in Figure 4.5. Theories that supports this drag curve will be explored in Section 4.2.3.

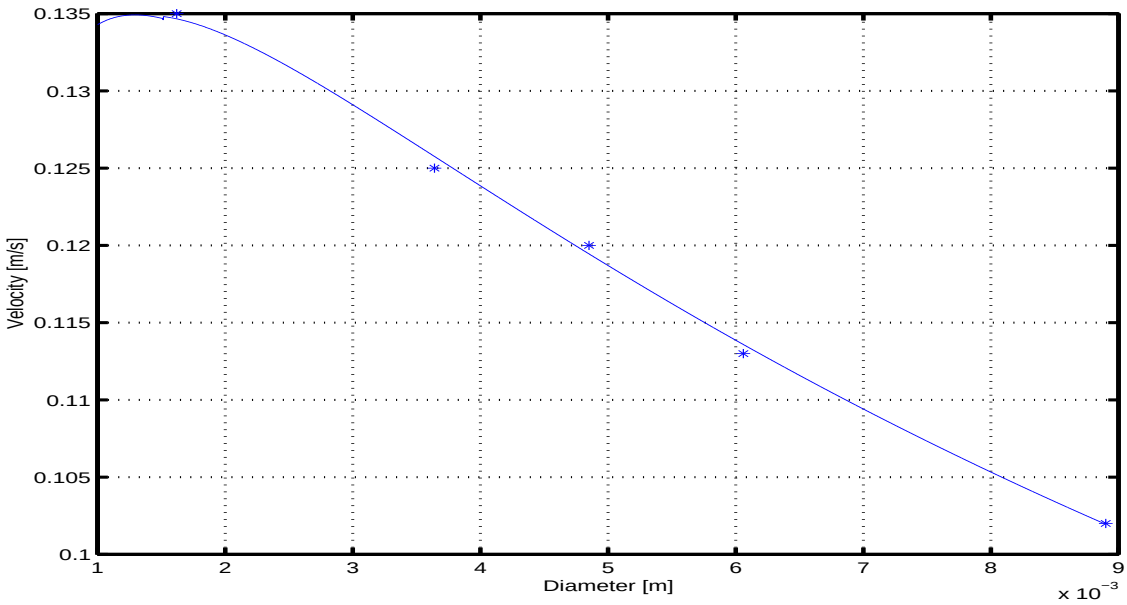

Figure 4.5: *Modelled velocity versus diameter compared to the properties of the observed drop.*

4.2.2 Drag influencing factors

Factors that may affect the drag are studied next, to search for possible explanations for the deviation in drag from the standard drag curve that was seen in Figure 4.4.

Surface and interfacial tension

Surface tension was defined in Chapter 3 as force per unit length across a line drawn on the interface, in a direction normal to the line and tangential to the interface. When the surface tension force has a constant value it works to reduce the surface energy and therefore tends to keep a fluid particle spherical in shape. Motion, pressure and temperature variations could overcome the stabilizing power of surface tension and cause deformation.

When studying a single drop with hydrate formation on its surface it is of interest to look at the properties at the interface between the liquid CO_2 and the surrounding seawater. These properties can be described by the interfacial tension σ, as the surface tension is then measured between different phases. (Earlier σ was referred to as surface tension in for instance the Eotvos number, but it will from now on only denote interfacial tension.) When liquid CO_2 is injected into the ocean under hydrate-forming conditions the interfacial tension between these liquids is difficult to estimate.

Many attempts have been made to measure and calculate interfacial tension. Uchida & Kawabata (1997) measured the interfacial tension between CO_2 and water, both with and

without a hydrate film. They found that when a hydrate shell existed, the interfacial tension was 26% less than without hydrate formation. They calculated it to be 0.021 Nm^{-1} for temperatures of about 7 ^oC and pressures above 4.45 MPa ($\sim$445 m). Ohmura & Mori (1998) estimated the interfacial tension between seawater and liquid CO_2 to be 0.024 Nm^{-1}, at depths of 3300-4000 m. Chun & Wilkinson (1995) measured the interfacial tension between CO_2 and water at different temperatures and pressures, but no hydrate formation was observed to take place in their experiment. They found that as the liquid drop reached the point where it started to evaporate, the interfacial tension was reduced for then to increase noticeably after this point. The interfacial tension between 8.27 MPa and 4.83 MPa and at 5 ^oC (equal to the pressures and temperatures of the seawater surrounding 'our' drop) varied around 0.021-0.0223 Nm^{-1}, while at 3.44 MPa and 3.79 MPa it was 0.0456 and 0.0429 Nm^{-1}, respectively. Kuznetsova & Kvamme (2002) calculated the interfacial tensions of the liquid-liquid water-CO_2 interface to be 0.029 $\pm$ 0.06 and 0.031 $\pm$ 0.06 Nm^{-1} at 300 and 100 atm, respectively, using molecular dynamic simulations. The temperature was set to about 3 ^oC, but the pressure used would be too low for hydrate formation to occur. Uchida et al. (2003) measured the interfacial tension between liquid CO_2 and water at 5 ^oC and at 5 MPa to be about 0.030 Nm^{-1}. When water was replaced with a NaCl solution the interfacial tension was more than 10 % larger.

The different measurements and calculations show that the assumption of an interfacial tension of 0.023 Nm^{-1} used to calculate the dimensionless numbers (Table 4.2) was reasonable, but there are deviations and the interfacial tension is also shown to vary. Interfacial tension normally decreases with increasing temperature (Batchelor 1967), but it is generally assumed to increase with decreasing pressure (Uchida et al. 2003).

Turbulence

Another factor that influences the dynamics of bubbles and drops in the ocean is turbulence. Figure 3.3 from Crowe et al. (1998) shows the spread in data from different experiments where drag coefficients of drops and particles have been measured. These deviations mainly originate from experiments with turbulence. Torobin & Gauvin (1961) and Clamen & Gauvin (1969) investigated the effect of increasing the relative turbulence intensity in the free stream and provided the data shown in Figure 3.3 by three similar deviating curves at $Re \sim 3 \cdot 10^3$. The curve on the left of these three originates from an experiment with a relative turbulence intensity of 40%; this looks somewhat similar to the drag curve achieved in Figure 4.4. For the next two curves turbulence intensities of 30 and 20 % are used, respectively.

The drop observed by Brewer et al. (2002) was all the time inside of a box with vertical walls restricting influence from surrounding currents. However, when the box was moved upwards by the ROV, turbulent flow might have occurred along the walls that could have affected the drop. If the increasing terminal velocity shown in the data from Brewer et al. (2002) is to be explained by turbulence alone, the turbulence intensity seemingly have to be

even more than 40 % to fit the Reynolds numbers in our case.

Seawater lifted by the rising ROV

Seawater might to some extent move along and be lifted with the ROV and the imaging box. This would result in a smaller relative velocity between the drop and the seawater and thus less friction. With less friction the terminal velocity is higher. As this effect is likely to be larger for a small drop than for a large one, it might explain the slight increase in velocity that the drop achieved with decreasing size.

Phase and purity

As was seen in Figure 3.4 the purity of the surrounding water largely affects the drag. In contaminated water, accumulation of surface-active contaminants on the drop surface affects the shape and thus the drag (Clift et al. 1978).

The figure also shows a difference dependent on phase (gas/liquid/solid), especially at larger Reynolds numbers. The drag coefficient for a gas bubble approaches a higher value than the drag coefficient for a solid sphere. The curves become more and more similar with decreasing Reynolds number, showing that very small bubbles tend to behave like rigid spheres. A fluid particle of liquid phase (the drop in our case) would probably have drag coefficients somewhere between those of a bubble and a solid particle. With hydrate covering the drop it has been suggested that the fluid particle will behave more like a rigid one, but the exact drag curve of a drop rising in the free ocean is not known. Hydrate formation on the drop surface might also have similar effect as surface-active contaminants (Mori 1998).

Shape

As our drop is covered with hydrate it is assumed to have a quasi-rigid behaviour. It is nevertheless interesting to study the shape regime that the drop belongs to if the surface is taken as mobile. The shape regime can generally be found from the Morton, Eotvos and Reynolds numbers (Clift et al. 1978), given in Table 4.2. Figure 4.6 shows roughly in which regime our drop is located (shaded area). The drop seems to 'move' from the ellipsoidal regime into the spherical regime. As the drag of an ellipsoidal drop would be larger than the drag of a sphere, the drag would be larger in the beginning than in the end. This is compatible with the result that the drag coefficient should decrease with decreasing Reynolds number and decreasing size in order to match theory with observations (Figure 4.4).

Mori & Mochizuki (1998) comment that the laboratory results of a smooth hydrate film surrounding the whole drop surface might not be representative for a drop in the 'real' sea. Drops in the ocean would be subject to a viscous shear not taken into account in the laboratory experiments (Aya et al. 1992, Hirai et al. 1997). Mori & Mochizuki (1998) also report that in experiments using a velocity as high as 0.2 ms^{-1} hydrate was formed in tiny particles

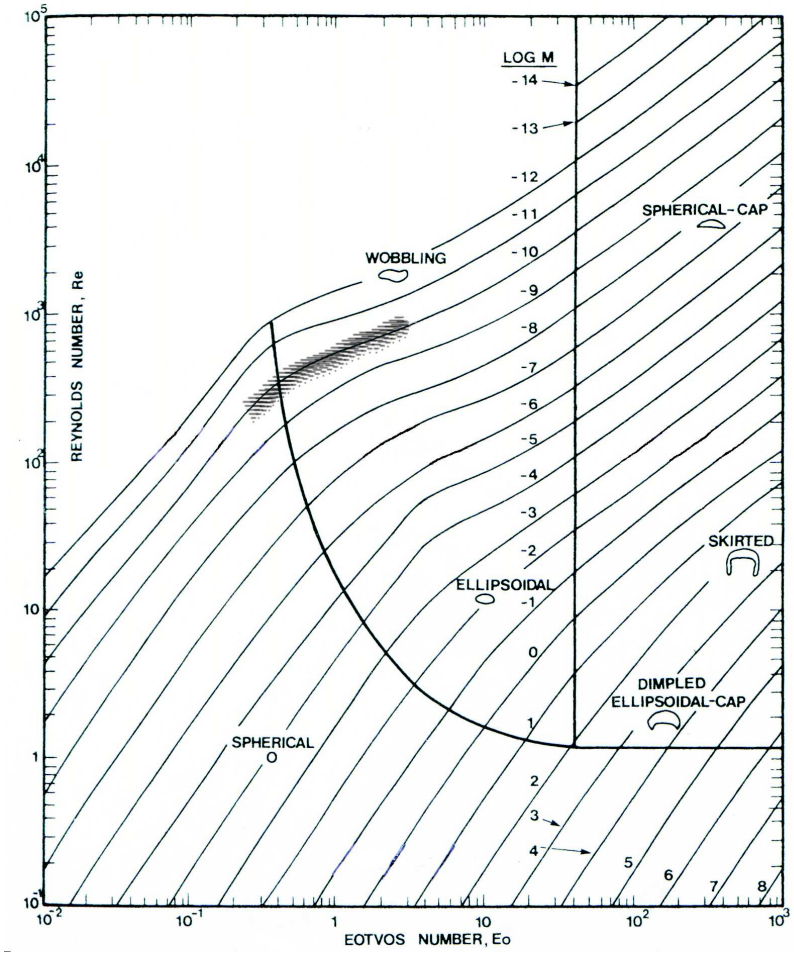

Figure 4.6: *Shape regimes of bubbles and drops (Clift et al. 1978) with the approximate Reynolds, Morton and Eotvos numbers of the drop from Table 4.1 included (shaded area).*

or flakes covering only parts of the drop, while in model calculations it is often assumed that the hydrate skin covers the whole surface evenly. During interfacial tension studies of CO_2 drops by Chun & Wilkinson (1995) hydrate formation was not even observed in spite of suiting conditions.

The uncertainties concerning hydrate formation mentioned above support the possibility that the surface of the drop observed by Brewer et al. (2002) might have been at least partly mobile and that some deformation could have occurred. Brewer et al. (2002) reported gradual transition to spherical shape but they did not report at which stage this was fully achieved. Hence change of shape and thus in drag coefficient might be one explanation for the deviation between the calculated and the observed velocity.

4.2.3 Comparing theories of dynamics

Following the assumption that deformation is a main reason for the deviation in drag from the standard drag curve, we have to use a drag that fairly well matches the terminal velocity that was observed by Brewer et al. (2002). Both Grace et al. (1976) and Bozzano & Dente (2001) take into account a varying shape by including the dimensionless numbers Mo, Eo, and Re in their theories of dynamics (Chapter 3). Their theories could then possibly be used.

The theory by Grace et al. (1976) was found in Clift et al. (1978) and is a classical theory based on laboratory work on bubbles and drops. The terminal velocity calculated when using these equations (3.16-3.15) is shown in Figure 4.7 as the stippled-dotted line. It fits the first two observational points (asterisks), but the velocity decreases right after the second point. The equations are used with a constant value of interfacial tension of 0.023 Nm^{-1}. As the value of interfacial tension might vary (Section 4.2.2), different values of interfacial tension were tried out. It was however not possible to match calculated values with observed ones. This theory was originally developed for bubbles and drops in contaminated water. Grace et al. (1976) also developed a correlation for purer systems by modifying the correlation they found for contaminated systems with a correction factor λ that must be obtained experimentally. A figure showing this correction factor found from a number of laboratory experiments is given in Clift et al. (1978), but no function is offered for the curve to use. The correction factor λ could be calculated in our case, but to find a perfectly fitting curve was difficult due to the very few observational points that we have.

The theory with standard drag is also included in Figure 4.7 (solid line). The theory by Grace et al. (1976) gives velocities that fit the observations better than the theory with standard drag, but none of the theories provide a satisfying result.

The set of equations (3.20 - 3.23) given by Bozzano & Dente (2001) was then found and tried out. The equations were originally developed for gas bubbles and Bozzano & Dente (2001) had chosen the density difference between seawater and the bubble to be equal to the density of seawater in the Morton number. This is a reasonable approximation for gas bubbles where the density difference is large, but for liquid drops in seawater the density difference is small and the approximation is not valid. The original definition of the Morton number (equation 3.5) was therefore used in our case. The result is presented as the stippled line in Figure 4.7.

Of the results shown in Figure 4.7, those found with the equations by Bozzano & Dente (2001) evidently match the observed data best. Here the terminal velocity increases as the drop dissolves, approximately following the observational points. The exception is the last point, where a marked deviation is seen. That the last point was impossible to match could be explained by the fact that this is where the drop is at its smallest and the measurement errors would be largest. Possible turbulence and lifted seawater caused by the rising imaging box in the experiment could be other explanations for the deviation, at least partly.

The values of interfacial tension that would be needed to get an exact fit was calculated

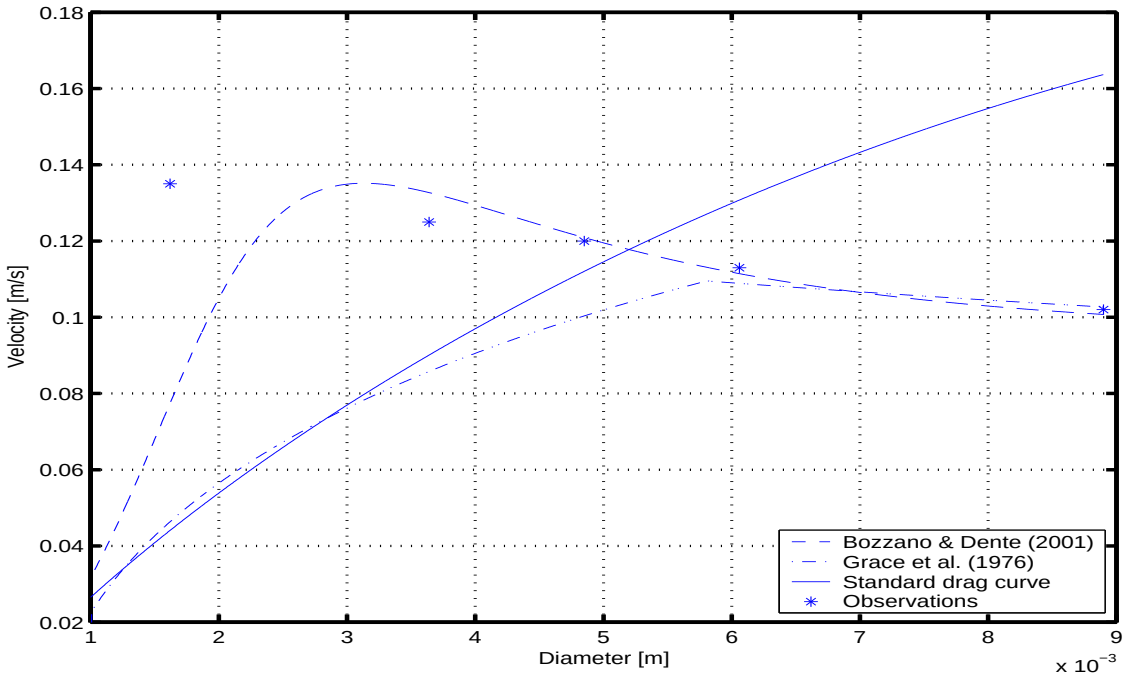

Figure 4.7: *Terminal velocity with diameter using the three different theories of dynamics.*

and are shown in Table 4.4.

Depth [m]	Interfacial tension $[Nm^{-1}]$	Drag coefficient [1]	Morton number [1]	Eotvos number [1]
804.5	0.0240	1.000	$8.214 \cdot 10^{-11}$	2.985
706.3	0.0238	0.612	$9.247 \cdot 10^{-11}$	1.536
649.1	0.0227	0.459	$1.139 \cdot 10^{-10}$	1.094
602.1	0.0203	0.333	$1.664 \cdot 10^{-10}$	0.721

Table 4.4: *Interfacial tension, drag coefficient and dimensionless numbers that match the theory of Bozzano & Dente (2001).*

Only the first four values were possible to find as the last calculated velocity point deviated that much from the observed velocity. As is seen from the table the values do not differ much from the original value of 0.023 Nm^{-1} and they decrease with decreasing Eotvos number (size).

The dynamical theory by Bozzano & Dente (2001) still fits reasonably well without changing the interfacial tension (Figure 4.7). Their equations are therefore chosen to be used further. The theory with standard drag of solid spherical drops will be included later for comparison.

4.3 Mass transfer

Mass transfer is an important mechanism in the CO_2 drop-seawater system. Especially from an environmental perspective it is essential to know how fast CO_2 dissolves. Under conditions where hydrate formation can take place, a hydrate film surrounding the drop will act to reduce the dissolution rate and thus make the time that the drop uses to dissolve longer. With hydrate formation the mass transfer is also dependent on temperature (Aya et al. 1997). The dissolution rate is nearly independent on temperature without a hydrate film surrounding the drop. Another important factor that affects dissolution is velocity, mass transfer increases with increase in velocity. Turbulence would in addition increase the rate of transfer at all Reynolds numbers (Clift et al. 1978). Two ways to calculate mass transfer will be introduced next.

Constant dissolution rate

Brewer et al. (2002) found that the observed mass transfer could be matched with a constant dissolution rate. Using the least square method and the observational data they calculated the dissolution rate Γ from the slope of the equation:

$$(r - r_0) = -V_m \Gamma (t - t_0) \tag{4.3}$$

where r_0 and r are initial drop radius and drop radius at time t, and t_0 is initial time. From this Γ gets a value of 3.0 $\mu molcm^{-2}s^{-1}$ which equivalences a slightly increasing dissolution rate $\frac{dr}{dt}$ of $1.41 - 1.46 \cdot 10^{-6}$ ms^{-1} (as the density of CO_2 is included in the transformation of dimensions). Figure 4.8 shows the calculated mass transfer (dotted line) together with the observed drop data (asterisks). This is the method used in the calculations in the previous section about terminal velocity.

The Ranz-Marshall correlation

A method that includes the varying drop terminal velocity is also tried out. This theory is a product of using the Ranz-Marshall correlation, and it is commonly used to calculate the dissolution rate of drops (Radhakrishnan et al. 2003, Sato & Sato 2002, Hirai et al. 1997, Mori & Mochizuki 1998). Here the Sherwood number:

$$Sh = 2 + 0.69 Re^{0.5} Sc^{0.33} \tag{4.4}$$

is used in connection with equation 3.29 (see Chapter 3 for more details about the Ranz-Marshall correlation). In this method it is necessary to include the effect of hydrate formation. How much the hydrate reduces the dissolution rate is not quite clear, and it also depends on the thickness of the hydrate film. It has been shown that in cases with hydrate formation the shrinking rate is about half of what it is without hydrate formation (Aya

et al. 1992, Nishikawa et al. 1995). A value of the reduction factor equal to 2 was also found in an experiment performed by Aya et al. (1997). Holder & Warzinski (1996) calculated that a reduction of a factor of 3 was needed for hydrate-covered CO_2 drops released at 1000 m depth. As the first term (= 2) in the right hand side of equation 4.4 is the analytical limiting value (the Sherwood number is equal to 2 when there is no net flow around the drop), this value is not included when calculating the reduced dissolution rate. The second term is then divided by a reduction factor RF and the Sherwood number becomes:

$$Sh = 2 + \frac{0.69}{RF} Re^{0.5} Sc^{0.33} \tag{4.5}$$

Figure 4.8 shows a plot with the original Ranz-Marshall correlation and with reduction factors of 2 and 3 including the observed drop data. As is seen in the figure, using the

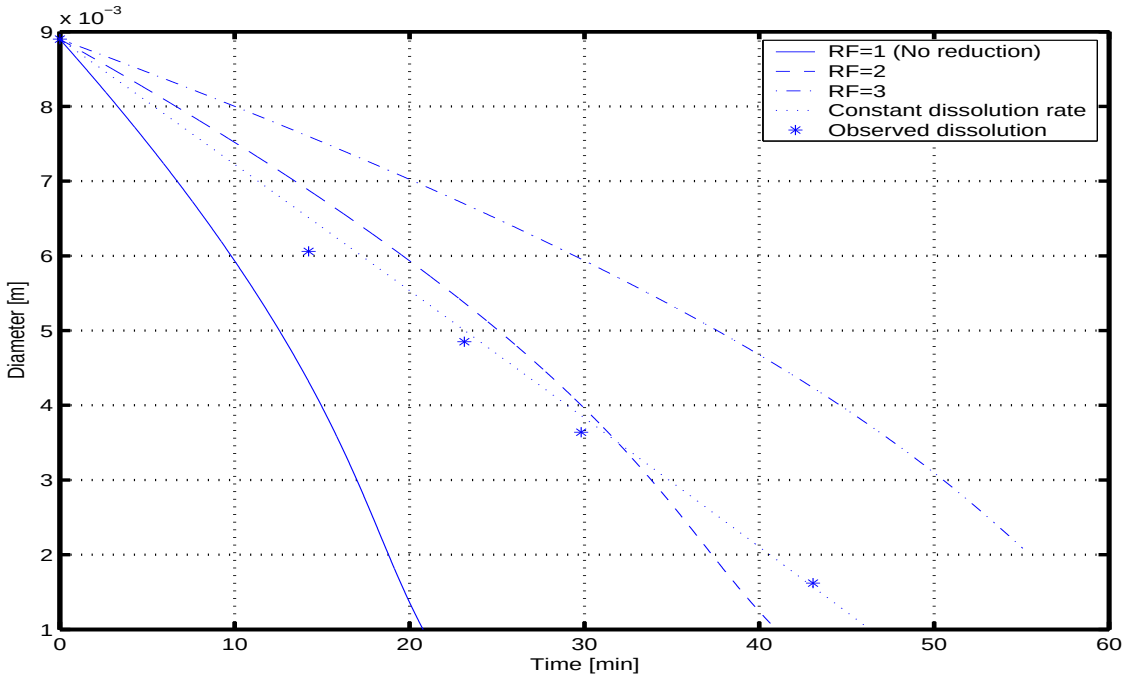

Figure 4.8: *Diameter versus time for calculated mass transfer including reduction factors to account for hydrate formation.*

Ranz-Marshall correlation does not match the observed mass loss as well as the constant dissolution rate by Brewer et al. (2002), but a reduction factor of 2 fits best. Hence, it is suggested that hydrate reduces the mass transfer of this CO_2 drop approximately by a factor of 2. With a reduction factor of 2 the Sherwood number becomes:

$$Sh = 2 + 0.35 Re^{0.5} Sc^{0.33} \tag{4.6}$$

The constant dissolution rate of 3.0 $\mu molcm^{-2}s^{-1}$ resulting from the experiment by Brewer et al. (2002) will be used further throughout this thesis.

Chapter 5

Vertical distributions of dissolved CO_2

In this chapter the focus will be on spreading of dissolved CO_2 in the water column caused by dissolution of a varying number of CO_2 drops. The effects of initial drop size and release depth will be studied and the results of using the different theories of dynamics and mass transfer. Statistical probability distributions of drops will be compared in the end.

5.1 Model basics

The numerical model introduced in Chapter 4 (and more extensively described in Appendix A) is here used to simulate a range of single CO_2 drops released into the ocean. The model is set to run a certain amount of times with different initial drop sizes and the information about each drop is collected in a database.

To study vertical distributions of dissolved CO_2, a small modification of the numerical model was made. Originally the model provided data at a frequency determined by a chosen time step. Now the output data for each drop is instead given per meter. This is accomplished by dividing the vertical into boxes of 1 m sizes and storing the calculated mass loss of each drop in these boxes. The initial masses of the drops are also stored. The vertical spread of dissolved CO_2, equivalent to the mass loss of the simulated CO_2 drops, can now be presented.

The model run for each drop is stopped if the the minimum diameter is achieved, here this is set equal to 10^{-4} m. It is also stopped if the drop reaches the depth of 420 m, around which depth liquid drops would turn into gas bubbles. The bubbles are then assumed to quickly ascend to the surface, releasing the remaining CO_2 gas to the atmosphere. Whenever a drop reaches the depth of phase change, the mass of CO_2 remaining is collected and stored. The amount of CO_2 gas entering the atmosphere can then be estimated.

A Matlab program was made to handle the information from the database of dissolved CO_2 for the different initial drop sizes. To achieve the wanted probability distribution, collections with randomly distributed initial drop sizes are here generated. The columns with the right sizes in the database are then multiplied with the corresponding number of drops.

Now the amount of dissolved CO_2 from the entire drop distribution is found at every depth interval of the water column.

5.2 Monodispersed distributions

Before investigating statistical distributions of a number of drops with mean diameters and standard deviations, monodispersed distributions are considered, i.e. distributions where all the drops have the same, or close to the same, initial size.

5.2.1 Base case

In the base case the drop and seawater properties from the experiment by Brewer et al. (2002) and the initial data from the previous chapter is used. The exception is initial diameter which is here set to 6 mm in stead of 8.9 mm. The drops will be released from the depth of 800 meters. Based on the analysis made in Chapter 4, the theory of dynamics for deformed drops (Bozzano & Dente 2001) and a constant dissolution rate of 3.0 $\mu molcm^{-2}s^{-1}$ will be employed. The initial data and theories for the base case are summarized in Table 5.1.

Initial diameter [m]	0.006
Theory of dynamics	Bozzano & Dente (2001)
Dissolution rate [$\mu molcm^{-2}s^{-1}$]	Constant = 3.0
Initial depth [m]	800

Table 5.1: *Initial values and theories used in the base case.*

A demonstration of the single drop model using varying theories of dynamics and mass transfer was given in the former chapter. Using the data and methods in Table 5.1, time and diameter for this drop are plotted as a function of depth and shown in Figure 5.1. As is seen in the figure the drop uses about 35 minutes to dissolve and reaches a depth of 600 meters.

A plot of the vertical distribution of dissolved CO_2 for the base case drop is shown in Figure 5.2. The mass of dissolved CO_2 per meter is divided by the initial mass of the drop so that the depth integral of the total curve is equal to one. By doing so, vertical distributions of different cases can easily be compared. The vertical distribution of dissolved CO_2 from one single drop of a certain size would then also be equal to the vertical distribution from a number of drops having the identical initial size. In this section concerning monodispersed distributions single drops will therefore be used.

The largest fraction of dissolved CO_2 per meter in Figure 5.2 is found at 800 meters and has a value of about 0.012 $[m^{-1}]$. The depth range of the spreading of dissolved CO_2 is 200 meters.

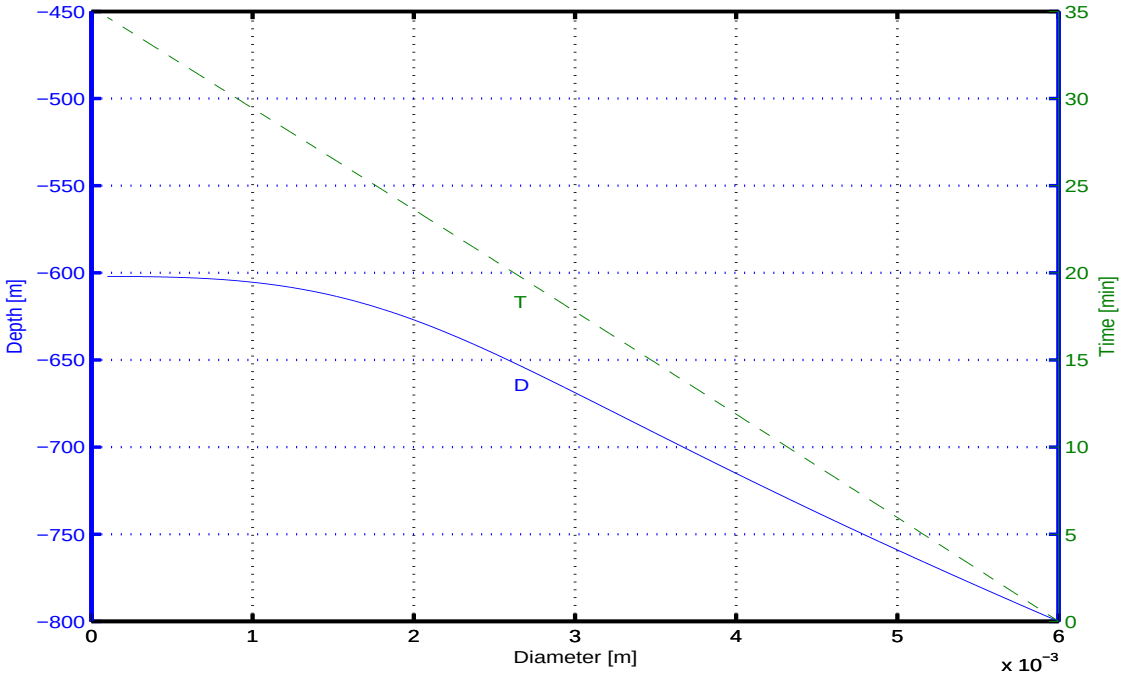

Figure 5.1: *Diameter with time (stippled line) and diameter with depth (solid line) for the base case drop.*

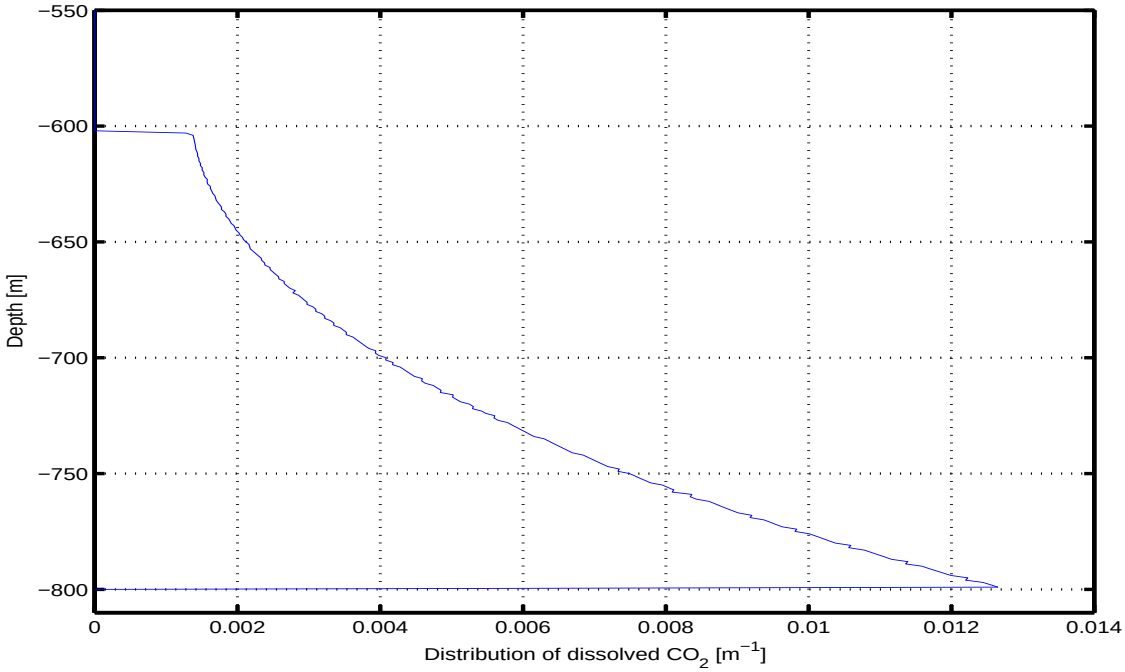

Figure 5.2: *Vertical distribution of dissolved CO_2 per meter for the base case drop.*

5.2.2 Initial diameter

The fate of CO_2 that is released into the ocean is greatly dependent on initial drop diameter (Haugan et al. 1995). The rising depth and time for 8 drops having initial diameters between 4 and 18 mm are shown in Figure 5.3. The largest drops are presented with stippled lines, the smallest with solid lines. The depth at which the drops enter the gas phase is shown as the horizontal line at about 420 meters. As can be seen the four largest drops, with diameters between 12 and 18 mm, reach this depth when they are released from 800 meters. The time from the drops are released until they are dissolved or have reached gas phase varies between about 20 and 60 minutes dependent on size.

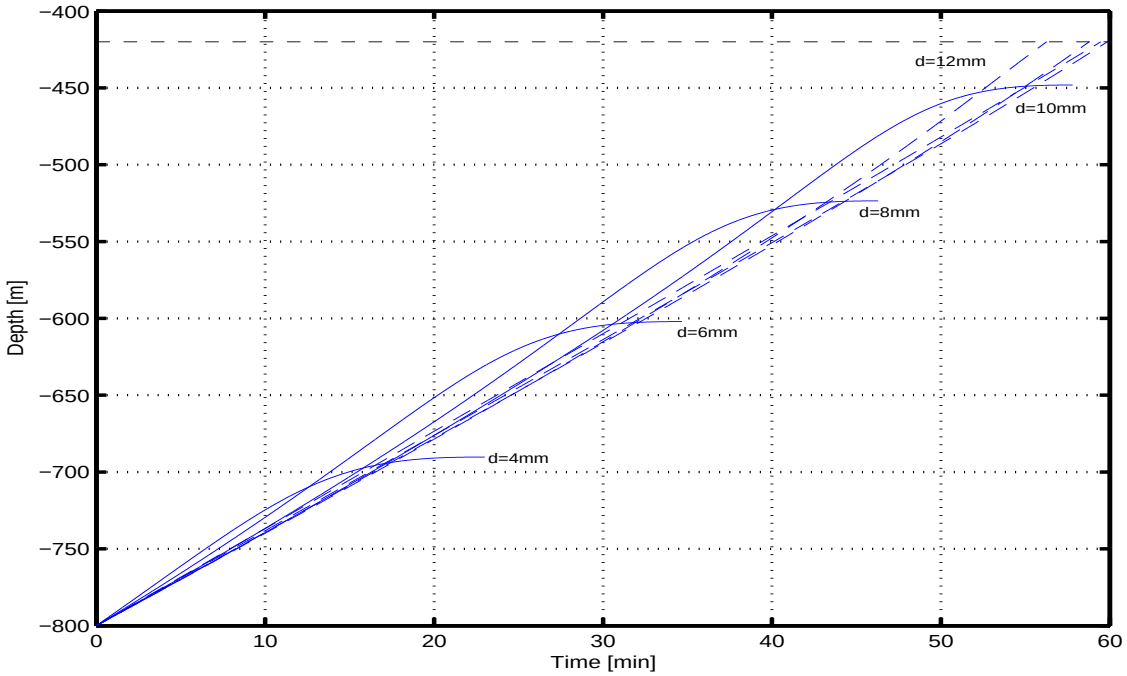

Figure 5.3: *Time and depth of 8 drops with diameters of 4, 6, 8, 10, 12, 14, 16 and 18 mm. The depth of phase change is shown as the horizontal stippled line. The four largest drops enter this depth and are also shown as stippled lines.*

In Figure 5.4 size reductions are plotted with drop velocities. Every drop has an initial velocity of between 10 and 13 cms^{-1} and gets a slightly increasing velocity at start. As the larger drops reach gas phase before they are fully dissolved, their maximum velocities are not achieved, but smaller drops get velocity tops around 13 and 14 cms^{-1}. Thereafter the velocities reduce down to zero as the drops get smaller. The largest drop with an initial diameter of 18 mm, seen in Figure 5.4 as the upper stippled line, only reduces its size to a diameter of 8 mm before experiencing transition to gas phase.

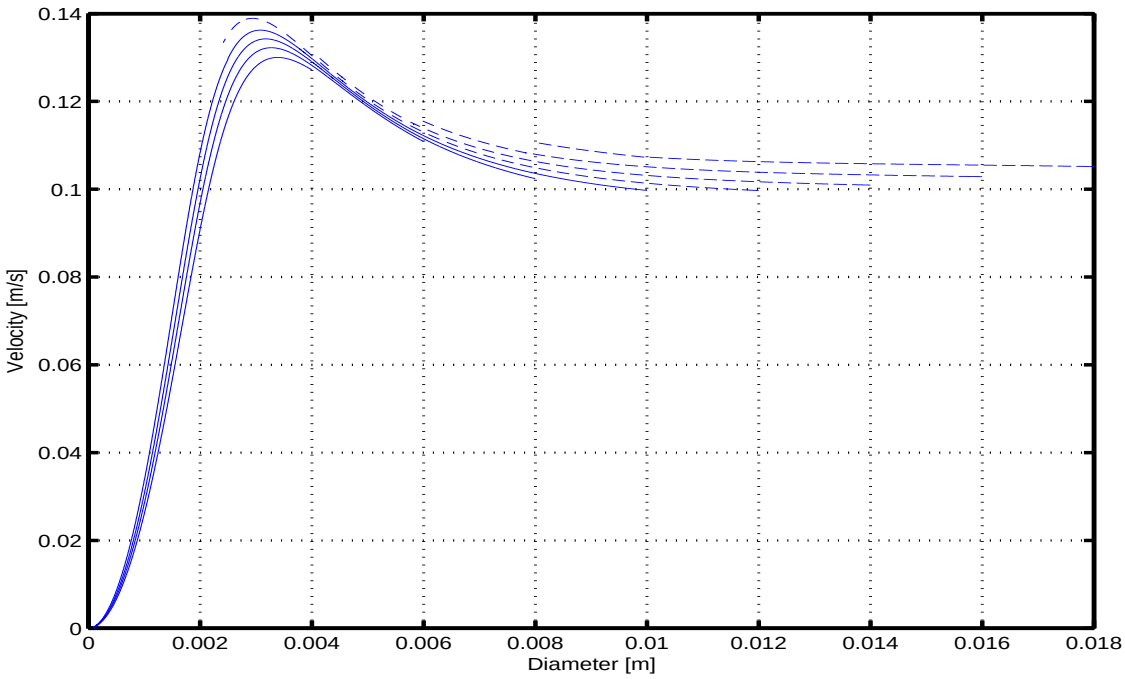

Figure 5.4: *The velocity plotted with diameter of the 8 different sized drops from Figure 5.3.*

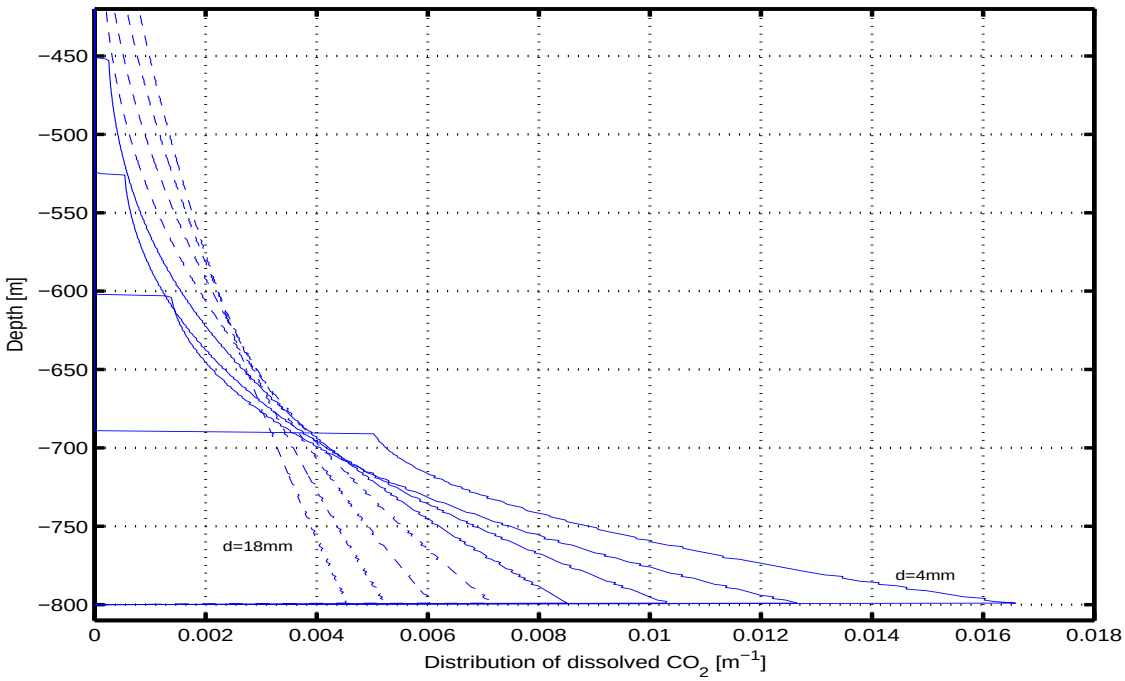

Figure 5.5: *Vertical distribution of dissolved CO_2 per meter for the 8 drops from the two previous figures.*

In Figure 5.5 the vertical distributions of dissolved CO_2 from the different 8 drops are plotted. The curve to the right represents the distribution of the drop with diameter 4 mm, the next curve represents the drop of diameter 6 mm etc.

The distribution of dissolved CO_2 is located deeper in the water column for smaller drops than for larger, as larger drops rise higher in the ocean. To give the least impact on the marine life, a large spread of dissolved CO_2 in the water column is preferred. At the same time the drops should not reach the depth of phase change. According to Figure 5.5 drops having initial diameters of 6-10 mm seem to provide the most favorable vertical distribution of dissolved CO_2, when the drops are released from 800 meters depth.

5.2.3 Theories of dynamics

In Chapter 4 the velocity patterns for the theory by Bozzano & Dente (2001) and the theory with standard drag were compared for the drop of diameter 8.9 mm (Figure 4.7). Here the analysis is extended. The effect of using the two methods with different initial drop sizes on the vertical distribution of dissolved CO_2 is studied.

In Figure 5.6 drop velocity is plotted as a function of drop diameter. As we know from Figure 5.3 the drops with diameters 4, 6, 8 and 10 mm will not enter gas phase when released from 800 meters depth, therefore the velocity patterns of these drops are included. The use of the theory of dynamics by Bozzano & Dente (2001) is presented as solid lines, the use of the theory with standard drag as stippled lines. When using the theory with standard drag the initial velocities show a much larger spread than when the theory by Bozzano & Dente (2001) is used. The velocities vary between 8 and 18 cms^{-1} initially before decreasing to zero.

The resulting distributions of dissolved CO_2 are shown in Figure 5.7. The solid lines represent the theory by Bozzano & Dente (2001), the stippled lines the theory with standard drag. Each drop size is shown in a separate plot to easily compare the two methods. Figure 5.7 a), representing a drop of diameter 4 mm, shows that the fraction of dissolved CO_2 is largest near the release depth when using the theory with standard drag. However for a drop of diameter 10 mm shown in Figure 5.7 d) the amount of dissolved CO_2 is largest near the release depth when using the theory by Bozzano & Dente (2001). For the base case drop of 6 mm and the drop with diameter 8 mm (Figures 5.7 b) and c)) the differences of using the two theories are smaller.

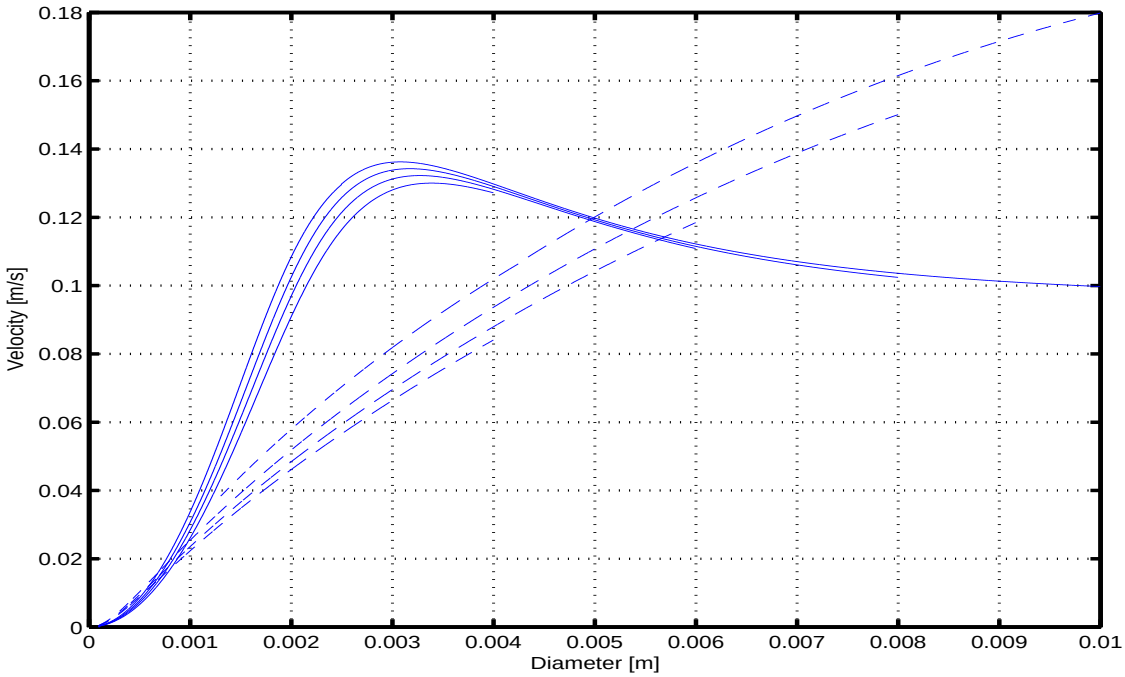

Figure 5.6: *Velocity with diameter for 4 different drop sizes, comparing the two theories of dynamics. Solid lines represent the theory by Bozzano & Dente (2001), stippled lines the theory with standard drag.*

The results can be explained by Figure 5.6. When having a drop of diameter 4 mm and using the theory with standard drag, the velocity is lower than when using the theory by Bozzano & Dente (2001). Then the drop rises a shorter distance during dissolution and we get a narrower vertical distribution of dissolved CO_2 located near the release depth. For a drop of diameter 10 mm the velocity is lowest when using the theory by Bozzano & Dente (2001), providing the narrowest distribution in the water column for this method. The drop velocities are more similar when using the two methods with drop sizes of 6 and 8 mm.

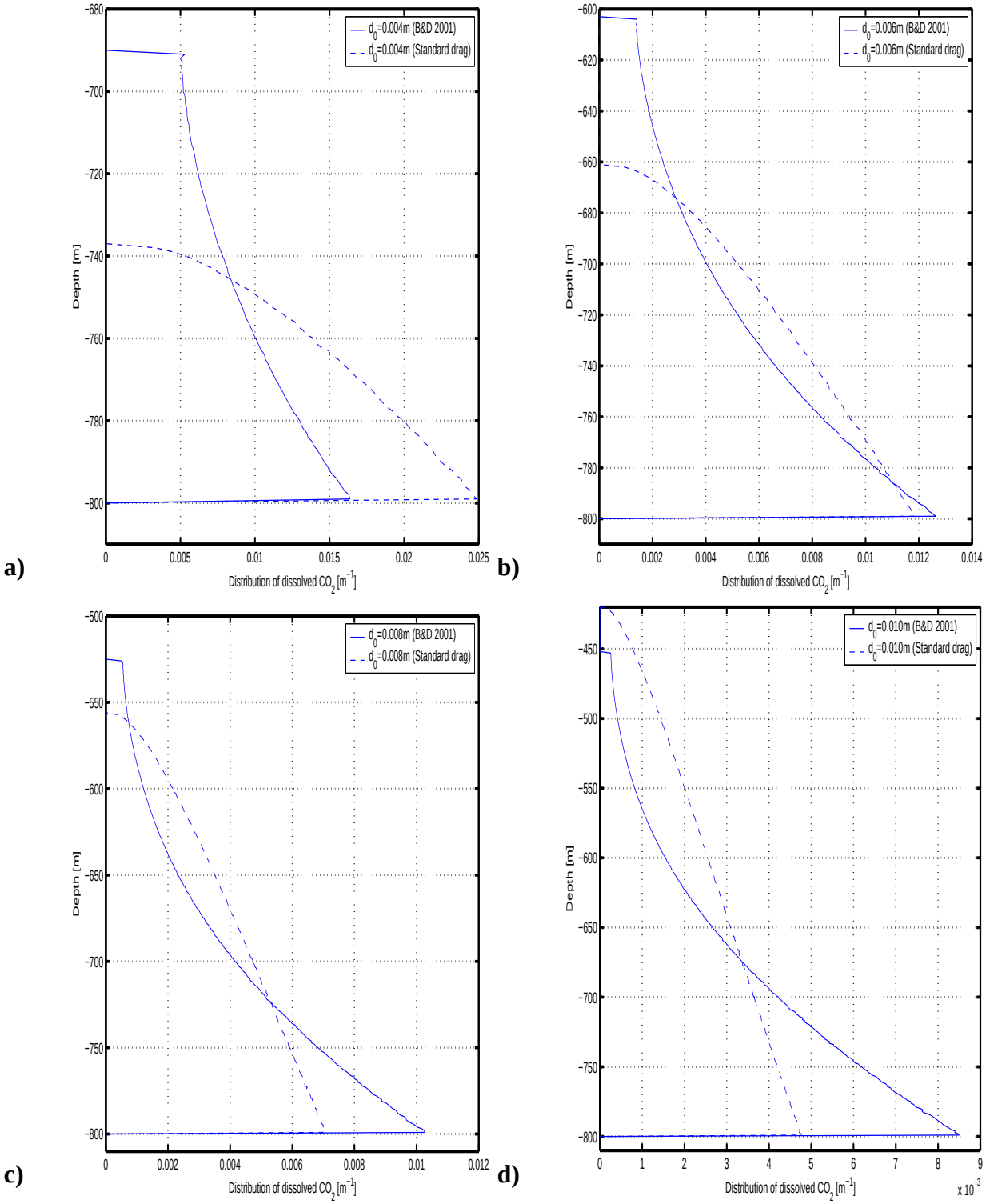

Figure 5.7: *Vertical distributions of dissolved CO_2 per meter when using the two theories of dynamics. The drop diameters are a) 4 mm, b) 6 mm, c) 8 mm and d) 10 mm. Solid lines represent the theory of Bozzano & Dente (2001), stipples lines the theory with standard drag.*

5.2.4 Dissolution rate

The effects of using the two methods to calculate mass transfer introduced in Chapter 4 will also shortly be presented. The constant dissolution rate, $\Gamma = 3.0\ \mu molcm^{-2}s^{-1}$, found by Brewer et al. (2002) was based on the observations of the single drop with initial diameter 8.9 mm. Whether this value of Γ is appropriate for drops under other conditions is not known. The effects of using the constant dissolution rate and the commonly used method with the Ranz-Marshall correlation are therefore studied.

Reductions of drop diameters with time for different initial drop sizes are seen in Figure 5.8, when the two theories are compared. In the case with the Ranz-Marshall correlation a reduction factor of 2 is used, based on the analysis in previous chapter. The results of using this theory are shown as the stippled line. As can be seen, for initially small drops the theory with the Ranz-Marshall correlation gives a faster dissolution. Initially large drops dissolve faster with the constant dissolution rate most of the time, but as they get smaller, again fastest when following the theory with the Ranz-Marshall correlation.

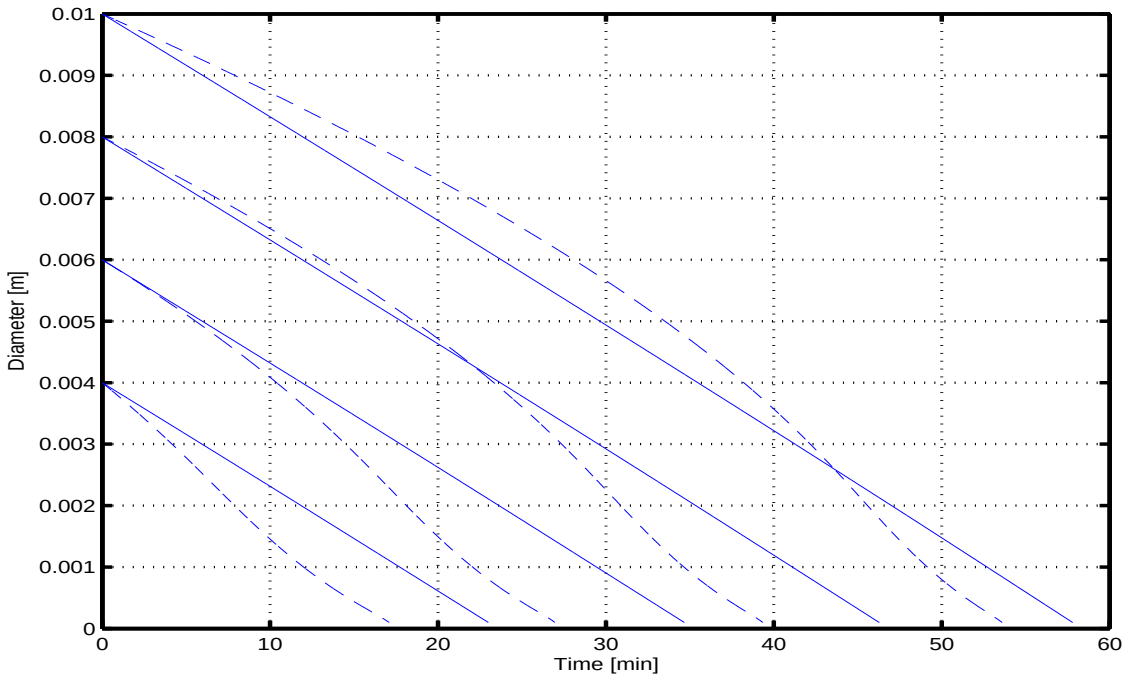

Figure 5.8: *Drop diameter with time for the 4 drops of diameter 4, 6, 8 and 10 mm, using the two mass transfer methods. Solid lines represent the use of a constant dissolution rate, stippled lines use of the theory with the Ranz-Marshall equation. The theory of dynamics by Bozzano & Dente (2001) is used.*

The resulting distribution of dissolved CO_2 for each initial drop size is shown in Figure 5.9. The constant dissolution rate is shown as the solid line, the Ranz-Marshall as the stippled line.

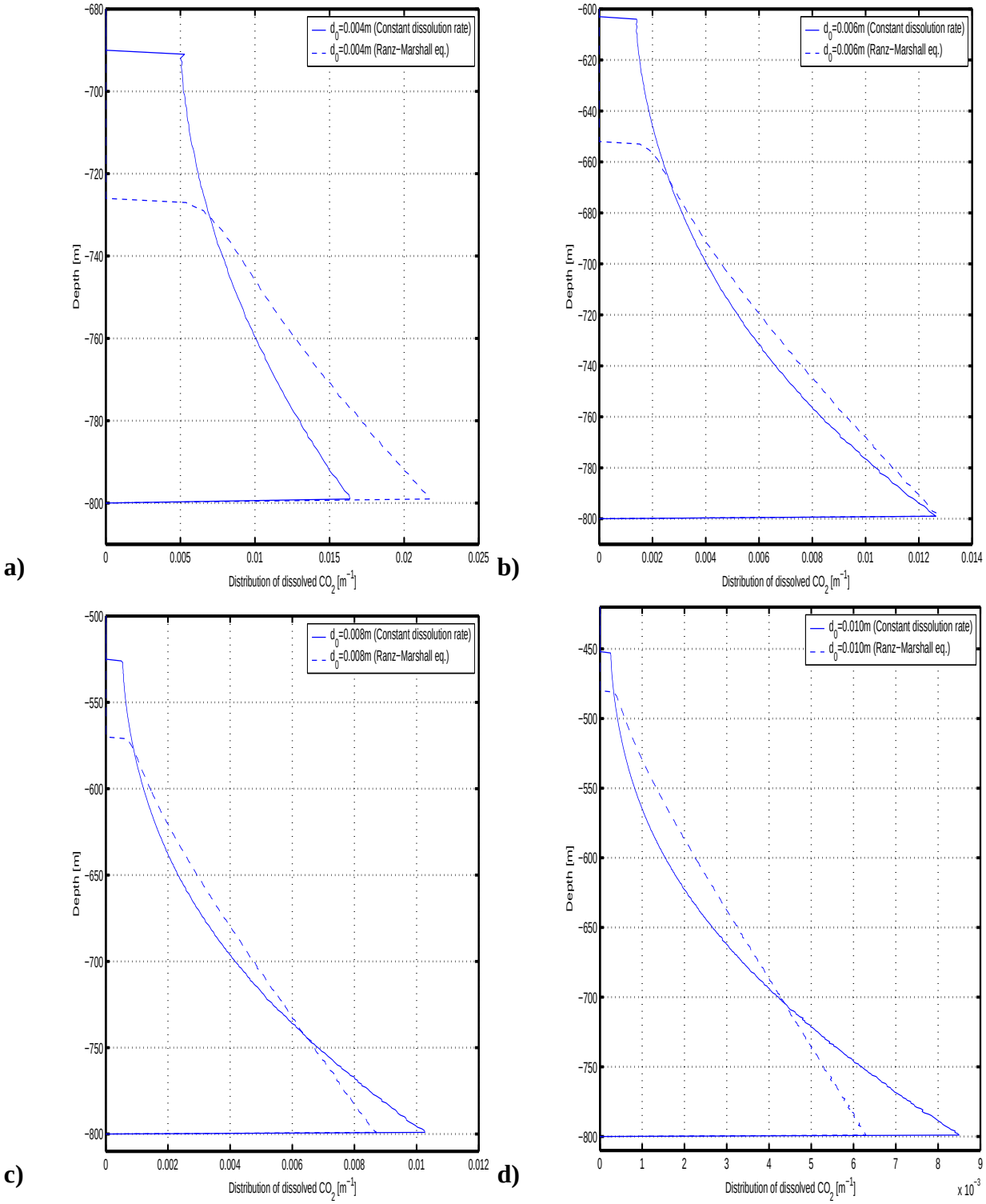

Figure 5.9: *Vertical distribution of dissolved CO_2 per meter corresponding to the cases in Figure 5.8. The drop diameters being a) 4 mm, b) 6 mm, c) 8 mm and d) 10 mm. Solid lines represent the constant dissolution rate, stippled lines the theory with the Ranz-Marshall correlation.*

For the smallest drop the fractional amount of dissolved CO_2 is largest near the release depth when the theory with the Ranz-Marshall correlation is used. With larger drops the method with constant dissolution rate provides the largest amount near the release depth. The method with constant dissolution rate however always gives the largest vertical spread of dissolved CO_2 for the drops sizes studied here. The effects of using the different mass transfer methods seems to be smaller than the effects of using the two theories of dynamics in previous section.

5.2.5 Initial depth

Until now all the drops have been released from the depth of 800 meters. The behaviour of drops released deeper in the ocean will be different and cause other distribution patterns of dissolved CO_2. The drops can also have a larger initial size without reaching the depth of phase change when they are released from a greater depth. Due to instability large drops normally split up into smaller drops. The exact maximum drop diameter that could occur in the ocean is not known. Bozzano & Dente (2001) suggested their theory of dynamics based on a number of laboratory experiments with bubbles. Most of the bubbles had diameters between 1 and 60 mm. In this thesis 60 mm is therefore the maximum diameter value studied.

In Figure 5.10 and 5.11 the fractional distributions of dissolved CO_2 are presented for drops with diameters 30, 40, 50 and 60 mm released at the depths of 1000, 1500, 2000 and 2500 meters. When the drops are released from the depth of 1000 meters distributions of dissolved CO_2 from all the drops are shown to reach the depth of phase change. From 1500 m the drops need to have a diameter of 40 mm to enter gas phase, from 2000 m they must be 50 mm or larger, while when released from 2500 meters the drops have to be larger than 60 mm to reach this depth. In Table 5.2 the rising distances of the drops from the vertical distributions in Figure 5.10 and 5.11 are summarized. For the drops that enter gas phase, the CO_2 gas that will reach the atmosphere is also included in the table, given in percent.

Diameter [m]	0.03	0.04	0.05	0.06
Rising distance [m] from 1000m	580.0	580.0	580.0	580.0
CO_2 gas to the atmosphere [%]	15.98	35.97	51.02	62.23
Rising distance [m] from 1500m	1056.6	1080.0	1080.1	1080.0
CO_2 gas to the atmosphere [%]	0	3.39	15.38	29.03
Rising distance [m] from 2000m	924.5	1314.9	1580.1	1580.1
CO_2 gas to the atmosphere [%]	0	0	0.24	5.09
Rising distance [m] from 2500m	795.3	1081.1	1428.4	1863.8
CO_2 gas to the atmosphere [%]	0	0	0	0

Table 5.2: *Traveling distance of the different drops from the vertical distributions in Figures 5.10 and 5.11 and the amount of CO_2 gas that reaches the atmosphere given in percent.*

a)

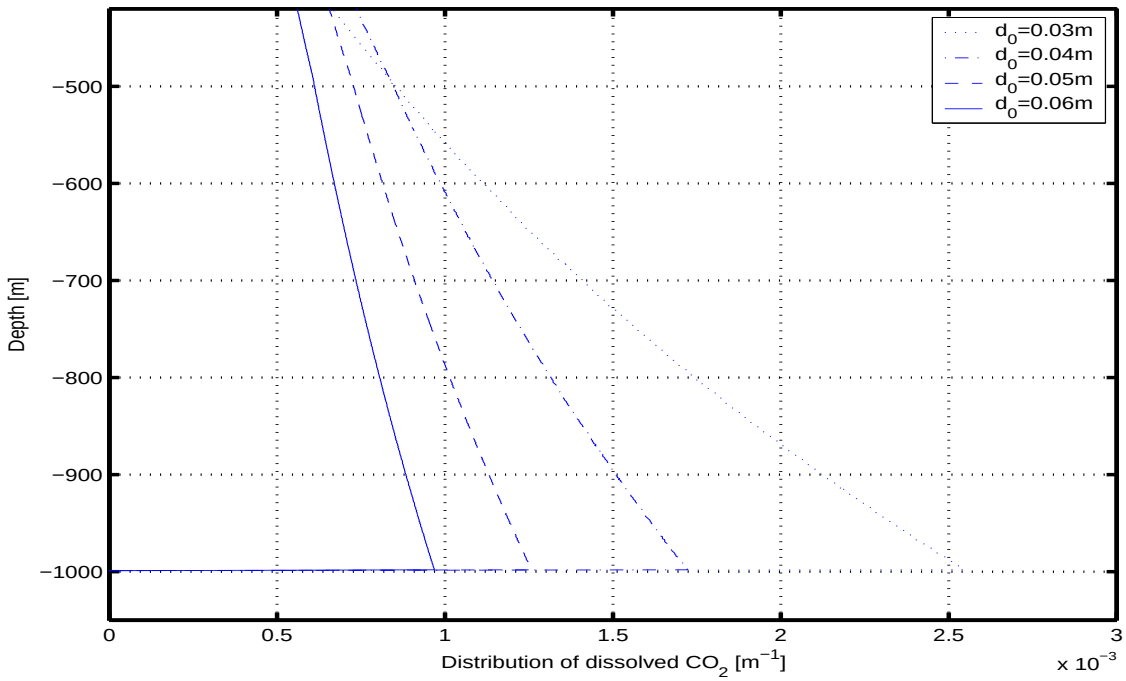

b)

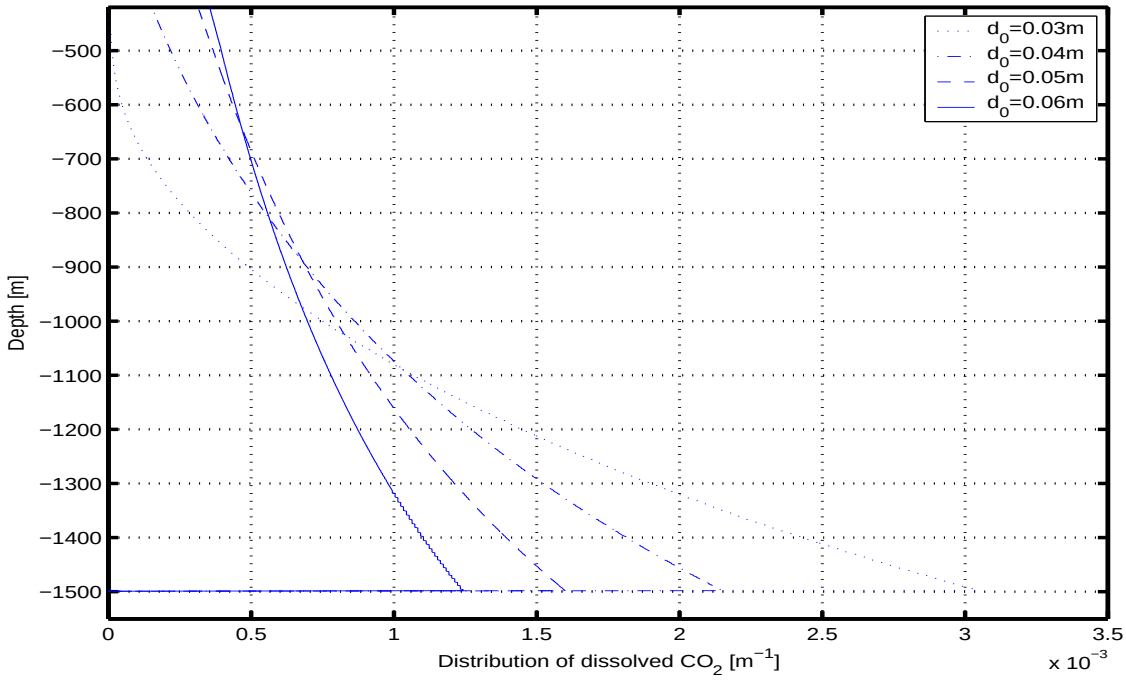

Figure 5.10: *Vertical distributions of dissolved CO_2 per meter for drops of four different sizes d_0 released from the depths of a) 1000 m and b) 1500 m.*

a)

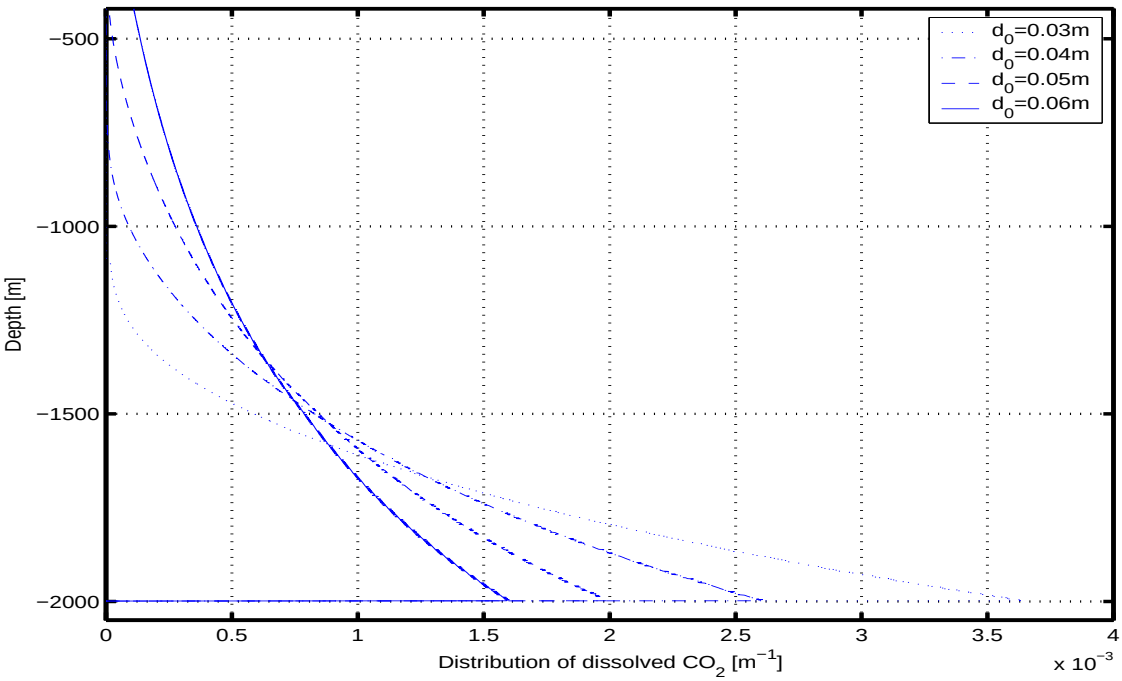

b)

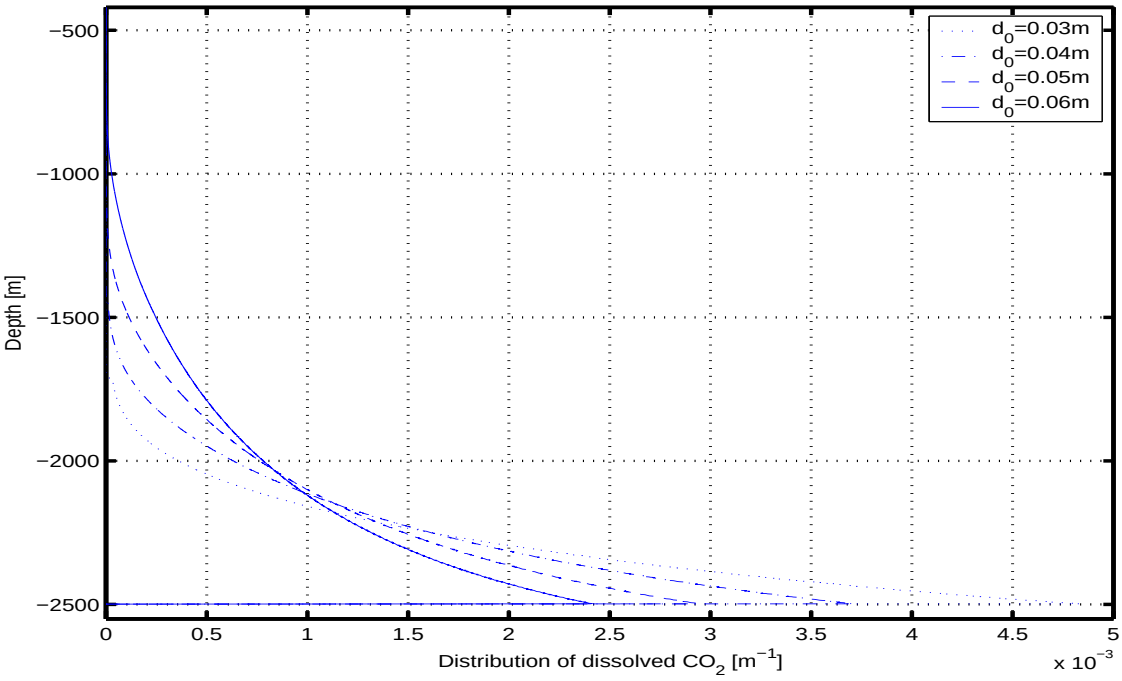

Figure 5.11: *Vertical distributions of dissolved CO_2 per meter for drops of four different sizes d_0 released from the depths of a) 2000 m and b) 2500 m.*

The critical depth

The seawater temperature and density profile in Figure 4.2 was given for depths between 500 and 800 meters, the depths at which the investigated single drop with a diameter of 8.9 mm was located during its rise. To be able to simulate drop releases at greater depths the temperature is here chosen to gradually decrease from 800 meters and down to 1500 meters, and from there have a constant value of 2 ^{o}C. The densities of CO_2 and seawater then follow the lines shown in Figure 5.12. The critical depth is where the drop of CO_2 has the same density as the surrounding seawater. This occurs at the depth of 2743.25 meters according to Figure 5.12. Drops that are released below this depth will sink and cause a distribution of dissolved CO_2 deeper in the water column. With other seawater characteristics than given here the critical depth would be located at a different depth.

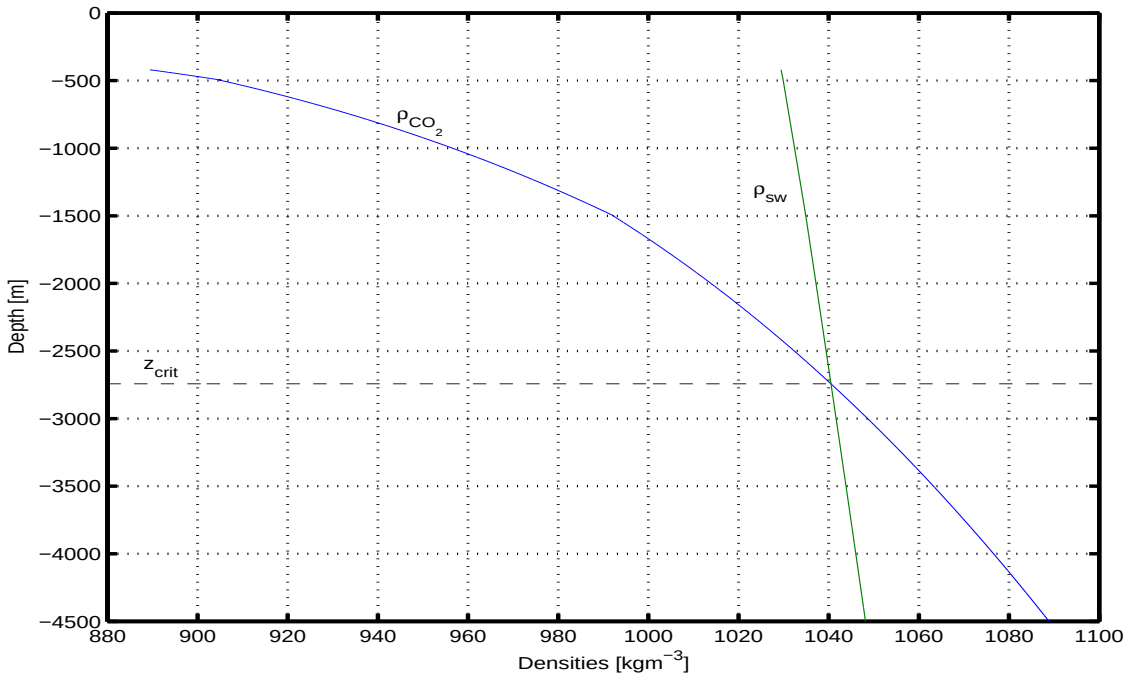

Figure 5.12: *Seawater and CO_2 densities and the critical depth, z_{crit}.*

For drop velocity equation 4.1 to be used for greater depths, an extension was made:

$$U_T = \begin{cases} \left(\frac{8gr|\rho_{sw}-\rho_{CO_2}|}{3C_d\rho_{sw}}\right)^{0.5} & \text{for} \quad \rho_{sw} \geq \rho_{CO_2} \\ -\left(\left(\frac{8gr|\rho_{sw}-\rho_{CO_2}|}{3C_d\rho_{sw}}\right)^{0.5}\right) & \text{for} \quad \rho_{sw} < \rho_{CO_2} \end{cases} \tag{5.1}$$

This makes it possible to simulate sinking of drops that are released below the critical depth.

The resulting fraction of dissolved CO_2 from the base case drop released at the depths of 1000, 2000, 2500, 3000, 3500 and 4500 meters are shown in Figure 5.13.

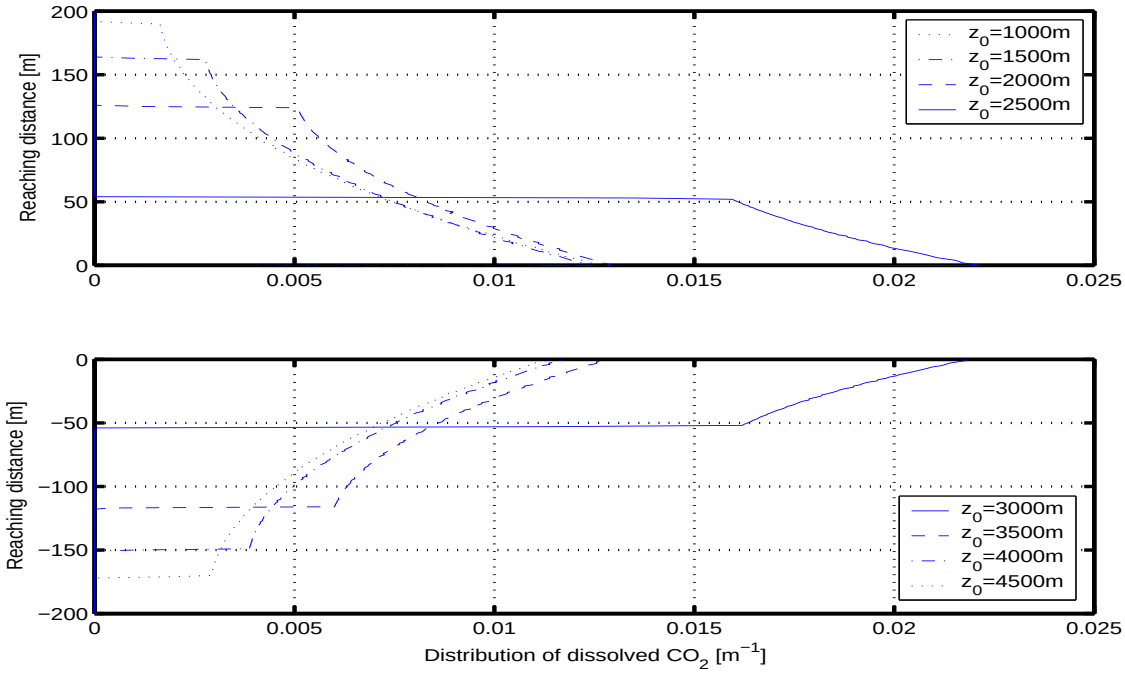

Figure 5.13: *Vertical distribution of dissolved CO_2 per meter for the base case drop released from different depths. The rising distance from the release depth of each drop is shown.*

The equivalent results for the drop released at depths near the critical depth are presented in 5.14. The velocity of the drop released at different depths are then shown in Figure 5.15, where time increases from right to left.

The closer to the critical depth the drops are released, the narrower becomes the vertical distributions of dissolved CO_2. The vertical distance reached depends on drop velocity (Figure 5.15). As is also seen in equation 5.1, when the densities of CO_2 and seawater become equal near the critical depth, the velocity approaches zero. This results in a narrower distribution of dissolved CO_2. When the drop is released quite near the critical depth, all the dissolved CO_2 is located around only a few meters as seen in Figure 5.14. Further away from the critical depth where the drops get larger relative velocities they move longer and thus bring dissolved CO_2 further away from the release depth.

As is seen in Figure 5.14 the curves are not quite smooth. This is because the layers here cover only a few meters and the model has a depth resolution of only 1 m. The result would be improved with a higher resolution.

Studying Figure 5.15 more closely it can be seen that the velocity patterns of the drops released above the critical depth are not equivalent to the velocities of the drops released below it. Notice for instance the two drops released from the depths of 1000 and 4500

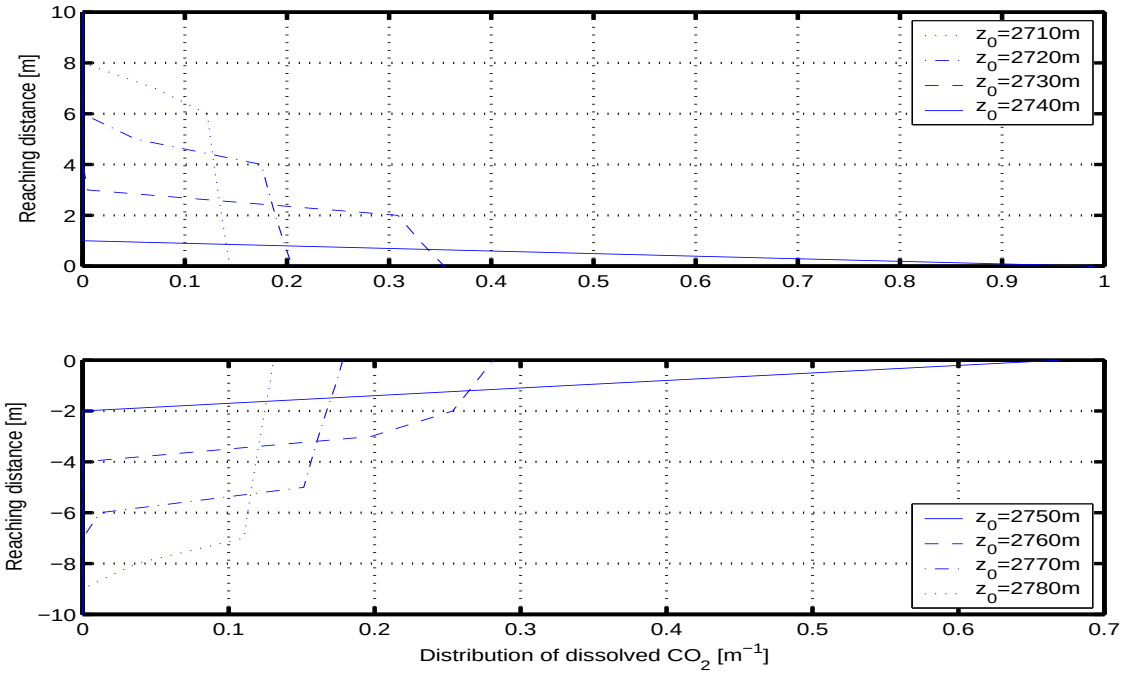

Figure 5.14: *Vertical distribution of dissolved CO_2 per meter for the base case drop released from different depths. The rising distance from the release depth of each drop is shown.*

meters. The distance from the critical depth is nearly the same for the drops. Therefore the velocity equation (equation 5.1) for the drop released above the critical depth will be similar to the equation for the drop released below it, except that for the second drop there will be a negative sign in front of the equation. In Figure 5.15 however the drop released from 1000 m depth is shown to experience a higher absolute velocity than the drop released from 4500 m depth. When the first drop has got the diameter of 3 mm it has achieved an absolute velocity of about 12.5 cms^{-1}, while the second drop has got an absolute velocity of less than 9 cms^{-1} at this stage.

This asymmetrical pattern is an effect of the higher compressibility of CO_2 than of seawater. As the CO_2 drop released at 1000 m rises in the ocean, its diameter gets reduced because the drop dissolves in the water. But the drop will also expand some because of the decreasing seawater pressure. The total effect is still a reduction of the drop size. As the drop released at 4500 m sinks, the surrounding increasing pressure compresses the drop. This effect comes in addition to the size reduction caused by the dissolution. Thus, the diameter of the sinking CO_2 drop reduces more than the diameter of the rising drop. Larger drops can achieve higher velocities than smaller drops (Figure 5.4), explaining the asymmetrical velocities of these two drops shown in Figure 5.15. Similarly the drop released from 1500 m depth can be compared with the one released from 4000 m depth as these drops have a nearly equal distance from the critical depth, and etc.

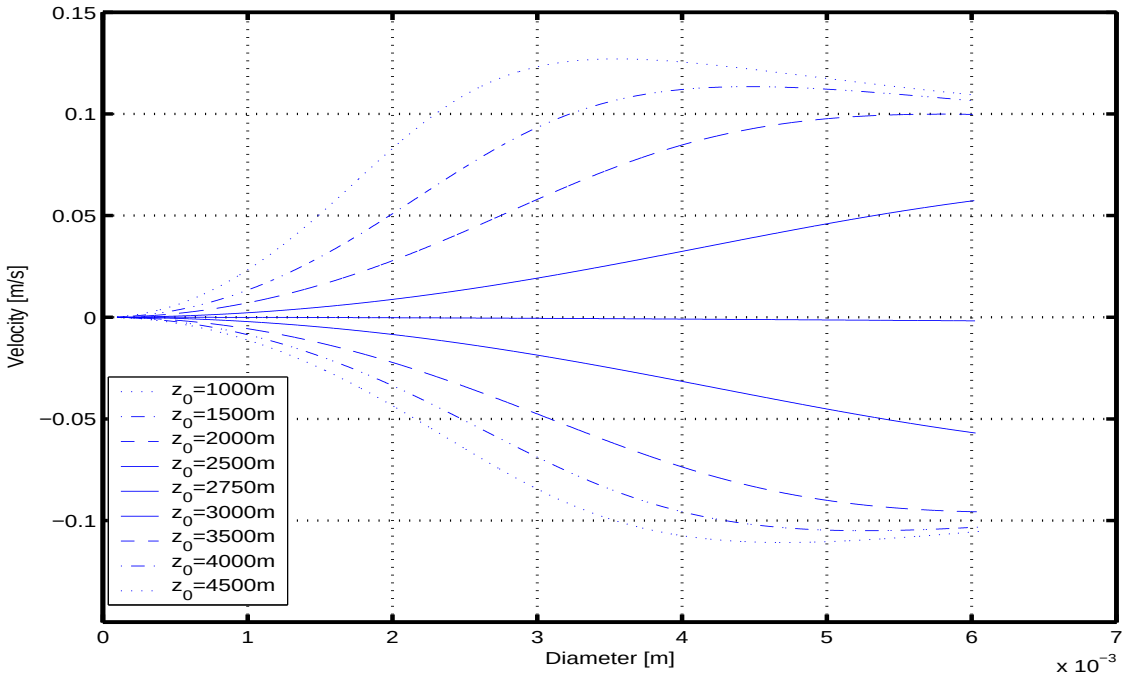

Figure 5.15: *The drop velocity at different depths, plotted with diameter.*

The effect of the asymmetric velocity patterns can be seen in Figure 5.13. Higher velocities result in longer traveling distances in the ocean. The dissolved CO_2 from the rising drops is then spread over larger vertical depth intervals then the dissolved CO_2 from the sinking drops.

Now, the center of the different depths in Figure 5.15 is here chosen to be the depth of 2750 m instead of the critical depth of 2743.15 m. Note that this only makes Figure 5.15 more symmetric than it would be if the center had the exact value of 2743.15 m. If we used the release depth of 4486.3 m to compare the release depth of 1000 m with, the distance from the critical depth would be exactly the same for both release depths. Then the drop released from 4486.3 m depth would have an even lower absolute velocity than the drop released from 4500 m depth and the difference in traveling distance would be consequently larger.

Hence the higher compressibility of CO_2 than of seawater implies that we can not expect the vertical distributions of dissolved CO_2 from drops released above the critical depth to be equivalent to distributions from drops released below this depth.

5.3 Polydispersed distributions

Next a number of drops generated by random probability distributions is examined.

5.3.1 Information from a laboratory experiment

An experiment by Tang & Masutani (2003) was performed to get information about the jet instability and breakup of gradually increasing liquid-liquid flow and the drop size distribution in the regimes that occurred. CO_2, crude oils and silicone fluids were injected into water through different orifices and over different velocities. Two optical techniques to study the drop behavior were used, a Phase Doppler Particle Analyzer (PDPA) to use on drops with a diameter smaller than 4 mm and video image analysis to measure larger drops. The liquid CO_2 was injected under simulated deep ocean conditions. The laboratory work by Tang & Masutani (2003) produced size spectra for five different regimes when employing different jet velocities. These were called varicose breakup, sinuous wave breakup, filament core breakup, wave atomization and fully atomization. The data from the first regime had the lowest injection speed. According to Tang & Masutani (2003) this regime could be described by a normal distribution with a single peak at a diameter between 6 and 7 mm. As the drop in our model is released into the ocean with no jet velocity, this regime is the most reasonable to compare our results with.

The statistical values given by Tang & Masutani (2003) were D50 and D95. D50 is the median diameter of the data of which 50 percent are smaller, D95 is the median size of the data of which 95 percent is finer. With a large amount of data, D50 can be approximated by the mean diameter. Tang & Masutani (2003) reported that D50 was 6.28 mm and D95 equal to 7.1 mm.

From Chapter 3 we know that statistical tables give the area under the standard normal curve that correspond to the probability that Z has a value less than z for different values of z. As 95 % of the distribution generated by Tang & Masutani (2003) is smaller than the value of D95 = 7.1 mm, the probability that Z is less than z = 7.1 is 0.95. The Z-value that correspond to this probability is found in the tables to be 1.645.

Now we need to convert this value, being for a standard normal distribution with mean zero and standard deviation 1, so that it can be used for a normal distribution with mean 6.28 mm and a corresponding standard deviation. This is done by equation 3.45. The corresponding standard deviation is then:

$$\sigma = \frac{7.1mm - 6.28mm}{1.645} = 0.5mm. \tag{5.2}$$

A normal distribution of drops with standard deviation 0.5 mm would then be the suggested distribution based on the laboratory result when a mean of about 6 mm is considered. The

next section includes the normal distribution with the standard deviation found here and this value compared with larger standard deviations.

5.3.2 Normal distributions

The normal distribution was introduced in Chapter 3. Here randomly generated distributions of diameters for a large number of drops are compared, all varying around the diameter of 6 mm. Then for a normal distribution with a standard deviation σ, 68% of the drops are located between the diameter of $6 \pm \sigma$ mm and 95 % between $6 \pm 2 \cdot \sigma$ mm. The maximum drop diameter that can be generated in the model is set equal to 60 mm.

Results of using various standard deviations are shown in Figure 5.16 a). Corresponding histograms for each standard deviation is presented in Figure 5.16 b). A number of 10^5 random sized drops were generated.

For the first two standard deviations demonstrated in Figure 5.16 a) the largest fractions of dissolved CO_2 per meter are about 0.012 m^{-1} and are located at 800 meters. The depth range of the distributions is about 250 meters with dissolved CO_2 reaching up to the depth of about 550 meters. The CO_2 distributions are similar to the one for a single drop with a diameter of 6 mm shown in Figure 5.2 and would be exactly equal if we had used a standard deviation of zero.

The use of larger standard deviations provides greater spreads of the initial drop sizes with more larger and smaller drops. The smallest drops will not add much dissolved CO_2 to the vertical distribution. The larger drops will however rise longer and bring the dissolved CO_2 higher in the water column as is demonstrated in Figure 5.16 a).

As the generation of normally distributed diameters around 6 mm would give some negative values, especially when using large standard deviations, these values were eliminated from the data. As the drops are very small here, the effect of this is relatively small.

a)

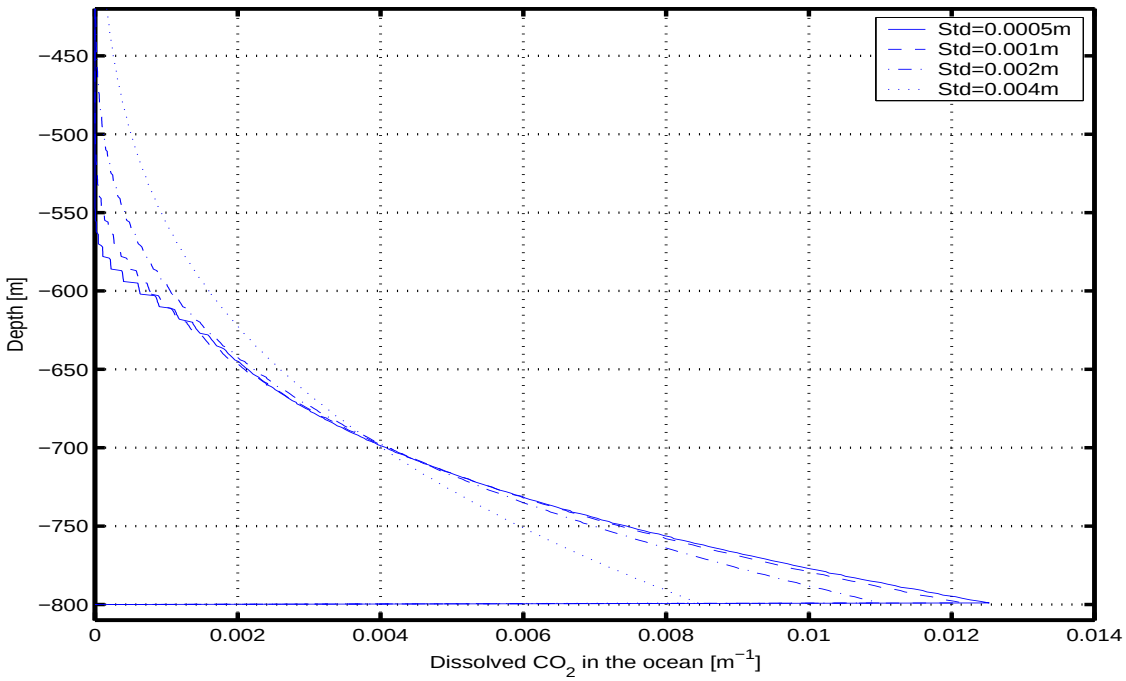

b)

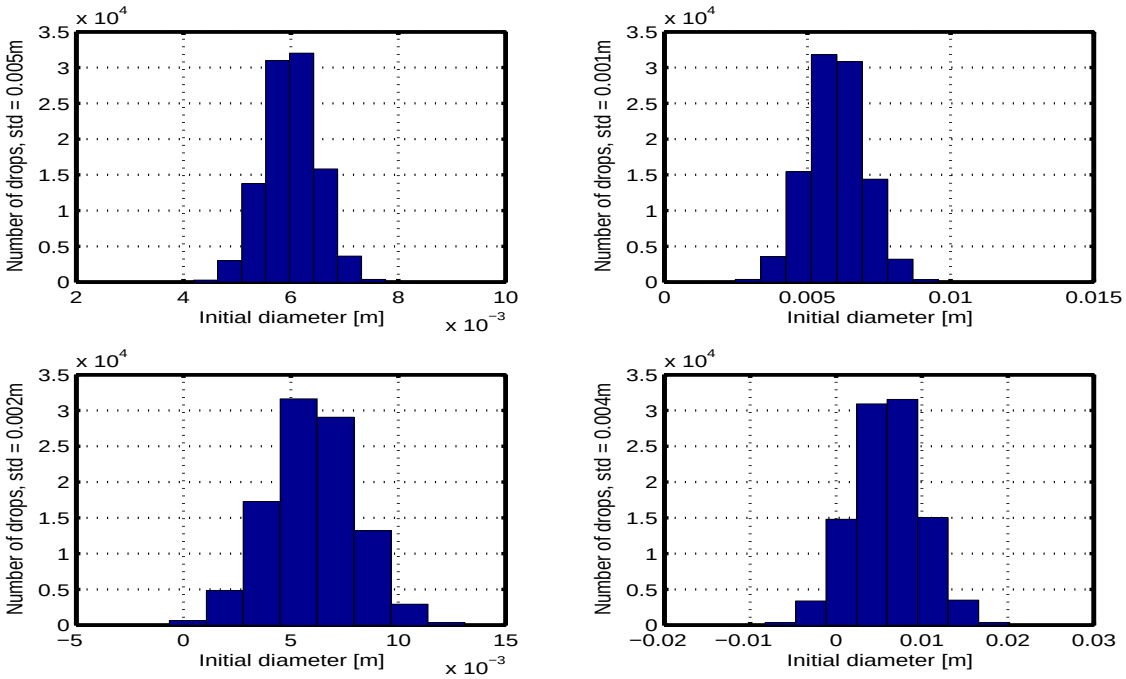

Figure 5.16: *a) Normal distributions with mean 6 mm and standard deviations 0.5, 1, 2 and 4 mm and b) histograms corresponding to the different cases in a).*

5.3.3 Lognormal distributions

To avoid the problem with negative values in the distribution the lognormal distribution is tried. This probability distribution was also described in Chapter 3.

In order to achieve a lognormal distribution of drops with mean 6 mm, the correct values for μ and σ to be used in equation 3.46 had to be found. These were calculated from equation 3.47 with E(x) = 6 mm and equation 3.48 with the different standard deviations replaced by $Var(x)^{0.5}$.

In Figure 5.17 and 5.18 the lognormal probability distribution is demonstrated with different values of standard deviations $Var(x)^{0.5}$. A number of 10^5 arbitrary sized drops were generated also here. A normal distribution with standard deviation 0.5 mm is included for comparison.

As seen in the corresponding histograms, especially when large standard deviations is used, the lognormal distribution takes another shape than the normal distribution. It has a higher amount of smaller drops and a 'tail' of larger drops. With a standard deviation of 0.5 mm the difference between using the normal distribution and the lognormal distribution seems small. As the standard deviation increases, the lognormal distribution shows a higher spread in the water column. A lognormal distribution of standard deviation 4 mm shows a greater spread of dissolved CO_2 in the water column than a normal distribution with the equivalent standard deviation, seen in Figure 5.18 and 5.16. This is because of the tail of large drops provided in the lognormal distribution. Even though there are many more smaller drops, it is sufficient with one large drop to drastically alter the distribution.

a)

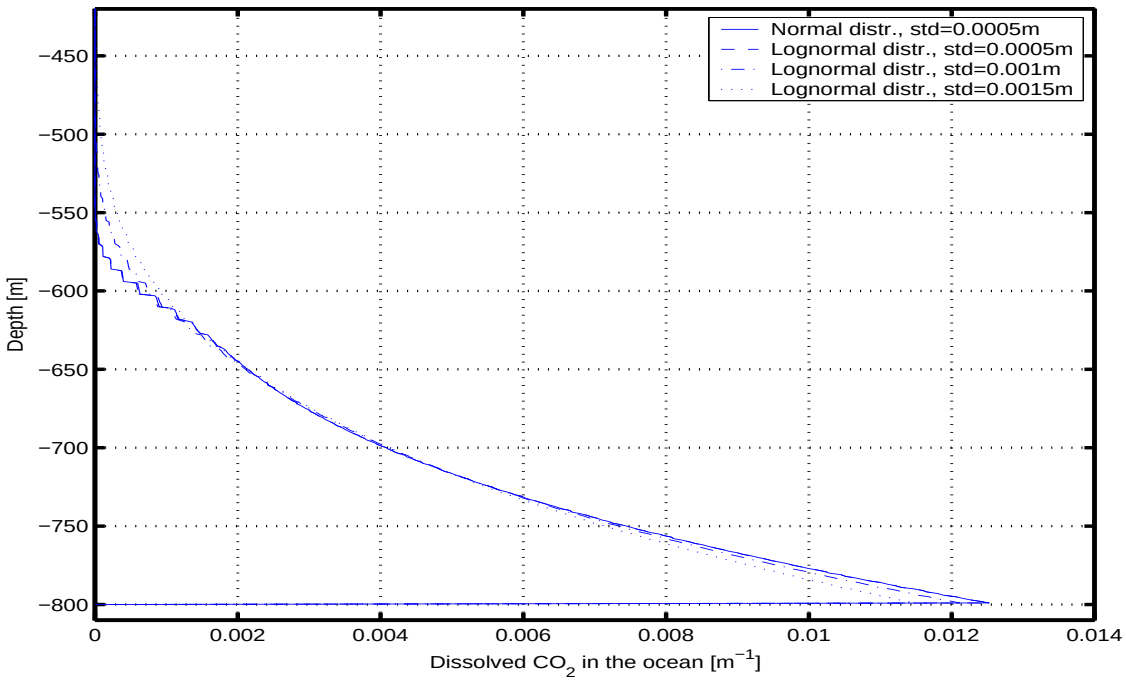

b)

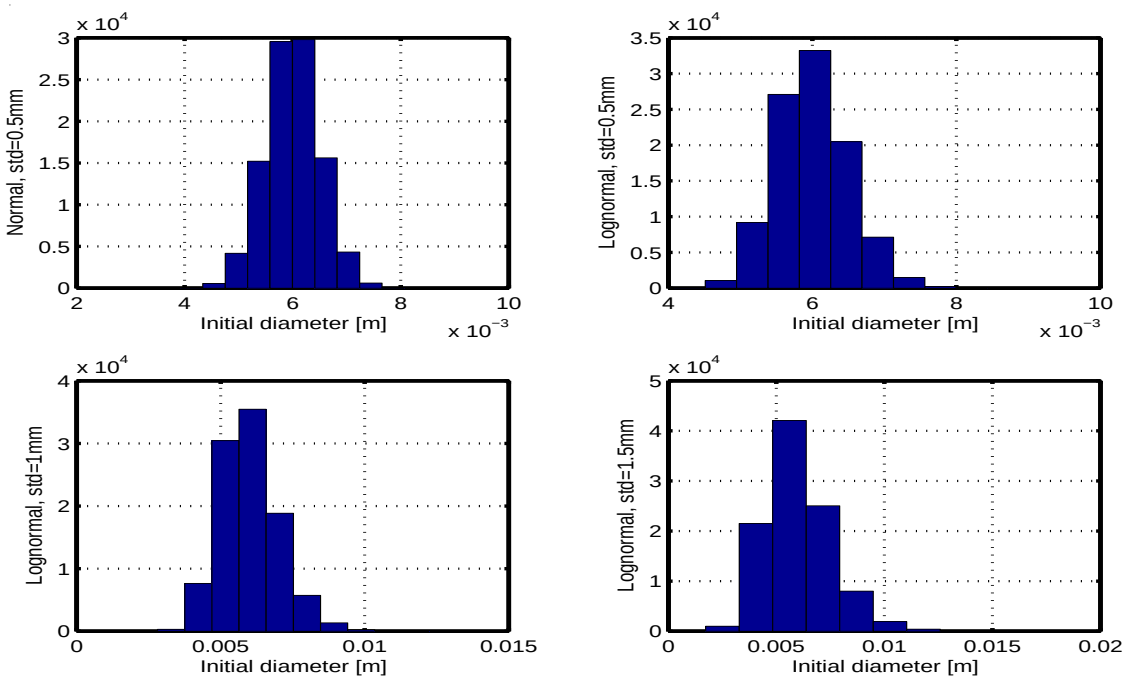

Figure 5.17: *a) Normal distributions with mean 6 mm and standard deviations 0.5 compared to lognormal distribution with equaivalent mean and standard deviations of 0.5, 1 and 1.5 mm and b) Histograms corresponding to the different cases in a).*

a)

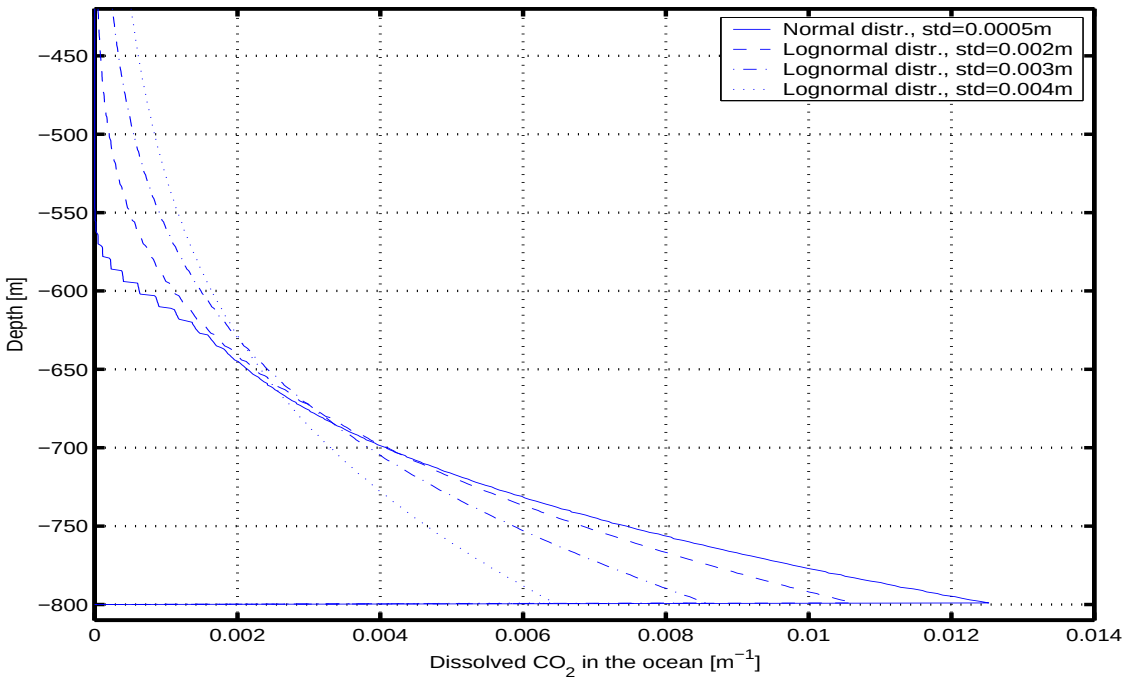

b)

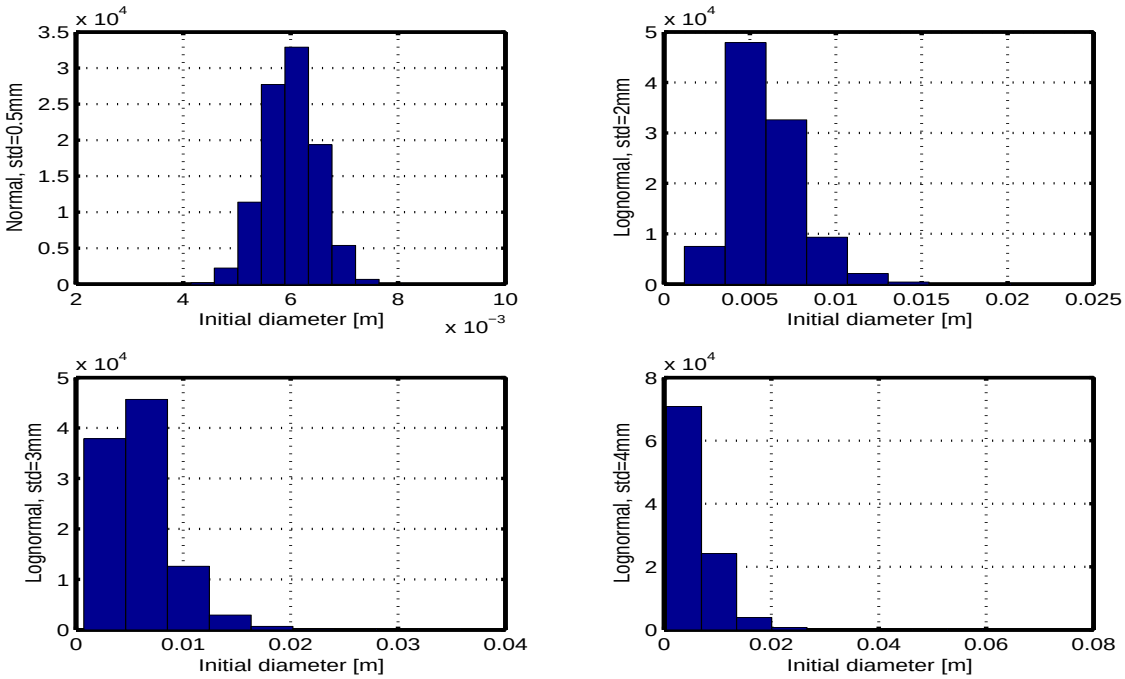

Figure 5.18: *a) Normal distributions with mean 6 mm and standard deviations 0.5 compared to lognormal distribution with equivalent mean and standard deviations of 2, 3 and 4 mm and b) Histograms corresponding to the different cases in a).*

Chapter 6

Discussion

This thesis already contains some required discussion, especially the analysis made in Chapter 4. This will be summarized here and in addition will most of the results be further discussed.

6.1 Terminal velocity

As presented in Chapter 4, a numerical model was used to calculate the terminal velocity of a single CO_2 drop rising in the ocean. The calculations were compared with observations by Brewer et al. (2002). The presence of hydrate on the drop surface is expected to change drop shape and drop dynamics. It has been suggested that with hydrate formation CO_2 drops get spherical shapes and become rigid. Hence the drop velocities should correspond to the drag curve of solid, spherical particles, referred to as the standard drag curve. This theory was used in the single drop model with the implemented seawater and drop characteristics given from Brewer et al. (2002). The drop velocity calculated with the use of standard drag showed to markedly decrease as the drop size decreased. When comparing this to the observed drop velocity a clear deviation was proved. The observed drop instead got a slightly increasing terminal velocity. In the standard drag curve the drag coefficient increases with decreasing diameter. In order to achieve the observed velocities a decreasing drag with decreasing drop size was instead needed.

Drag is influenced by several factors which could possibly explain the deviation found. External experimental forces could have played a role. Both turbulence and seawater lifted with the drop caused by the rising ROV could maybe reduce the drag of the drop. If the reason why the drop did not show a rigid sphere behaviour can be explained by these factors alone, it would be correct to use the rigid sphere theory with the standard drag curve in the numerical model to simulate the behaviour of CO_2 drops in seawater.

Purity of seawater is believed to affect the drag. The drag is also dependent on phase, gas bubbles get a different drag curve than solid particles. The drag curve of liquid drops

covered with hydrate is not known and laboratory results showing rigid particle behaviour of a hydrate-covered CO_2 drop might not describe the moving patterns in the real ocean.

The possible differences between laboratory results and the ocean must also be considered when it comes to drop shape. The suggestion of spherical shape of a hydrate-covered drop was based on laboratory work. If the CO_2 drop is allowed to deform regardless of the hydrate film surrounding it, the drag will be changed. An ellipsoidal drop has a higher drag than a sphere. The Reynolds, Morton and Eotvos numbers of the drop observed by Brewer et al. (2002) indicate that the drop initially had an ellipsoidal shape that later became spherical. This points to a decreasing drag with decreasing drop diameter, compatible to what is needed to match the drop velocities observed. Change of shape might thus be an important factor explaining the deviating drag.

To investigate this further, two theories of dynamics that included change of shape were tried, the theory by Grace et al. (1976) and a theory developed for bubbles by Bozzano & Dente (2001). Both theories provided velocities that matched the observed drop velocity better than the result of using the theory with standard drag. Calculated drop velocity using the theory by Grace et al. (1976) however only matched the first two observational points. This might be explained by the fact that this theory was developed for drops and bubbles in contaminated water. The drag of the drop studied here having Reynolds numbers between 200 and 900 is more similar to the drag of a particle in pure water (Figure 3.4). This implies that surface active contaminants had a negligible effect on the dynamics of the observed drop (also suggested by Brewer et al. (2002)). The theory by Bozzano & Dente (2001) fits most of the observed drop velocity pattern well. The exception is the last observational point where the drop is very small. Here the observations show a continuing increasing velocity, while the theory provides a decreasing velocity down to zero. That measurement errors would be larger for a small drop than for a large one could possibly explain this deviation.

Another component that needs attention is interfacial tension. In the calculations this is set equal to a value of 0.023 Nm^{-1}, but it is dependent on environmental conditions like temperature and pressure. If the interfacial tension changes during the drop rise, the properties of the drop will change and the drop drag and dynamics may be affected. The exact variations of the interfacial tension between a hydrate-covered CO_2 drop rising in the ocean, and the surrounding seawater is not known for sure. From literature it has a value of between 0.021 and 0.030 Nm^{-1} with internal variations. Fitting of the interfacial tension in the two theories for deformed drops was tried out, but it was not possible to obtain values of interfacial tension that matched the observed drop behaviour exactly.

Without any adjustments however, except neglecting an approximation done by Bozzano & Dente (2001) that is only valid for gas bubbles (Section 4.2.3), the theory by Bozzano & Dente (2001) shows a reasonably good fit for the drop studied here.

The effects of using the two different theories were also explored with the use of different initial drop sizes (Chapter 5.2.3). Comparing the theory by Bozzano & Dente (2001) and the theory with standard drag it was shown that the vertical spreading of dissolved CO_2 largely

depends on drop size. For small drops the distribution of dissolved CO_2 is narrower when the theory with standard drag is used, while for large drops it is narrower when the theory by Bozzano & Dente (2001) is used. This is due to the different velocity patterns of the two theories. For a small drop the velocity is generally lower when the theory with standard drag is used, for a large drop it is lower when the theory by Bozzano & Dente (2001) is used. As drop velocity significantly influences how far a drop will ascend in the water column, a lower drop velocity results in a narrower vertical distribution of dissolved CO_2. In Figure 4.7 it was shown that the drop velocity calculated with the theory by Bozzano & Dente (2001) fits the ocean observations best. By using the theory with standard drag to calculate the velocity of small drops we would then estimate a narrower distribution of dissolved CO_2 in the water column than what might be realistic in the real ocean. Equivalently, for large drops (with $d \geq 10$ mm) we would predict a larger vertical spread with use of the theory with standard drag than what might be the result if single drops were released into the ocean. Large drops rise higher and bring more dissolved CO_2 higher up in the water column than small drops. The result for large drops is therefore most important.

After this study was done, a paper by Chen et al. (2003) was found to confirm the above results. Observations by Ozaki (1999) (in Japanese) of a liquid CO_2 drop covered with a hydrate film showed deformation of the drop shape and it was concluded that such a drop must be regarded as a rigid, irregular-ellipse particle. Chen et al. (2003) performed a similar study to the one made in this thesis, calculating terminal velocities when using the rigid-sphere drag coefficient and the drag coefficient where deformation was taken into account. The calculations were compared to the observations done by Ozaki (1999) where three different seawater conditions were included. The results are shown in Figure 6.1.

The observations clearly follow the terminal velocity patterns resulting from the use of the drag coefficient that includes deformation. Here the observed drops also get a decreasing velocity down to zero as they get very small, equal to what was implied in the results of using the theory of Bozzano & Dente (2001) (Figure 5.6). That very small drops get lower velocities is also supported by Figure 3.4. The drag curve of fluid particles with very low Reynolds numbers is shown to approach the drag curve of rigid spheres. Hence the terminal velocities for very small drops should approach the calculated velocities using the theory with standard drag. This is seen to occur in Figure 5.6.

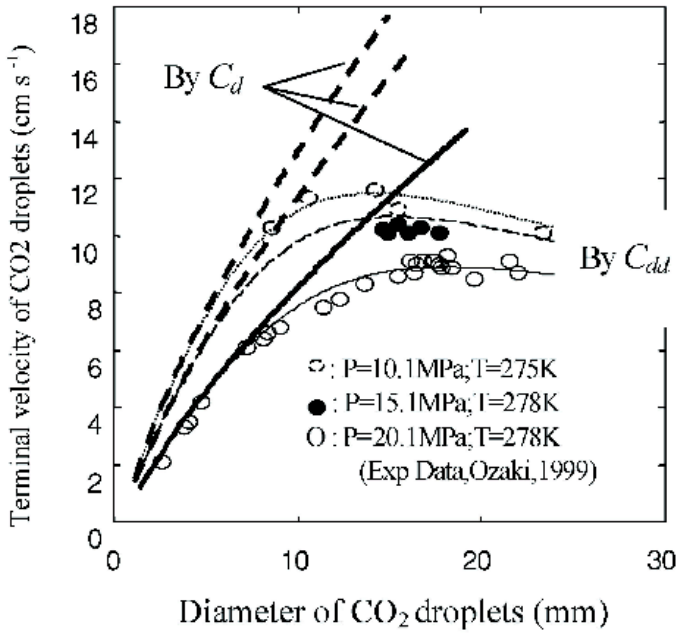

Figure 6.1: *Observations by Ozaki (1999) compared to calculated terminal velocities taking deformation into account (by C_{dd}) and assuming spherical shape (by C_d) (Chen et al. 2003).*

6.2 Mass transfer

Two ways to calculate mass transfer were also studied. Under conditions where hydrate formation can take place, the solubility of CO_2 is a dominating factor. Hydrate is expected to reduce the mass transfer from a CO_2 drop to the surrounding seawater. With a slower dissolution the drop can be brought further in the ocean and give a larger spread of dissolved CO_2 in the water column. In this way hydrate formation can give a positive effect. On the other hand, depending on release depth, if the drop dissolves slow enough to reach the depth were transition to gas phase occurs, an amount of CO_2 gas could be released to the atmosphere.

Brewer et al. (2002) found that the mass transfer from the observed hydrate-covered drop could be approximated by a constant value of 3.0 $\mu molcm^{-2}s^{-1}$. To achieve more knowledge of the effects of hydrate formation on mass transfer, a commonly used theory including the Ranz-Marshall correlation was also tried out. The theory with the Ranz-Marshall correlation contains the proportionality factor called the Sherwood number. This is dependent on the Reynolds number and the theory thereby also includes velocity. To take hydrate formation into account the equation had to be multiplied with a reduction factor. Using the theory with the Ranz-Marshall correlation matched the mass transfer of the observed drop best when a

reduction factor of 2 was used.

The two theories to calculate mass transfer were also tried out with different initial drop sizes. When studying the results of using the two theories it was seen that for initially small drops the dissolution happened slightly faster when the theory with the Ranz-Marshall correlation was used than when the constant dissolution rate was used. For initially large drops the dissolution was faster using the constant dissolution rate in the beginning. In the end it was again faster when the theory with the Ranz-Marshall correlation was used. For small drops this results in a narrower vertical distribution when the constant dissolution rate is used, while for large drops the vertical distribution of dissolved CO_2 is larger when this rate is used (Figure 5.9). The constant dissolution rate of 3.0 $\mu molcm^{-2}s^{-1}$ found by Brewer et al. (2002) was used throughout Chapter 5 when different drop sizes and release depths were studied. The differences between the results of using the constant dissolution rate and the more general equation with the Ranz-Marshall correlation indicate that the the mass transfer from a hydrate-covered drop to the surrounding seawater might not be described by a constant dissolution rate under any conditions.

Note however that the theory with the Ranz-Marshall correlation is based on laboratory results. The mass transfer calculated with this theory might not necessarily fit the dissolution rate of CO_2 drops in the real ocean. The dissolution of CO_2 is nevertheless influenced by several factors and might vary also when other factors than initial drop size are considered. Increased turbulence increases mass transfer. When hydrate formation occurs the mass transfer is also dependent on temperature. A laboratory experiment by Aya et al. (1997) showed that the dissolution rate of a hydrate-covered CO_2 drop decreases with decreasing temperature.

6.3 Release depth

Model experiments including the theory of dynamics by Bozzano & Dente (2001) and the constant dissolution rate of 3.0 $\mu molcm^{-2}s^{-1}$ were performed with different release depths. The traveling distances of the drops and the vertical distributions of dissolved CO_2 in the different cases were studied.

Drops that are released below the critical depth will sink and provide distributions of dissolved CO_2 deeper in the ocean. The vertical distributions for drops released below the critical depth are not equal to the corresponding distributions for drops released above this depth. This is seen when two drops of initially equal sizes are compared. One is released above the critical depth and will rise in the ocean, the other is released below this depth and will sink. The distance from the critical depth is exactly the same so that the velocity equation 5.1 is equal for the two drops, except that they will have opposite signs in front of the equation. The high compressibility of CO_2 compared to seawater would then give the sinking drop an extra reduction of size with increasing pressure. A rising drop expands its size some

due to the decreasing surrounding pressure, even though the size reduction caused by the dissolution is larger. So although the diameter of the rising drop gets reduced, it reduces less than the diameter of the sinking drop. Larger drops can achieve higher velocities (Figure 5.6, theory by Bozzano & Dente (2001)). This results in a higher absolute velocity for the rising drop than for the sinking. A higher velocity results in a longer traveling distance in the ocean. The dissolved CO_2 from the rising drops is then spread over a larger vertical depth interval then the distribution from the sinking drop.

The nearer the critical depth the drops are released, the lower will the absolute drop velocity be and the narrower will the vertical distribution of dissolved CO_2 be (Figure 5.13). Achieving a very thin layer of dissolved CO_2 around the critical depth would not be realistic in the real ocean as the density of seawater increases as CO_2 dissolves in it. Seawater density increases with approximately $8 \cdot 10^{-3}\ kgm^{-3}$ per $molm^{-3}$ of total dissolved inorganic carbon (Haugan & Drange 1992). A large density increase would force the layer to sink down. The thinner the layer is the more concentrated will the dissolved CO_2 be and the heavier will the layer be. It might even bring the drops with it as it sinks (Alendal & Drange 2001). This effect is not taken into account in the present studies.

Depending on how close the release depth is to the sea bottom, sinking of dissolved CO_2 could give a high concentration of dissolved CO_2 on the sea floor. In the case with a leakage of CO_2 from the sea bottom, dissolved CO_2 would be in close contact with the sea bed independent of release depth. If the leakage occurs at a depth below the critical depth, the time before the CO_2 reaches the atmosphere would probably be much longer than if the leakage takes place above this depth. The environmental impacts might however be higher.

6.4 Probability distributions

Different probability distributions of drops were studied at last. Using a normal distribution with mean 6 mm and standard deviation 0.5 mm matches a laboratory experiment performed by Tang & Masutani (2003) on CO_2 drops in water under simulated deep water conditions. Cases with larger standard deviations were also studied. Then a greater spread of the initial drop diameters were generated, with more larger and smaller drops. A higher amount of small drops will not influence the vertical distribution of dissolved CO_2 greatly. The larger drops however will rise higher before they are fully dissolved and bring a greater part of the dissolved CO_2 to a shallower depth of the ocean.

With large standard deviations negative values of the diameter could occur. This problem was avoided using the lognormal distribution. Here equivalent standard deviations were used and the different probability distributions were compared. These two statistical distributions were recommended to use for drops by Crowe et al. (1998). Using a small standard deviation the two probability distributions show equal vertical distributions of dissolved CO_2, while when using a larger standard deviation the vertical spread is larger with the lognormal distri-

bution than with the normal distribution. This is due to the tail of large drops generated for the lognormal probability distribution. As large drops rise higher they will provide a larger vertical spread of dissolved CO_2, even though there is a much higher amount of small drops in the drop distribution.

It is important to be aware of that the numerical model simulates single drops released into the ocean, not a plume of drops. The probability distributions with numerous single drops will not include the effects in a plume. There we could also expect seawater being lifted up with the plume. And like the case with a thin layer near the critical depth there would be a density increase from the dissolved CO_2 in the plume which would cause sinking. The numerical model may then better describe drops released by a seeping leakage of CO_2 from the sea bottom than a release of CO_2 into the ocean for storage intentions.

Chapter 7

Summary and conclusions

7.1 Summary

CO_2 is a natural component of the atmosphere-seawater system in continuous exchange between atmosphere and ocean. The ocean contains 50 times more carbon than the atmosphere. Due to the release of anthropogenic CO_2 to the atmosphere, the natural carbon cycle has been disturbed. A third of the released CO_2 to the atmosphere is today taken up in the ocean, but the whole ocean has a capacity to absorb 70-90 % of the total released anthropogenic CO_2 in the entire fossil fuel period. Due to the thermocline barrier however, it takes several hundred years for the entire ocean to get into a new steady state with the atmosphere. Most of the anthropogenic CO_2 that is taken up in the ocean therefore ends up in the surface waters, giving a reduced value of pH here which might affect the marine life. To reduce this and other impacts from an increased CO_2 level in the atmosphere, storage of CO_2 is one option that might become necessary in a transition period to newer energy sources. Storage of CO_2 in the ocean or in geological formations under the sea bottom with potential leakage into the ocean both requires investigation of the behaviour of CO_2 and CO_2 drops in seawater.

A numerical model was used to simulate the release of single CO_2 drops into the ocean. An ocean experiment on single drops performed by Brewer et al. (2002) was employed to get information about seawater and drop characteristics. This information was implemented into the model so that the simulation would better fit a real life experiment. As the observations by Brewer et al. (2002) showed that hydrate formation occurred, hydrate formation is included in this study. The single drop model was then used to study distributions of dissolved CO_2 in the water column. Variations of drop size, initial depth and theories of dynamics and mass transfer were explored. A database with dissolved CO_2 for numerous drops of different initial sizes was produced. Normal and lognormal probability distributions were generated by a Matlab program drawing the needed initial drop sizes from the database.

When drop velocity was calculated in this thesis it became clear that using a theory with standard drag for rigid, spherical drops did not fit the drop behaviour observed by Brewer et al. (2002), in spite of suggestions by researchers (Figure 4.3). Change of drop shape, varying interfacial tension between the CO_2 drop and seawater, variation of purity of the surrounding seawater and external forces like turbulence caused by the experimental procedure could all cause a drag curve more similar to the one needed to match the observed velocities.

A theory of dynamics by Bozzano & Dente (2001) developed for bubbles and accounting for change of shape was found and tried. When using this theory in the numerical model a convincingly good fit of the terminal velocity was provided for the drop studied (Figure 7.1). The need for deformation to be taken into account in the calculations was confirmed by Chen et al. (2003).

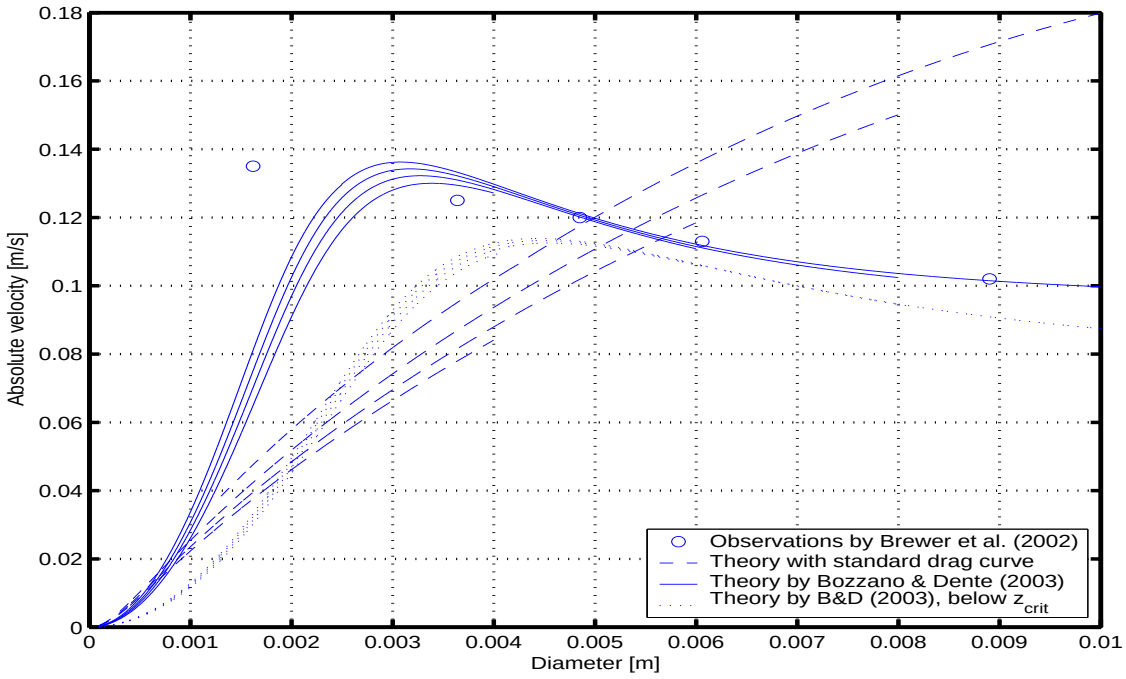

Figure 7.1: *Absolute velocity with drop diameter for 4 drops with initial diameters 4, 6, 8 and 10 mm. Solid lines represent the theory by Bozzano & Dente (2001) for deformed drops, stippled lines the theory with standard drag curve for spheres, and circles represent the drop with initial diameter 8.9 mm observed by Brewer et al. (2002). All drops are released from the depth of 800 m, except the drops shown as the 4 dotted lines, which are released from the depth of 4686 m. The distances from the critical depth (of 2743 m) are equal for the two release depths.*

The theory of dynamics by Bozzano & Dente (2001) was also compared with the theory with standard drag when different initial drop diameters were used (Figure 7.1). It is seen that a release of small drops gives a larger spread in the water column when using the theory by Bozzano & Dente (2001) than when using the theory with standard drag. Drops being

initially larger than 10 mm will on the other hand not rise as high with the theory of Bozzano & Dente (2001) as with the theory with standard drag and hence give a narrower vertical distribution in the ocean.

Chen et al. (2003) suggested that the observational deviation from the rigid sphere theory could cause an overestimation of the vertical range of dissolved CO_2 if this deviation was not taken into account. Here we found that when drops larger than 10 mm exist in the drop distribution, the vertical range of dissolved CO_2 might be overestimated if the rigid sphere theory is used in the simulations of a CO_2 release.

Based on laboratory results hydrate is expected to reduce the mass transfer from a CO_2 drop to the surrounding seawater. The Ranz-Marshall correlation fitted the observed mass transfer when a reduction factor of 2 was used. The Sherwood number was then:

$$Sh = 2 + 0.35 Re^{0.5} Sc^{0.33}. \tag{7.1}$$

That hydrate reduces the dissolution rate with a factor of 2 is compatible with laboratory results on dissolution of CO_2 drops in seawater.

The critical depth for the seawater properties used here was found to be at 2743.25 m depth. The nearer the critical depth the drops are released, the lower will the drop velocity be and the narrower will the vertical distribution of dissolved CO_2 be (Figures 5.13 and 5.14).

The numerical simulations demonstrated that the vertical distributions of dissolved CO_2 for drops released below the critical depth are not equivalent to the distributions from the drops released above this depth. This is because the absolute velocities for the drops released below the critical depth are lower than for those released above it. This is shown in Figure 7.1 where four drops are released at two depths with equal initial distances from the critical depth.

Normal and lognormal probability distributions were compared in the end. With a large standard deviation the vertical distribution was greater with the lognormal distribution than with the normal distribution (Figure 5.18 and 5.16, respectively). This is due to the long tail of large drops in the lognormal distribution. Even though the amount of small drops is huge compared to the amount of large drops, it is sufficient with only one large drop to provide a large vertical distribution of dissolved CO_2.

7.2 Conclusions

1. Standard drag of rigid spheres does not fit the drag of a rising CO_2 drop in the ocean.

2. An existing parametrisation for slip velocity allowing for change of shape matches observed drop velocity reasonably well.

3. When deformation is not included in the calculations of drop terminal velocities, an overestimation of the vertical spread of dissolved CO_2 might be made.

4. Model simulations indicate that hydrate reduces the mass transfer from a CO_2 drop to the seawater with a factor of 2.

5. Releasing CO_2 near the critical depth leads to a narrower vertical range of dissolved CO_2, hence release depth is an important factor influencing the distribution of dissolved CO_2 in the water column.

6. Vertical distributions from drops released above and below the critical depth are not symmetric about the axis of the critical depth. Below the critical depth the spread is narrower.

7. The distribution of dissolved CO_2 in the water column is especially sensitive to the amount of large drops in the drop distribution. Large drops rise higher and provide a larger vertical distribution.

7.3 Suggestions for future work

The numerical model simulated single CO_2 drops in the ocean, released either by a single drop experiment or by a seeping leakage of CO_2 from the sea bottom. For studies of deliberately released plumes of CO_2 or leakages of larger amounts of CO_2 into the ocean, the parameterisations found in this thesis could possibly be included in an extended numerical model. This should preferably include the increase of seawater density due to higher concentrations of dissolved CO_2 than those studied here. In addition, other factors that influences the behaviour of CO_2 like injection rate and background velocities could be included.

Even though many model calculations (Sato et al. 2000, Chen et al. 2003, Alendal & Drange 2001) on the behaviour of CO_2 in seawater have been performed lately, there is a lack of ocean experiments to verify the research done. In this thesis theory was compared to one ocean experiment and one drop observed at five stages. Additional similar experiments would reduce uncertainties that could be due to local seawater characteristics etc. Experiments should also be performed with different initial drop sizes and at different release depths. Hydrate formation is especially a phenomenon that still needs extensive investigation.

The experiment by Brewer et al. (2002) provided valuable information about single CO_2 drops so that the single drop model could be compared and adjusted to actual observations. An ocean plume experiment would bring additional knowledge about the behaviour of CO_2 in the ocean and provide data that plume models could be compared to.

Appendix A

The numerical model

The numerical model used in this thesis is written in Fortran 90. The model is integrated in time by a fourth and fifth order Runge-Kutta method (Section A1). The main model equations are shown below:

$$\frac{dx}{dt} = u \tag{A.1}$$

$$\frac{dy}{dt} = v \tag{A.2}$$

$$\frac{dz}{dt} = U_T(r, \rho_{sw}, \rho_{CO_2}, P, T) \tag{A.3}$$

$$\frac{dM}{dt} = \dot{M}(r, U_T, \rho_{sw}, \rho_{CO_2}, T, C_s, hydred) \tag{A.4}$$

$$M = \rho_{CO_2} \frac{4}{3} \pi r^3 \tag{A.5}$$

In this thesis u and v, determining the horizontal movement of the drop, are set equal to zero. U_T is the terminal velocity of the rising or sinking drop dependent on droplet radius, density of seawater and CO_2, pressure and temperature.

$\dot{M}$ is the mass transferred from the CO_2 drop to the seawater, dependent on radius, terminal velocity, density of seawater and CO_2, temperature, concentration of dissolved CO_2 far from the drop surface and a reduction factor to take hydrate formation into account. Knowing the radius and density of a drop, the mass M is found by equation A.5.

The different drag parametrisations are found in Section A2 and the mass transfer alternatives in A3. Density of seawater is calculated from the algorithm developed by the international group of experts on standards (UNESCO 1987) which is dependent on seawater salinity, temperature and pressure. Density of CO_2 is calculated from a 32 term Modified Benedict-Webb-Rubin equation of state (Ely et al. 1989) in Section A4.

The numerical model was developed by Dr. Guttorm Alendal.

A.1 Runge-Kutta methods

The Runge-Kutta methods (Cheney & Kincaid 1985) got their name after the German mathematicians Carl Runge and Willhelm Kutta. They developed the methods to imitate the Taylor series method without needing analytical differentiation of the original equation.

The Runge-Kutta method of order 2 can be written as follows:

$$x(t+h) = x(t) + \frac{1}{2}(F_1 + F_2) \tag{A.6}$$

where

$$F_1 = hf(t,x) \tag{A.7}$$

$$F_2 = hf(t+h, x+F_1). \tag{A.8}$$

An error term is required to restore the equality. For Runge-Kutta methods of order 2 the error term is only of order h^3. Second-order Runge-Kutta methods are therefore not widely used on large computers.

The fourth-order Runge-Kutta method is formulated as:

$$x(t+h) = x(t) + \frac{1}{6}(F_1 + 2F_2 + 2F_3 + F_4) \tag{A.9}$$

where

$$F_1 = hf(t,x) \tag{A.10}$$

$$F_2 = hf(t+\frac{h}{2}, x+\frac{1}{2}F_1) \tag{A.11}$$

$$F_3 = hf(t+\frac{h}{2}, x+\frac{1}{2}F_2) \tag{A.12}$$

$$F_4 = hf(t+h, x+F_3). \tag{A.13}$$

The error here contains h^5.

The fifth-order Runge-Kutta method is given by

$$x(t+h) = x(t) + \frac{1}{24}F_1 + \frac{5}{48}F_4 + \frac{27}{56}F_5 + \frac{125}{336}F_6 \tag{A.14}$$

where

$$F_1 = hf(t,x) \tag{A.15}$$

$$F_2 = hf(t+\frac{1}{2}h, x+\frac{1}{2}F_1) \tag{A.16}$$

$$F_3 = hf(t+\frac{1}{2}h, x+14F_1+\frac{1}{4}F_2) \tag{A.17}$$

$$F_4 = hf(t+h, x-F_2+2F_3) \tag{A.18}$$

$$F_5 = hf(t+\frac{2}{3}h, x+\frac{7}{27}F_1+\frac{10}{27}F_2+\frac{1}{27}F_4) \tag{A.19}$$

$$F_6 = hf(t+\frac{1}{5}h, x+\frac{28}{625}F_1-\frac{1}{5}F_2+\frac{546}{625}F_3+\frac{54}{625}F_4-\frac{378}{625}F_5). \tag{A.20}$$

A.2 Drop velocity

Three alternatives are used to calculate drop terminal velocities. These are all more extensively described in Chapter 3.

1. The first is the theory of spherical drops with standard drag:

$$U_T = \left(\frac{8gr(\rho_{sw} - \rho_{CO_2})}{3C_d\rho_{sw}}\right)^{0.5} \tag{A.21}$$

where

$$C_d = \frac{24}{Re_r}(1 + 0.15Re_r^{0.687}). \tag{A.22}$$

2. The second alternative is the theory of deformed drops by Grace et al. (1976):

$$U_T = \frac{\mu_{sw}}{\rho_{sw}d_e}Mo^{-0.149}(J - 0.857) \tag{A.23}$$

where

$$J = \begin{cases} 0.94H^{0.757} & \text{for} \quad 2 < H <= 59.3 \\ 3.42H^{0.441} & \text{for} \quad H > 59.3 \end{cases} \tag{A.24}$$

and

$$H = \frac{4}{3}EoMo^{-0.149}\left(\frac{\mu_{sw}}{\mu_w}\right)^{-0.14}. \tag{A.25}$$

The viscosity of water is $\mu_w = 9 \cdot 10^{-4}$ $[kgm^{-1}s^{-1}]$.

3. And the third alternative is the theory of deformed drops by Bozzano & Dente (2001):

$$U_T = \left(\frac{8gr_e(\rho_{sw} - \rho_{CO_2})}{3C_d\rho_{sw}}\right)^{0.5} \tag{A.26}$$

where the drag is found from:

$$C_d = f\left(\frac{a}{r_e}\right)^2 \tag{A.27}$$

with

$$f = \frac{48}{Re}\left(\frac{1 + 12Mo^{1/3}}{1 + 36Mo^{1/3}}\right) + 0.9\frac{Eo^{3/2}}{1.4(1 + 30Mo^{1/6}) + Eo^{3/2}} \tag{A.28}$$

and

$$\left(\frac{a}{r_e}\right)^2 \cong \frac{10(1 + 1.3Mo^{1/6}) + 3.1Eo}{10(1 + 1.3Mo^{1/6}) + Eo}. \tag{A.29}$$

The Reynolds, Eotvos and Morton numbers are given in Chapter 3.

A.3 Mass transfer

Two alternatives to calculate mass transfer are used, also better explained in Chapter 3.

1. The first is the method with use of the Ranz-Marshall correlation. Equation 3.29 from Chapter 3 is in the model written as:

$$\frac{dm}{dt} = -Sh\pi d\rho_{sw} D_v M_{CO_2}(C_{sat} - C_s) \tag{A.30}$$

where C_{sat} is the saturation concentration of dissolved CO_2 at the drop surface and is set equal to 1363.33 $molm^{-3}$. C_s is the concentration of dissolved CO_2 in the ocean far from the CO_2 drop surface and is set equal to 0. M_{CO_2} is the molar CO_2 equal to $44.01 \cdot 10^{-3}$ $[kgmol^{-1}]$. The Sherwood number:

$$Sh = 2 + 0.69 Re_r^{0.5} Sc^{0.33} \tag{A.31}$$

where

$$Sc = \frac{\nu_{sw}}{D_v}. \tag{A.32}$$

Here the kinematic viscosity of seawater with a temperature of 20 ^oC and salinity of 36 psu is used: ν_{sw} = $1.049 \cdot 10^{-6}$ $m^2 s^{-1}$. The diffusion coefficient D_v $[m^2 s^{-1}]$ is:

$$D_v = \frac{7.1141 \cdot 10^{-15} \cdot (273,15 + T)}{\mu_{sw}} \tag{A.33}$$

where the molecular viscosity of seawater, μ_{sw}, with temperature equal to 20 ^oC and salinity of 36 psu is $1.075 \cdot 10^{-3}$ $kgms^{-1}$.

2. The second method to calculate mass transfer is:

$$\frac{dm}{dt} = -4\pi r^2 \rho_{CO_2} V_m \Gamma \tag{A.34}$$

where Γ = 3.0 $\mu molcm^{-2}s^{-1}$ (Brewer et al. 2002).

A.4 Density of CO_2

Density of CO_2 is calculated from a 32 term Modified Benedict-Webb-Rubin equation of state (Ely et al. 1989):

$$P = \sum_{i=1}^{9} A_i \rho^i + exp(-\frac{\gamma\rho^2}{\rho_{cr}^2}) \sum_{i=10}^{15} A_i \rho^{(2i-17)} \tag{A.35}$$

where ρ is density and ρ_{cd} is critical density of CO_2. This equation is used for the density interval $\rho \in [1,160] \bigcup [900,1100] \frac{kg}{m^3}$, while the phase change is interpolated with a 3. degree polynomial to guarantee continuity in the first derivative (Thorkildsen & Haugan 1993):

$$\rho = (1-f)\rho_{liquid} + f\rho_{gas} \tag{A.36}$$

where

$$f = 3(\frac{P_{cond} - P + I}{2I})^2 - 2(\frac{P_{cond} - P + I}{2I})^3 \tag{A.37}$$

and ρ_{gas}, ρ_{liquid} are found from equation A.35 in the interval $\rho_{gas} \in$[1:60] and $\rho_{liquid} \in$ [900:1100]. The condensation pressure is calculated by (Drange & Haugan 1992):

$$P_{cond} = 34.8649 + 0.90485T + 0.0108504T^2. \tag{A.38}$$

The equation of state using equation A.35 is solved with respect to ρ with an Illinois algorithm implemented by Dr. Guttorm Alendal. The first derivative of equation A.35 with respect to P and solving for $\frac{\partial \rho_{CO_2}}{\partial P}$ we achieve:

$$\frac{\partial \rho}{\partial p} = \frac{1}{\sum_{i=1}^{9} A_i i \rho^{i-1} + exp(-\frac{\gamma \rho^2}{\rho_{cr}^2}) \sum_{i=10}^{15} A_i (\frac{2i-17}{\rho} - \frac{2\gamma\rho}{\rho_{cr}^2}) \rho^{(2i-17)}}) \tag{A.39}$$

In the interval where the equation of state is interpolated, $\frac{\partial \rho}{\partial P}$ is:

$$\frac{\partial \rho}{\partial P} = (1-f)\frac{\partial \rho_{liquid}}{\partial P} + f\frac{\partial \rho_{gas}}{\partial p} - (\rho_{gas} - \rho_{liquid})\frac{6((\frac{P_{cond}-P+I}{2I}) - (\frac{P_{cond}-P+I}{2I})^2)}{2I} \tag{A.40}$$

where f is given in equation A.37. As we use the hydrostatic pressure approximation we get:

$$\frac{\partial \rho}{\partial z} = \frac{\partial \rho}{\partial P}\frac{\partial P}{\partial z} = \frac{\partial \rho}{\partial P} g \rho_{sw} \cdot 10^{-5} [kg/m^4]. \tag{A.41}$$

$A_1 = RT$	$A_6 = \frac{b_{14}}{T} + \frac{b_{15}}{T^2}$	$A_{11} = \frac{b_{22}}{T^2} + \frac{b_{23}}{T^4}$
$A_2 = b_1 T + b_2 T^{1/2} + b_3 + \frac{b_4}{T} + \frac{b_5}{T^2}$	$A_7 = \frac{b_{16}}{T}$	$A_{12} = \frac{b_{24}}{T^2} + \frac{b_{25}}{T^3}$
$A_3 = b_6 T + b_7 + \frac{b_8}{T} + \frac{b_9}{T^2}$	$A_8 = \frac{b_{17}}{T} + \frac{b_{18}}{T^2}$	$A_{13} = \frac{b_{26}}{T^2} + \frac{b_{27}}{T^4}$
$A_4 = b_{10} T + b_{11} + \frac{b_{12}}{T}$	$A_9 = \frac{b_{19}}{T^2}$	$A_{14} = \frac{b_{28}}{T^2} + \frac{b_{29}}{T^3}$
$A_5 = b_{13}$	$A_{10} = \frac{b_{20}}{T^2} + \frac{b_{21}}{T^3}$	$A_{15} = \frac{b_{30}}{T^2} + \frac{b_{31}}{T^3} + \frac{b_{32}}{T^4}$

Table A.1: *Temperature dependency of the coefficients in equation A.35. See Table A.2 for the b_i coefficients.*

$b_1 = -0.164147038534x10^{-2}$	$b_{12} = 0.513786291437x10^{-1}$	$b_{23} = 0.201313458725x10^{7}$
$b_2 = 0.145929294249$	$b_{13} = 0.399290811531x10^{-4}$	$b_{24} = 0.183678443072x10^{1}$
$b_3 = -0.322567667165x10^{1}$	$b_{14} = -0.672823309226x10^{-2}$	$b_{25} = -0.683851238480x10^{1}$
$b_4 = 0.420707873671x10^{3}$	$b_{15} = 0.902241252782x10^{1}$	$b_{26} = 0.389996843596x10^{-2}$
$b_5 = -0.459593803667x10^{5}$	$b_{16} = 0.260383108327x10^{-3}$	$b_{27} = -0.678673537499$
$b_6 = 0.440698210123x10^{-4}$	$b_{17} = -0.278016427941x10^{-5}$	$b_{28} = 0.454450104416x10^{-5}$
$b_7 = -0.355905419463x10^{-1}$	$b_{18} = -0.148694555399x10^{-1}$	$b_{29} = 0.329755873375x10^{-4}$
$b_8 = 0.175125702459x10^{1}$	$b_{19} = 0.254880656162x10^{-3}$	$b_{30} = 0.583216588973x10^{-8}$
$b_9 = -0.681045405840x10^{5}$	$b_{20} = 0.737790214963x10^{5}$	$b_{31} = 0.744884409668x10^{-6}$
$b_{10} = -0.316765853771x10^{-5}$	$b_{21} = -0.107686044002x10^{7}$	$b_{32} = -0.136758502411x10^{-3}$
$b_{11} = 0.348868332019x10^{-2}$	$b_{22} = 0.537117265673x10^{3}$	
$\rho_{cr} = 10.63[mol/dm^3]$	$\gamma = 1$	

Table A.2: *The b_i coefficients of equation A.35 (see Table A.1)*

Appendix B

Notations

a	[m]	Major semi-axis of the drop
A	[m^2]	Cross sectional area of a fluid particle (Section 3.3)
A_i	i=1,...,15	Temperature dependent coefficients in the MBWR-32 eq. of state for CO_2 (Appendix A4)
b_i	i=1,...,32	Coefficients in the MBWR-32 eq. of state for CO_2 (Appendix A4)
C_d	[ms^{-1}]	Drag coefficient
C_{sat}	= 1363.33 [$molm^{-3}$]	Saturation concentration of dissolved CO_2 at the drop surface
C_s	[$molm^{-3}$]	Far field ambient value of the saturation conc. of dissolved CO_2
d	[m]	Diameter
D	[m]	Measure of size, like diameter or equivalent diameter (Section 3.5)
D50	[m]	Median diameter of the data of which 50 % are smaller (Section 5.3)
D95	[m]	Median diameter of the data of which 95 % are smaller (Section 5.3)
d_e	[m]	Equivalent drop diameter
D_v	[$m^2 s^{-1}$]	Diffusion coefficient
Eo	[1]	Eotvos number
E(x)		Mean of the lognormal distribution (Section 3.5)
$f_n(D_i)$		Discrete number frequency of drops in each interval ΔD (Section 3.5)
$f_n(D)$		Continuous frequency (Section 3.5)
F_D	[$kgms^{-1}$]	Drag force
g	=9.81[ms^2]	Acceleration due to gravity
I_r	[1]	Relative turbulence intensity (Section 3.3)
m	[kg]	Drop mass
M	[kg]	Drop mass (Appendix A)
$\dot{M}$	[kg]	Mass transfer (Appendix A)

m_c	[kg]	Mass of continuous phase
M_{CO_2}	$=44.01\cdot10^{-3}$ $[kgmol^{-1}]$	Molar mass of CO_2
m_d	[kg]	Mass of dispersed phase
Mo	[1]	Morton number
N		Total number of size intervals (Section 3.5)
n		Normal vector (Section 3.4)
P	[bar]	Hydrostatic pressure in the area of the drops (Appendix A4)
P_{cond}	[bar]	Condensation pressure for pure CO_2 (Appendix A4)
r	[m]	Drop radius
r_0	[m]	Initial drop radius (Section 4.3)
r_e	[m]	Equivalent radius
Re	[1]	Reynolds number
Re_r	[1]	Relative Reynolds number
S	$[m^2]$	Drop surface (Section 3.4)
S	[psu]	Seawater salinity
t	[s]	Time
t_0	[s]	Initial time (Section 4.3)
T	$[^oC]$	Temperature
u	$[ms^{-1}]$	Velocity vector of continuous phase
$u^{'}$	$[ms^{-1}]$	Turbulence fluctuations of the carrier fluid
U_{pure}	$[ms^{-1}]$	Terminal velocity for pure systems
U_T	$[ms^{-1}]$	Terminal rise velocity of the drop
v	$[ms^{-1}]$	Velocity vector of dispersed phase
V_m	$[m^3 mol^{-1}]$	Specific volume
Var(x)		Variance of the lognormal distribution (Section 3.5)
w	$[ms^{-1}]$	Velocity through drop surface (Section 3.4)
We	[1]	Weber number (Section 3.1)
X		Random variable of a normal distribution (Section 5.3)
x		Ordinate for a normal distribution (Section 5.3)
Z		Random variable of a normal distributions with mean zero and standard deviation 1 (Section 5.3)
z		Ordinate for a standard normal distribution (Section 5.3)
γ	$\in [0,1]$	Momentum amplification factor (Appendix A4)
Γ	$[molm^{-2}s^{-1}]$	Dissolution rate
κ	[1]	Viscosity ratio μ_d/μ_c (Section 3.3)
μ		Mean value (section 3.5)
μ_c	$[kgm^{-1}s^{-1}]$	Molecular viscosity of continuous phase

μ_{CO_2}	[kgm$^{-1}s^{-1}$]	Molecular viscosity of CO_2
μ_d	[kgm$^{-1}s^{-1}$]	Molecular viscosity of dispersed phase
μ_{sw}	=1.075·10^{-3} [$kgm^{-1}s^{-1}$]	Molecular viscosity of seawater (at T=20^oC and $S = 36psu$)
μ_w	=9·10^{-4} [$kgm^{-1}s^{-1}$]	Molecular viscosity of water
ν_c	[m$^2s^{-1}$]	Kinematic viscosity of the continuous phase
ν_{sw}	= 1.049·10^{-6} [m^2s^{-1}]	Kinematic viscosity of seawater (at T=20^oC and $S = 36psu$)
λ		Correction coefficient (Section 3.3)
ρ	[kgm^{-3}]	Density of free CO_2 (Appendix A4)
ρ_c	[kgm^{-3}]	Density of the continuous phase (= reference density)
ρ_{CO_2}	[kgm^{-3}]	Density of CO_2
ρ_{cr}	= 10.63 [mold$^{-1}m^{-3}$]	Critical density of CO_2 (Appendix A4)
ρ_d	[kgm^{-3}]	Density of fluid particle (dispersed phase)
ρ_s	[kgm^{-3}	Density of drop at surface (Section 3.4)
ρ_{sw}	[kgm^{-3}]	Density of seawater
σ	[Nm^{-1}]	Surface/interfacial tension
σ		Standard deviation (Section 3.5)
σ^2		Variance (Section 3.5)
σ_n		Number standard deviation (Section 3.5)
σ_n^2		Number variance (Section 3.5)
τ_V	[ms]	Momentum response time (Section 3.3)
ω_d	[1]	Mass fraction of the dispersed phase (CO_2) (Section 3.4)
$\omega_{d,s}$	[1]	Mass fraction of the dispersed phase at the surface (Section 3.4)
$\omega_{d,\infty}$	[1]	Mass fraction of the disp. phase in the freestream (Section 3.4)

Table B.1: *Table of notations. Sections are referred to when the notations are not used throughout the whole thesis.*

Bibliography

Alendal, G. & Drange, H. (2001), 'Two-phase, nearfield modelling of purposefully released CO_2 in the ocean', *Journal of Geophysical Research, Vol. 106 (C1)* pp. 1085–1096.

Alendal, G., Drange, H. & Haugan, P. M. (1994), 'Modeling of deep-sea gravity currents using an integrated plume model', *The Polar Oceans and Their Role in Shaping the Global Environment: The Nansen Centennial Volume, AGU Geophysical Monograph, Vol. 85, edited by O. M. Johannessen, R. D. Muench and J. E. Overland* pp. 237–247.

Archer, D., Kheshgi, H. & Maier-Reimer, E. (1997), 'Multiple timescales for neutralization of fossil fuel CO_2', *Geophysical Research Letters, Vol. 24* pp. 405–408.

Aya, I., Yamane, K. & Nariai, H. (1997), 'Solubility of CO_2 and density of CO_2 hydrate at 30 MPa', *Energy, Vol. 22, No. 2/3* pp. 263–271.

Aya, I., Yamane, K. & Yamada, N. (1992), 'Stability of Clathrate-Hydrate of Carbon Dioxide in Highly Pressured Water', *ASME HTD-Vol. 215, Fundamentals of Phase Change: Freezing, Melting and Sublimation* pp. 17–22.

Bacastow, R. & Stegen, G. R. (1991), 'Estimating the Potential for CO_2 Sequestration in the Ocean using a Carbon Cycle Model', *Oceanus, Vol. 3* pp. 1654–1657.

Bachu, S. (2000), 'Sequestration of CO_2 in geological media: criteria and approach for site selection in response to climate change', *Energy Conversion and Management, Vol. 41* pp. 953–970.

Bachu, S. (2001), 'Sequestration of CO_2 in geological media in response to climate change: road map for site selection using the transform of the geological space into the CO_2 phase space', *Energy Conversion and Management, Vol. 43* pp. 87–102.

Batchelor, G. K. (1967), *An Introduction to Fluid Dynamics*, Cambridge University Press. ISBN0521098173.

Bozzano, G. & Dente, M. (2001), 'Shape and terminal velocity of single bubble motion: a novel approach', *Computers and Chemical Engineering, Vol. 25* pp. 571–576.

Brewer, P. G., Friederich, G., Peltzer, E. T. & Orr Jr., F. M. (1999), 'Direct Experiments on the Ocean Disposal of Fossil Fuel CO_2', *Science, Vol. 284* pp. 943–945.

Brewer, P. G., Glover, D. M., Goyet, C. & Shafer, D. K. (1995), 'pH of the North Atlantic Ocean: Improvements to the global model for sound absorption in sea water.', *Journal of Geophysical Research, Vol. 100 (C5)* pp. 8761–8776.

Brewer, P. G., Peltzer, E. T., Friederich, G. & Rehder, G. (2002), 'Experimental Determination of the Fate of Rising CO_2 Droplets in Seawater', *Environmental Science and Technology, Vol. 36, No. 24* pp. 5441–5446.

Caldeira, K. (2003), 'Monitoring of ocean storage projects', *IPCC workshop on carbon dioxide capture and storage* .

Caldeira, K. & Wickett, M. E. (2003), 'Oceanography: Anthropogenic carbon and ocean pH', *Nature, Vol. 425* p. 365.

Caulfield, J. A., Auerbach, D. I., Adams, E. & Herzog, H. J. (1997), 'Near field impacts of reduced ph from ocean disposal', *Energy Conversion and Management, Vol. 38* pp. 343–348.

Chen, B., Song, Y., Nishio, M. & Akai, M. (2003), 'Large-eddy simulation of double-plume formation induced by CO_2 dissolution in the ocean', *Tellus 55B* pp. 723–730.

Cheney, W. & Kincaid, D. (1985), *Numerical Mathematics and Computing*, Brooks/Cole Publishing Company. ISBN0-534-04356-9.

Chun, B.-S. & Wilkinson, G. T. (1995), 'Interfacial Tension in High-Pressure Carbon Dioxide Mixtures', *Ind. Eng. Chem. Res.* pp. 4371–4377.

Clamen, A. & Gauvin, W. H. (1969), 'Effects of turbulence on the drag coefficient of spheres in a supercritical flow regime', *AIChE Journal, Vol. 15* p. 184.

Clift, R., Grace, J. R. & Weber, M. E. (1978), *Bubbles, Drops and Particles*, Academic Press.

Crowe, C., Sommerfield, M. & Tsuji, Y. (1998), *Multiphase flows with droplets and particles*, CRC Press. ISBN-0-8493-9469-4.

Drange, H., Alendal, G. & Johannessen, O. M. (2001), 'Ocean release of fossil fuel CO_2: A case study', *Geophysical Research Letters, Vol. 28 (No. 13)* pp. 2637–2640.

Drange, H. & Haugan, P. M. (1992), 'A feasibility study of dissolution and sequestration of CO_2 in the ocean', *Technical Report 54, The Nansen Environmental and Remote Sensing Center, Final report of a project executed by NERSC in 1992 for Statoil* .

Ely, J., Haynes, W. & Bain, B. (1989), 'Isochoric(p, V_m, T) measurements on CO_2 and on $(0.982CO_2 + 0.018N_2)$ from 250 to 300 K at pressure to 35 MPa', *Journal of Chemical Thermodynamics, Vol. 21* pp. 879–894.

Grace, J. R., Wairegi, T. & Nguyen, T. H. (1976), 'Shapes and velocities of single drops and bubbles moving freely through immiscible fluids', *Trans.Instn.Chem.Engrs., Vol. 54* pp. 167–173.

Haugan, P. M. & Drange, H. (1992), 'Sequestration of CO_2 in the deep ocean by shallow injection', *Nature, Vol. 357* pp. 318–320.

Haugan, P. M. & Drange, H. (1996), 'Effects of CO_2 on the ocean environment', *Energy Conversion and Management, Vol. 37* pp. 1019–1022.

Haugan, P. M., Thorkildsen, F. & Alendal, G. (1995), 'Dissolution of CO_2 in the ocean', *Energy Conversion and Management, Vol. 36, No. 6-9* pp. 461–466.

Herzog, H., Eliasson, B. & Kaarstad, O. (2000), *Scientific American* pp. 54–61.

Hirai, S., Okazaki, K., Tabe, Y., Hijikata, K. & Mori, Y. (1997), 'Dissolution rate of liquid CO_2 in pressurized water flows and the effect of clathrate films', *Energy, Vol. 22, No. 2/3* pp. 285–293.

Hoffert, M. I., Wey, Y.-C., Callegari, A. J. & Broecker, W. S. (1979), 'Atmospheric Response to Deep-Sea Injections of Fossil-Fuel Carbon Dioxide', *Climatic Change, Vol. 2* pp. 53–68.

Holder, G. D. & Warzinski, R. P. (1996), *Prepr. Pap. Am. Chem. Soc. Div. Fuel Chem., Vol. 41 (4)* p. 1452.

IPCC (2001), *Climate Change 2001: The Scientific Basis - Contribution of Working Group I to the Third Assessment Report of the Intergovernmental Panel on Climate Change*, World Meteorological Organization / United Nations Environment Programme.

Kling, G. W., Evans, W. C., Tuttle, M. L. & Tanyileke, G. (1994), 'Degassing of Lake Nyos.', *Nature, Vol. 368* pp. 405–406.

Kuznetsova, T. & Kvamme, B. (2002), 'Atomistic computer for thermodynamic properties of carbon dioxide at low temperatures', *Energy Conversion and Management, Vol. 43* pp. 2601–2623.

Magnesen, T. & Wahl, T. (1993), *Nersc Technical Report, Vol 77A* .

Marchetti, C. (1977), 'On Geoengineering and the CO_2 Problem', *Climatic Change, Vol. 1* pp. 59–68.

Mori, Y. H. (1998), 'Clathrate hydrate formation at the interface between liquid CO_2 and water phases - a review of rival models characterizing "hydrate films"', *Energy Convers. Mgmt, Vol. 39, No. 15* pp. 1537–1557.

Mori, Y. H. & Mochizuki, T. (1998), 'Dissolution of liquid CO_2 into water at high pressures: A search for the mechanism of dissolution being retarded through hydrate-film formation', *Energy Convers. Mgmt, Vol. 39, No. 7* pp. 567–578.

Nishikawa, N., Ishibashi, M., Ohta, H., Akutsu, N., Tajika, M., Sugitani, T., Hiraoka, R., Kimuro, H. & Shiota, T. (1995), *Energy Conversion and Management, Vol. 36* p. 489.

Ohmura, R. & Mori, Y. H. (1998), 'Critical Conditions for CO_2 Hydrate Films To Rest on Submarine CO_2 Pond Surfaces: A Mechanistic Study', *Environmental Science and Technology, Vol. 32, No. 8* pp. 1120–1127.

Ozaki, M. (1999), *Annual Report of RITE* pp. 286–307.

Radhakrishnan, R., Demurov, A., Herzog, H. & Trout, B. L. (2003), 'A consistent and verifiable macroscopic model for the dissolution of liquid CO_2 in water under hydrate forming conditions', *Energy Conversion and Management* pp. 771–780.

Sato, T., Jung, R.-T. & Abe, S. (2000), 'Direct Simulation of Droplet Flow With Mass Transfer at Interface', *Journal of Fluids Engineering, Vol. 122* pp. 510–516.

Sato, T. & Sato, K. (2002), 'Numerical prediction of the dilution process and its biological impacts in CO_2 ocean sequestration', *Journal of Marine Science and Technology, Vol. 6* pp. 169–180.

Schiller, L. & Naumann, A. (1933), 'Über die grundlegenden Berechungen bei der Schwerkraftaufbereitung', *Ver. Deut. Ing. Vol. 77* pp. 318–320.

Stegen, G. R., Cole, K. H. & Bacastow, R. (1993), 'The influence of discharge depth and location on the sequestration of carbon dioxide', *Energy Conversion and Management, Vol. 34* pp. 857–864.

Stokes, G. G. (1851), 'On the effect of the internal friction of fluids on the motion of pendulums.', *Transactions of the Cambridge Philosophical Society Vol. 1* pp. 1–141.

Tang, L. & Masutani, S. M. (2003), 'Laminar to Turbulent Flow Liquid-liquid Jet Instability and Breakup', *Proceedings of The Thirteenth International Offshore and Polar Engineering Conference, Honolulu, Hawaii, USA* pp. 317–324.

Thorkildsen, F. & Haugan, P. M. (1993), 'Numerical model for plumes of dissolving co_2 droplets in seawater', *Technical Report 78, The Nansen Environmental and Remote Sensing Center, Final report of a project executed for Statoil in 1993* .

Thornton, H. & Shirayama, Y. (2001), 'CO_2 ocean sequestration and its biological impacts. III-1. Effects of CO_2 on benthic organisms', *Nippon Suisan Gakkaishi, Vol. 67* pp. 756–757.

Torobin, L. B. & Gauvin, W. H. (1961), 'The drag coefficients of single spheres moving in steady and accelerated motion in turbulent fluid', *AIChE Journal, Vol. 7* p. 615.

Uchida, T. & Kawabata, J. (1997), 'Measurements of mechanical properties of the liquid CO_2-water-CO_2-hydrate system', *Energy, Vol. 22, No. 2/3* pp. 357–361.

Uchida, T., Ohmura, R., Takeya, S., Nagao, J., Minagawa, H., Ebinuma, T. & Narita, H. (2003), 'Estimations of interfacial tensions between liquid CO_2 and water from the sessile-drop observations', *Greenhouse Gas Control Technologies, Volume II, J. Gale and Y. Kaya (Eds.), Elsevier Science Ltd.* pp. 1679–1682.

Walpole, R. E., Myers, R. H. & Myers, S. L. (1998), *Probability and Statistics for Engingeers and Scientists*, Prentice Hall International, Inc., Sixth edition. ISBN 0-13-095246-X.